

MINERALOGICAL MAPPING OF SELECTED AREAS OF THE LUNAR  
SURFACE USING MOON MINERALOGY MAPPER DATA

DISSERTATION

For the award of the degree Ph.D.

Of the Georg-August-University of Göttingen

within the doctoral program of Environmental Informatics  
of the Georg-August University School of Science (GAUSS)

Submitted by

Yehor Surkov

Göttingen, 2022

### **Thesis Committee**

Prof. Dr. Martin Kappas

Geographic Institute, Georg-August University of Göttingen

Dr. Urs Mall

Department of Planetary Science, Max-Planck Institute for Solar System Research

Dr. Vadym Kaydash

Institute of Astronomy, V.N. Karazin Kharkiv National University, Ukraine

### **Members of the Examination Board**

Prof. Dr. Martin Kappas

Geographic Institute, Georg-August University of Göttingen

Dr. Urs Mall

Department of Planetary Science, Max-Planck Institute for Solar System Research

Dr. Vadym Kaydash

Institute of Astronomy, V.N. Karazin Kharkiv National University, Ukraine

PD. Dr. Harald Krüger

Department of Planetary Science, Max-Planck Institute for Solar System Research

Dr. Daniel Wyss

Geographic Institute, Georg-August University of Göttingen

Prof. Dr. Yuri Shkuratov

Institute of Astronomy, V.N. Karazin Kharkiv National University, Ukraine

Prof. Dr. Carsten Damm

Institute of Computer Science, Georg-August University of Göttingen

## CONTENT

SUMMARY .....	5
CHAPTER 1. GENERAL INTRODUCTION.....	9
CHAPTER 2. [PAPER] IMPROVED CHANDRAYAAN-1 M3 DATA: A NORTHWEST PORTION OF THE ARISTARCHUS PLATEAU AND ADHERENT MARIA.....	13
2.1 Introduction.....	14
2.2 Additional data processing.....	18
2.2.1 Gaussian $\lambda$ -convolution.....	19
2.2.2 Fourier filtration.....	21
2.2.3 Band parameters.....	26
2.3 Results and discussion.....	29
2.3.1 Mapping band parameters.....	29
2.3.2 Geologic characterization.....	34
2.3.3 Age assessments.....	37
2.3.4 Relationships between spectral and geological data.....	42
2.4 Conclusions.....	50
2.5 References.....	51
CHAPTER 3. [PAPER] CHARACTERIZING PYROCLASTIC DEPOSITES OF LUNAR MARE VAPORUM WITH IMPROVED CHANDRAYAAN-1 M3 DATA.....	60
3.1 Introduction.....	61
3.2 M <sup>3</sup> data and processing.....	66
3.3 Results and discussion.....	68
3.3.1 Mapping the band parameters.....	69

3.3.2 The crater Hyginus.....	73
3.4 Conclusions.....	82
3.5 References.....	83
CHAPTER 4. [PAPER] LUNAR ILMENITE CONTENT AS ASSESSED BY IMPROVED CHANDRAYAAN-1 M3 DATA.....	93
4.1 Introduction.....	94
4.2 Source data and extra M <sup>3</sup> data processing.....	97
4.3 Mapping ilmenite abundance.....	103
4.4 Discussion.....	109
4.5 Conclusion.....	113
4.6 References.....	114
CHAPTER 5. GENERAL SUMMARY AND CONCLUSIONS.....	118
AKNOWLEDGEMENTS	

## SUMMARY

*The dissertation is concerned with spectrophotometric studies of selected areas of the lunar surface using the data generated by the mapping spectrometer Moon Mineralogy Mapper (M<sup>3</sup>), onboard the Chandrayaan-1 spacecraft. Spectrophotometry is one tool to investigate planetary surfaces by remote sensing. This technique is based on the measurement and further interpretation of diffuse reflection spectra, which contain information about the chemical and mineralogical composition, as well as the structure of the regolith of the surfaces studied.*

The M<sup>3</sup> spectrometer provided hyperspectral images covering 95 % of the lunar surface in the visible and near-infrared wavelengths range (from 540 to 3000 nm) with a spatial resolution of about 140 m/pixel. Unfortunately, due to the thermal issues during the flight, the Chandrayaan-1 spacecraft was not able to provide the M3 instrument the required stable environmental conditions for acquiring its data. This circumstance led to a deterioration of the data quality of the M3 instrument manifesting itself in various artifacts most visible in a random system of long, narrow vertical stripes which can be found on nearly all its hyperspectral images. This thesis proposes a new method to reduce the above-mentioned artifacts leading to a significant recovery of the original data quality. The new method consists of two stages: (1) a Gaussian convolution of the spectra recorded by an individual pixel of the image, and (2) a Fourier filtration of each spectral channel of the M3 image. These corrections are applied in an additional data processing step to the fully calibrated data which are publicly available through the Planetary Data System <https://pds-imaging.jpl.nasa.gov/volumes/m3.html>.

With the help of the new approach it now becomes possible to clearly identify the spectral parameters which are needed to analyze the M3 reflectance

spectra. The power of the new approach is demonstrated in this thesis by investigating the areas of the northwest portion of Aristarchus Plateau, Montes Agricola and contiguous maria. In particular, maps of the 1 and 2  $\mu\text{m}$  absorption band positions were used to build Adam's diagrams for the investigated regions. A cluster analysis of the diagram shows that the investigated area is composed of five spectral provinces which reveal significantly different mineralogic compositions mostly represented by pyroxenes of different types and lunar glasses. This approach has proved to be particularly useful for identifying and mapping the volcanic and pyroclastic glass deposits. It has been further applied to the investigation of pyroclastic glass on the southern part of Mare Vaporum. We could show that dark smooth deposits around a Hyginus crater contains pyroclastic material. They are the satellite pyroclastic deposits on this region rather than the outcrop of mare basalts, as they originally had been considered.

In another application of our new method we demonstrate how the new processing technique of the M3 data allowed us to investigate the irregular mare patches (IMP) inside the Hyginus crater, where we are now able to map spectral parameters on the spatial scales of original resolution (140 m/pixel). The IMP formations on the lunar surface were first discovered several decades ago during the Apollo-15 mission. Since that time, about one hundred of them have been identified using the high-resolution LRO NAC images. However, their spectral properties still have not been characterized satisfactorily due to their small sizes (less than few kilometers). The M3 spectra of the IMPs inside the Hyginus crater have two peculiarities: (1) the higher spectral slope and more proliferate absorption bands that are the spectral signatures of surface immaturity, and (2) the broad absorption band near 2  $\mu\text{m}$  which extends beyond 2.7  $\mu\text{m}$ . The second peculiarity was interpreted as the unique mineralogic composition of IMPs' regolith that includes spinel, a rare oxide mineral on the lunar surface. These findings are

consistent with the hypothesis that these formations are the result of young (less than 1,000,000 y.o) lunar volcanic activity.

The quantitative assessment of the ilmenite ( $\text{FeTiO}_3$ ) abundance in the lunar regolith is an important research topic in lunar surface science. Based on the fact that the distribution of the band depth near  $1.5 \mu\text{m}$  in lunar reflectance spectra shows a strong correlation with ilmenite, a new quantitative assessment of the ilmenite abundance in the lunar regolith has been undertaken using the M3 data which cover the region between the Mare Tranquilities and Serenitatis. This studied region also included the Apollo-17 landing site. A comparison of the remotely and laboratory estimated ilmenite abundances indicates the correctness of the proposed method for estimating ilmenite abundances. The distribution of ilmenite reveals significant variations of this mineral content in mare basalts from 0 up to 20 weight per cent. Ti in the lunar regolith is believed to be distributed between several mineralogical components (e.g. ilmenite, ulvospinel, agglutinic and pyroclastic glasses). Sato et al., (2017) developed the approach to retrieve only the amount of total  $\text{TiO}_2$ . With our new method developed in the framework of this thesis we are now able to estimate the amount of  $\text{TiO}_2$  that is a component only of ilmenite. Comparisons of the total amount of  $\text{TiO}_2$  with the ilmenite-bearing  $\text{TiO}_2$  shows that the ilmenite is the main  $\text{TiO}_2$ -containing mineral of the lunar basalts.

We can state that all of our results are compatible with the generally accepted modern views of the mineralogical composition of the lunar surface. They form a number of new clarifying provisions for the spectral and optical characteristics and mineralogical composition of the regolith, which is important for further studies of the formation of the Hyginus crater and rimae complex, the origin of IMPs, the flow processes, the solidification and further evolution of the basalts of Mare Tranquilitatis. The newly developed remote sensing methods,

which are presented in this thesis, can be applied to the spectral data of other lunar locations, in order to estimate or refine their mineralogical composition. Furthermore, the generation of global spectral and optical parameters maps and a mapping of the mineralogical diversity for scientific purposes will enable the planning of future space missions and a better assessment of the Moon's resource potential.



## CHAPTER 1. GENERAL INTRODUCTION

*The subject of research* is the spectral characteristics, optical properties, chemical and mineralogical composition of the lunar regolith.

*The choice of the research topic.*

Spectrophotometry of the surface of the Moon and other exospheric bodies of the Solar System from spacecrafts (SCs) allows for the study of the composition and structure of the lunar surface under conditions that are not possible from telescopic studies (better spatial resolution, wider spectral range and various lighting/observation conditions). In order to achieve better data accuracy under qualitatively better conditions, many space missions were launched by the world's leading space agencies (ESA SMART-1, JAXA SELENE, NASA LRO, China NSA Chang'E-1, ISRO Chandrayaan-1 and 2), during which a huge amount of data in different ranges of the electromagnetic radiation spectrum was accumulated.

With a spatial resolution of approximately 140 meters per pixel, and 85 narrow spectral bands covering the range from 0.54 to 3.0  $\mu\text{m}$ , where the diagnostic absorption bands of the main rock forming minerals of the Moon are located, and covering more than 95% of the lunar surface, data from the M<sup>3</sup> imaging spectrometer onboard the Chandrayaan-1 lunar orbiter are currently the most promising for studying and a detailed mapping of the chemical and mineralogical composition.

In the past knowledge of the composition of the lunar was based mainly on the information which could be derived from individual color filters (e.g. albedos and color ratios). These parameters can provide important information on the chemical composition, however only limited on the mineralogy of the lunar regolith. M<sup>3</sup> hyperspectral images make it possible to obtain new spectral

parameters as absorption band depth, position, integral depth, width at half-depth, asymmetry, and others for the surface of the Moon. This opens up new perspectives for detailed mineralogical mapping and the possibility of searching for new components of the surface composition, which until now have not been determined due to limited distribution and/or low content in the regolith. However, due to significant data distortions by technical factors, accurate determination and high quality mapping of absorption band parameters is almost impossible. The data obtained from M<sup>3</sup> are unique. To obtain high quality maps of the spectral parameters and their distributions existing methods to extract those parameters from the M<sup>3</sup> reflectance spectra must be improved or new methods be invented to estimate the abundance of the lunar mineralogical composition which may turn out to be relevant for future lunar prospecting.

*Purpose and tasks of the research.*

The purpose of this dissertation is to determine and construct maps of spectral parameter distributions using the processed data of the M<sup>3</sup> detector to establish the relationship between the received spectral parameters and the mineralogical composition of the lunar regolith, and to improve and develop methods for qualitative and quantitative prediction of the mineralogical composition. To achieve the goal, the following key tasks were set:

- 1) to analyze the effect of existing data artifacts of the M<sup>3</sup> scanning spectrometer on the determination of the parameters of the absorption bands in the reflection spectra;
- 2) to develop methods and appropriate software to eliminate existing artifacts;

3) to develop additional software for mineralogical forecasting and mapping of spectral parameters for further interpretation, cluster analysis of Adams diagrams obtained from the data of the M<sup>3</sup> detector;

4) to map spectral parameters for selected areas of the Moon's surface, establish a connection between optical and geological and mineralogical data; to conduct a mineralogical interpretation of the obtained spectral parameters;

5) to develop a method of quantitative analysis of the mineralogical composition of the Moon's surface.

#### *Research methods.*

To reduce the contribution of the main artifact of the M<sup>3</sup> data, which manifests itself in the images in the form of narrow (with a width of 1-2 image pixels) and very long (over 500 pixels) vertical bands, we used sequential convolution of the spectrum with a Gaussian window and a rejection frequency filter, which was subsequently additionally equipped with a convergence factor to prevent the manifestation of the Gibbs effect, the main drawback of the total reduction of components in the Fourier expansion.

When obtaining the depths and exact positions of the absorption bands present in the spectrum, the spectral continuum was approximated by a part of the convex hull of the spectrum. For further spectral and mineralogical analysis, cluster analysis was used to select spectral classes and construct class maps. To calibrate the dependence of the integral depth of the absorption band of ilmenite near 1.5  $\mu\text{m}$  to the laboratory spectral data of lunar samples from the LRMCC set (Isaacson et al., 2011a), a linear regression (using the least squares method) of the dependence of the corresponding spectral parameter on the experimentally measured content of ilmenite in the samples was applied.

*The studied regions:* the northwestern part of the Aristarchus Plateau, the southern part of the Mare Vaporum, together with the nearby Hyginus Crater area and the northern part of the Mare Tranquilitatis. These sites were selected due to their expected mineralogical diversity. In addition, the features located in these areas (for example, IMPs in the Hyginus crater, the complex of Hyginus crater and rimae, and the Taurus-Litov valley with the Apollo-17 landing site) are at the center of the current research of the Moon.

## **CHAPTER 2. [PAPER] IMPROVED CHANDRAYAAN-1 M<sup>3</sup> DATA: A NORTHWEST PORTION OF THE ARISTARCHUS PLATEAU AND ADHERENT MARIA**

We provide and test a method to obtain significant improvement of available Chandrayaan-1 M<sup>3</sup> data. The advance is achieved using the Gaussian  $\lambda$ -convolution of spectra and Fourier filtration of images. The main result is imagery of the reflectance across different wavelengths as well as parameters of 1  $\mu\text{m}$  and 2  $\mu\text{m}$  absorption bands with unprecedented quality. This approach can be particularly useful for further investigations using M<sup>3</sup> data, since it produces improved imagery of various lunar surface characteristics. We studied a region comprising a portion of the Aristarchus Plateau, Montes Agricola, and a small part of the mare surface in Ocean Procellarum to the north of Montes Agricola. We found that the lava flows in the area between the Aristarchus Plateau and Montes Agricola have a chemical/mineral composition different in comparison with mare areas to the northwest of the ridge Montes Agricola. We also identified distinct spectral properties of morphologically young craters located on the plateau and mare surface. A correlation diagram for positions of the minima of the 1 and 2  $\mu\text{m}$  bands allows a cluster analysis of the region, and we map areas associated with a cluster corresponding to pyroclastic glasses. Relationships between geologic and spectral parameter maps were established.

## 2.1 Introduction

The Indian Chandrayaan-1 lunar probe was launched in October 2008 and operated until August 2009. One of the main goals of the mission was performing high-resolution remote sensing of the Moon in visible, NIR, and X-ray spectral ranges (Goswami and Annadurai, 2009). At a surface resolution of about 100 m/pix, hyperspectral imaging with the scanning spectrometer M<sup>3</sup> onboard the probe provided a vast amount of data that are useful for developing new visions of the lunar surface (Goswami and Annadurai, 2009; Pieters, 2009). The M<sup>3</sup> operated from 420 to 3000 nm, where highly diagnostic mineral absorption bands occur. Individual M<sup>3</sup> images are long and narrow strips between lunar poles. The accumulation of contiguous image data provides global studies of the Moon, covering almost all the lunar surface at 85 wavelengths.

In this near-infrared spectral range, lunar minerals reveal crystal field bands formed, in particular, by electron transitions of the d–d type between split energy levels of Fe<sup>2+</sup> ions (Burns, 1993). Being a transition element, iron has the unfilled external d-shell; hence, electrons placed on the five orbitals  $d_{xy}$ ,  $d_{yz}$ ,  $d_{xz}$  and  $d_{z^2}$  are weakly bound with the nucleus. When an Fe cation is placed in a crystal lattice, the orbitals due to their different shapes are disturbed differently by neighboring anions. The disturbance removes the degeneracy and the energy levels split, which allows quantum transitions with photon absorption. For orthopyroxene, for instance, the splitting produces two bands centered near 950 and 1800 nm. For olivine the splitting produces 3 overlapping bands near 1  $\mu\text{m}$ . The pyroxene and olivine bands are strongly overlapped near 1  $\mu\text{m}$ , producing a common asymmetric absorption structure.

In this paper we study optical properties of a region of the northwestern side of the Aristarchus Plateau using a small part of image cube M3G20090612T183813 (<https://pds-imaging.jpl.nasa.gov/volumes/m3.html>), which covers the area shown in Fig. 2.1 with a resolution of about 250 m/pixel. The scene comprises not only the NW portion of the Aristarchus Plateau and Montes Agricola, but also a small portion of Oceanus Procellarum. We chose this area because of its expected diversity in optical and, hence, geological properties. In particular, we here anticipate conspicuous variations in depths and positions of the 1  $\mu\text{m}$  and 2  $\mu\text{m}$  absorption bands. The correlation between the positions of the absorption bands is diagnostic for the determination of pyroxene types, e.g. to distinguish between ortho- and clinopyroxenes (McCord and Adams, 1973; Adams, 1974; Klima et al., 2007; 2011; Whitten and Head, 2015), as well as glasses (Adams, 1974; Besse et al., 2014; Horgan et al., 2014).

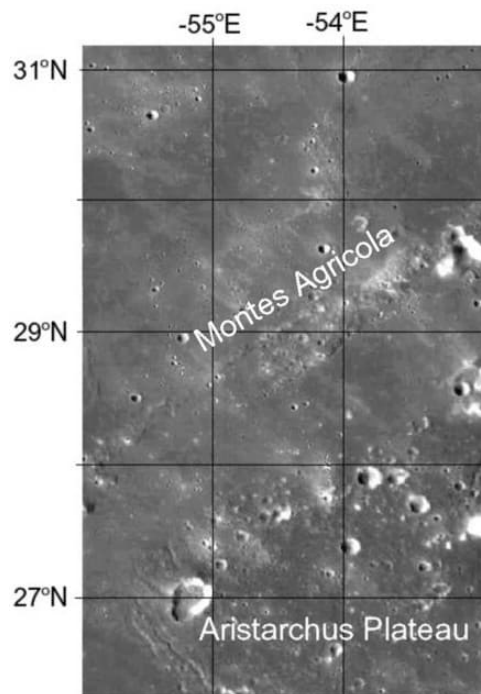


Figure 2.1. A NW portion of the Aristarchus Plateau. The image is adopted from <http://target.lroc.asu.edu/q3> with a spatial resolution of about 250 m at a phase angle near 90°; the frame width equals 80 km; the equidistant cylindrical projection is used. The image was acquired with the Clementine UVVIS camera.

The Aristarchus Plateau is among the most interesting sites on the Moon. It is located in the northwestern portion of the lunar nearside. The plateau is an elevated formation of about 170×220 km, which is surrounded by younger mare basalts of Oceanus Procellarum (Schultz 1975; Wilhelms 1987). The crater Aristarchus is located at the southeastern edge of the Aristarchus Plateau and is approximately 40 kilometers in diameter and 3.0 kilometers in depth; this crater is beyond the scene in Fig. 2.1. The plateau is noted to be rich in optical and geologic features (Gaddis et al. 1985). Dark mantling deposits (DMD) of the volcanic pyroclastic origin cover this plateau (e.g., Zisk et al. 1977; Gaddis et al. 1985; Wilhelms 1987). These deposits are especially dark in the UV spectral range, which were revealed more than 100 years ago by Wood (1911; 1912), who supposed that this optical feature might be a result of strong absorption of sulphur compounds. Later, this UV dark formation was unofficially named Wood's Spot. It is interesting to note that the boundary of the Aristarchus Plateau and Wood's spot are not coincident everywhere. We note also that the plateau has a thorium anomaly (Hagerty et al., 2009). According to LRO Diviner measurements, the Christiansen wavelength of the surface materials of the plateau and surrounding maria are similar (<http://target.lroc.asu.edu/q3>). A smaller abundance of rocks is observed on the plateau surface (<http://target.lroc.asu.edu/q3>). The scene includes also Montes Agricola (Fig. 2.1) that is a ridge. This continues for a distance of 160 km. The 20 km gap between the ridge and the plateau to the south is covered by mare basaltic flows.

For a further geological description and chemical/mineral characterization of the region, the Chandrayaan-1 M<sup>3</sup> spectrometer data could be very informative. Fig. 2.2 displays the scene shown in Fig. 2.1 in the context of M<sup>3</sup> measurements. The instrument M<sup>3</sup> is an imaging spectrometer working in a pushbroom operation. It uses a HgCdTe detector array. In each surface point, like S (see Fig. 2.2), a full



spectrum including 85 narrow spectral bands is measured. Thus, the data set is arranged as a cube with the spatial coordinates  $x$  (along the detector array) and  $y$  (along orbital movement) and the third coordinate  $\lambda$  (wavelength), which justifies the name  $M^3$  (Goswami and Annadurai, 2009; Pieters et al., 2009).

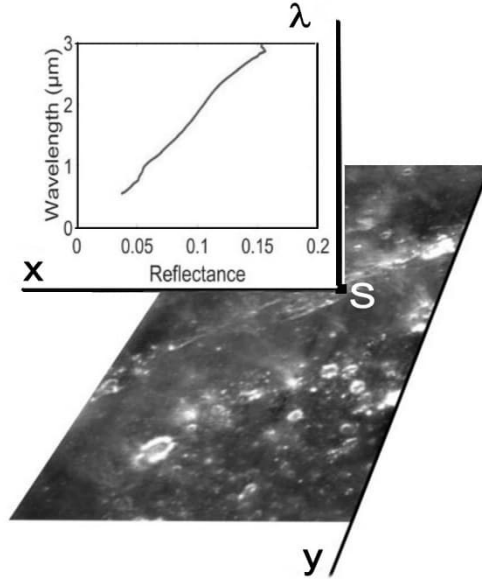


Figure 2.2. The scene shown in Fig. 2.1 is presented in the context of  $M^3$  measurements. Hereafter  $\lambda$  denotes a wavelength.

Because of some technical problems of the spacecraft (largely thermal), the  $M^3$  final images are burdened with a system of random vertical stripes, which significantly limit the data use for quantitative analysis. This especially becomes noticeable for derivative images, which involve multiple images. Fig. 2.3a,b illustrates this problem for distributions of the apparent albedo (reflectance)  $A(950 \text{ nm})$  (e.g., Hapke, 2012; Shkuratov et al., 2011) and the color ratio  $C(950 \text{ nm}/750 \text{ nm}) = A(950 \text{ nm})/A(750 \text{ nm})$  located in the upper left corner of the scene shown in Fig. 2.1. The clear vertical stripes have different intensity and length, and their system reveals faint periodicities. The stripes dramatically spoil derivative images such as the color ratio or more complicated combinations of spectral parameters, e.g., related to the depths and position of  $1 \mu\text{m}$  and  $2 \mu\text{m}$

bands. Fig. 2.3b shows the stripes dominating the lunar color ratio image, allowing only qualitative conclusions on mineralogy of the surface. The shortwave slope of the 1  $\mu\text{m}$  band characterized with the color ratio  $A(950\text{ nm})/A(750\text{ nm})$  is widely used for estimation of the FeO content and maturity degree of the lunar surface (Lucey et al., 1995; 2000; Shkuratov et al., 1999a; Pieters et al., 2006; Shkuratov et al., 2005; 2007). As can be seen, the image striation makes it almost impossible to calculate the local regolith characteristics with any accuracy.

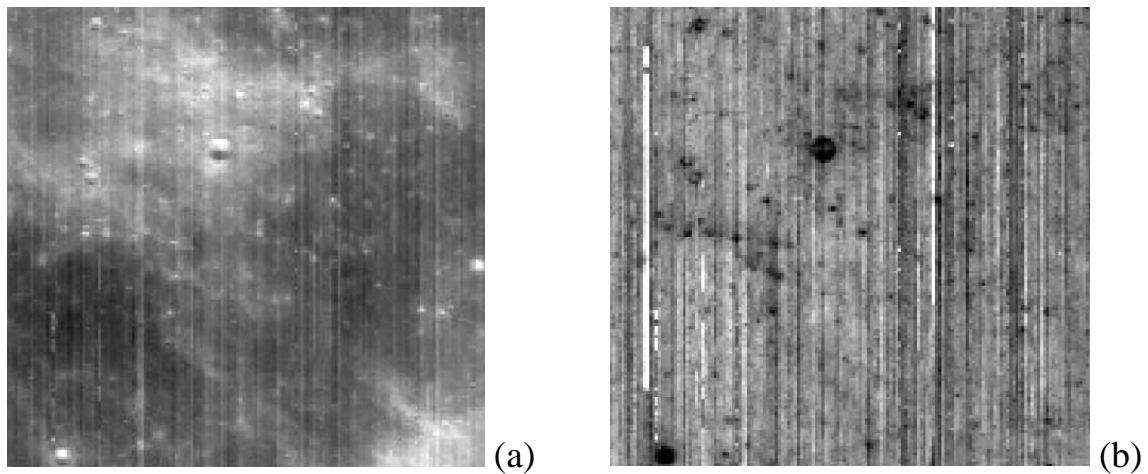


Figure 2.3. A portion of the scene located in the upper left corner of Fig. 2.1. The data were obtained with the Chandrayaan-1 M<sup>3</sup> scanning spectrometer (Pieters et al., 2009): (a) a brightness image acquired at  $\lambda = 950\text{ nm}$ , (b) a distribution of the color ratio image  $C(950/750) = A(950\text{ nm})/A(750\text{ nm})$ .

## 2.2 Additional data processing

In this paper we show that the current Chandrayaan-1 M<sup>3</sup> spectral data presented in <https://pds-imaging.jpl.nasa.gov/volumes/m3.html> can be significantly improved by means of suppressing the striation patterns of the images across the full spectral range.

### 2.2.1. Gaussian $\lambda$ -convolution

First, noticeable signal variations are found in neighboring wavelengths at the maximal spectral resolution at different points on the lunar surface. This effect is never observed in laboratory conditions, and therefore we may treat these variations as a random noise. We carried out a small scale smoothing of spectra through a convolution with a 1D Gaussian kernel. The kernel parameters were chosen empirically, considering that the quantitative criterion of their acceptability is the preservation of the mean over the image in each spectral channel with an accuracy of 0.2%. We here used the kernel width of about 4 spectral pixels on the level of the half-height of the Gaussian function. We did not use wavelengths larger than 2.6  $\mu\text{m}$ , since in this spectral range the number of spectral counts is small, and the smoothing may destroy the spectral structure attributed to the compounds OH/H<sub>2</sub>O (Pieters et al., 2009). Moreover, standard processing may result in a residual thermal component at wavelengths greater than 2.6  $\mu\text{m}$  and such wavelengths may not be sufficiently reliable. Fig. 2.4 illustrates the effect of the spectral smoothing. After the Gaussian  $\lambda$ -convolution, a spectrum obtained in one pixel from the scene shown in Fig. 2.1 almost does not change visually, but the ratio curve (pre/post smoothing) reveals that we nevertheless suppress the noise of several percents.

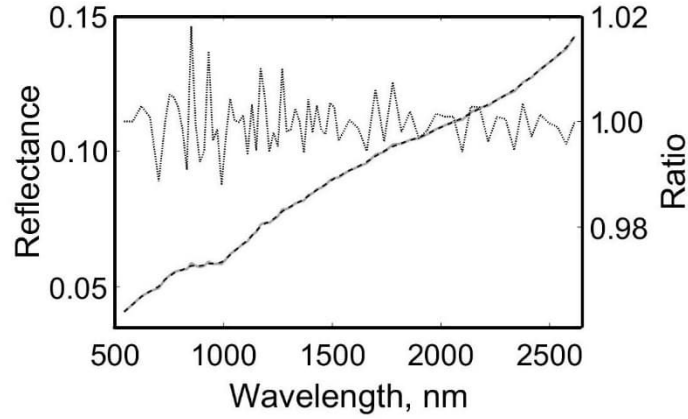


Figure 2.4. Spectrum obtained in one pixel from the scene shown in Fig. 2.1 before (solid line) and after (dashed line) smoothing and a ratio of the spectra (right scale).

Fig. 2.5 shows images before (a) and after (b) spectral smoothing. Although the stripe structure weakens after the smoothing, this does not disappear completely. To observe clearly the noise removed, we show the ratio of the images (a) and (b) in Fig. 2.5c. An important feature of such a ratio image should be the absence of details related to the Moon. It means we do not spoil the lunar scene, removing only noise.

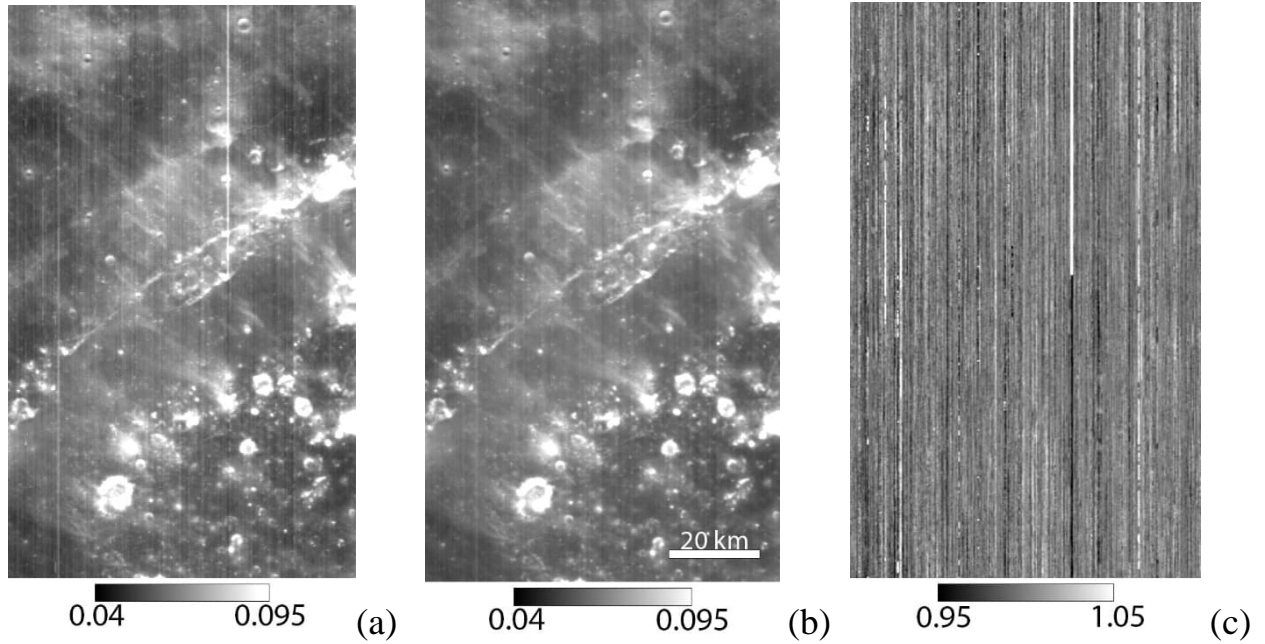


Figure 2.5. A portion of image M3G20090612T183813\_V03 before (a) and after (b) the described Gaussian  $\lambda$ -convolution. The image (c) is the ratio of (a) and (b). The image M3G20090612T183813\_V03 was obtained at  $\lambda=0.95 \mu\text{m}$ .

### 2.2.2 Fourier filtration

To further weaken the pattern of stripes, we use linear Fourier filtration. The idea of this filtration is as follows. First, we should produce a 2D Fourier transform of the reflectance image  $F(\omega_x, \omega_y)$  like that shown in Fig. 2.5a and b.

$$F(\omega_x, \omega_y) = \frac{1}{2\pi} \int_{-\infty}^{\infty} \exp(-i(\omega_x x + \omega_y y)) f(x, y) dx dy, \quad (1.1)$$

where  $\omega_x$  and  $\omega_y$  are the coordinates in the Fourier (spatial frequency) plane. Then, we may find frequencies responsible for the stripes in the Fourier plane and rejected them using the following simple filter.

$$\Lambda(C, \Omega, \omega_x, \omega_y) = \begin{cases} C, & \text{if } \omega_x, \omega_y \text{ are inside } \Omega \\ 1, & \text{if else} \end{cases}, \quad (2.2)$$

where  $C$  is a small constant,  $\Omega$  is the domain, where stripe frequencies are localized;  $C$  and  $\Omega$  are the filter parameters, providing rejection. After such a

filtration we may produce the inverse Fourier transform, resulting in an image without the stripe clutter.

$$f(x, y) = \frac{1}{2\pi} \int_{-\infty}^{\infty} \exp(i(\omega_x x + \omega_y y)) \Lambda(C, \Omega, \omega_x, \omega_y) F(\omega_x, \omega_y) d\omega_x d\omega_y, \quad (2.3)$$

Unfortunately, one cannot directly exploit Eqs. (2.1) - (2.3), because of the infinite limits in the integrals and the discrete presentation of images. Therefore, the Fourier integrals should be expressed in the following discrete form (e.g., Smith, 2002).

$$F_{p,q} = \sum_{j=0}^{m-1} \sum_{k=0}^{n-1} \exp(i(\omega_p j + \omega_q k)) f_{j,k}, \quad (2.4)$$

$\omega_p = -\frac{2\pi p}{m}$  and  $\omega_q = -\frac{2\pi q}{n}$  are the coordinates in the frequency plane,  $p = 0, 1, 2, \dots, m-1$ , and  $q = 0, 1, 2, \dots, n-1$ ,  $m$  and  $n$  characterize the image sizes in the number of pixels. Correspondingly

$$f_{j,k} = \frac{1}{mn} \sum_{p=0}^{m-1} \sum_{q=0}^{n-1} \exp(-i(\omega_p j + \omega_q k)) \Lambda(C, \Omega, \omega_p, \omega_q) F_{p,q}, \quad (2.5)$$

where

$$\Lambda(C, \Omega, \omega_p, \omega_q) = \begin{cases} C, & \text{if } \omega_p, \omega_q \text{ are inside } \Omega \\ 1, & \text{if else} \end{cases}, \quad (2.6)$$

Fig. 2.6 displays a 3D image of the Fourier spectra of the scene shown in Fig. 2.5b. The vertical axis is logarithmic. We may see, that the spatial spectra has a peak related to low frequencies that are responsible for the formation of the large scale lunar pattern of the image. We also see a comb, which is oriented along the  $p$  axis; it is a bit darker than the other points. This is a location of the vertical striation. The structure of the comb is clearly seen in Fig. 2.7 that is the vertical projection of the 3D surface shown in Fig. 2.6. One may see that actually there are several combs that are parallel to each other. In Fig. 2.7 we also show the domain  $\Omega$ .

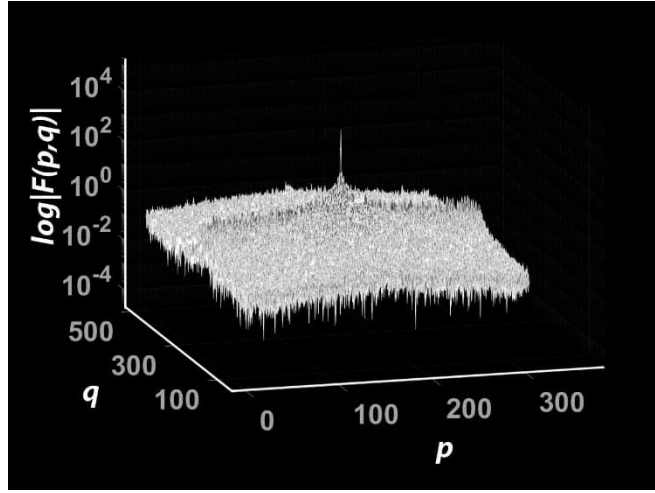


Figure 2.6. A 3D image of the Fourier spectra of the scene shown in Fig. 2.5b.

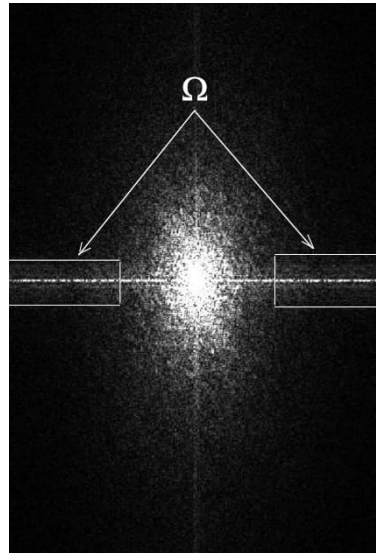


Figure 2.7. A Fourier spectrum of the image shown in Fig. 2.5b.

The filtration of the stripe structure has been carried out at  $C = 0$  inside the domain  $\Omega$ . The main selection criterion of the filter parameters is the disappearance of the stripe pattern or at least its visual minimization on the resulting image. Another important issue is the absence of features related to the Moon on the ratio image of the initial and filtered images. Additionally, by varying the parameter values we keep the average albedo of the scene within 0.2% of the

average for the original image. Fig. 2.8 shows images of the scene presented in Fig. 2.1 before (a) and after (b) application of both the Gaussian  $\lambda$ -convolution and the Fourier filtration of the stripe pattern. The resulting image (b) does not exhibit any detectable stripe pattern at all. The ratio (c) of the images (a) and (b) does not exhibit any lunar feature details.

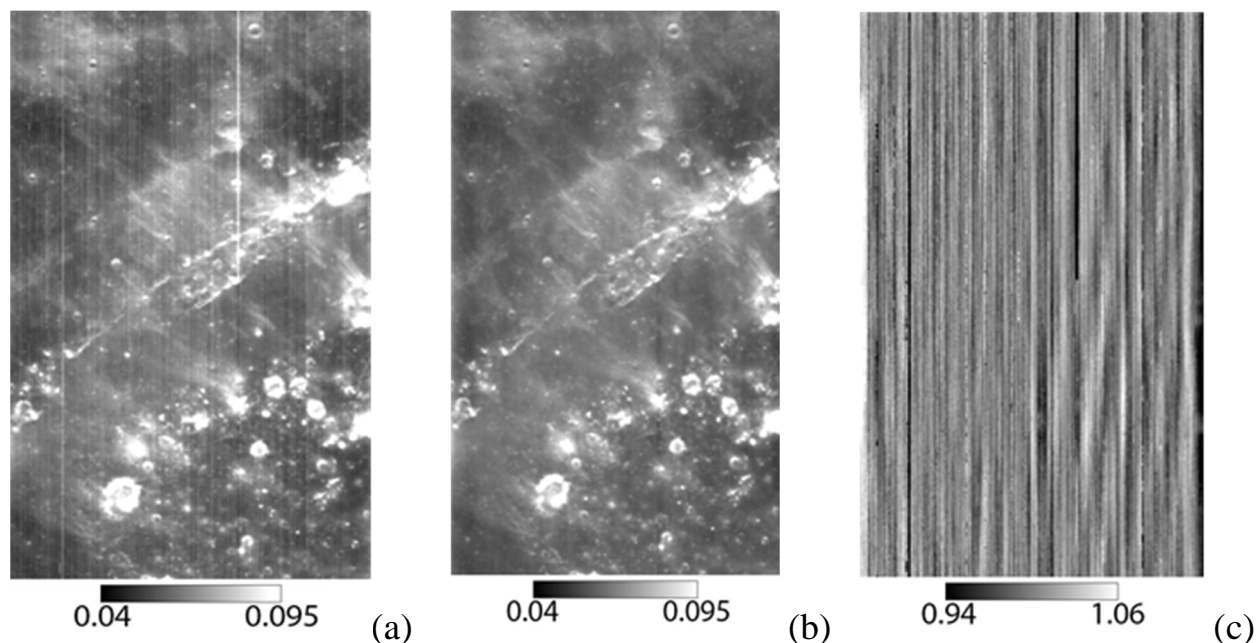


Figure 2.8. A part of image M3G20090612T183813\_V03 before (a) and after (b) Gaussian  $\lambda$ -convolution and Fourier filtration of the stripe pattern. The image was obtained at  $\lambda=0.95 \mu\text{m}$ , and the filter parameters are  $C = 0$ ; the image (c) is the ratio of ones marked as (a) and (b).

As has been noted, the main goal of the suggested processing development is to obtain derivative spectral images that can be applied to quantitative analyses of chemical/mineral composition of the lunar surface. Fig. 2.9 shows a distribution of the color ratio  $A(950 \text{ nm})/A(750 \text{ nm})$  and position  $\lambda_{\text{min}}$  of the  $1 \mu\text{m}$  band (see below), respectively, before [(a), (d)], after [(b), (e)] application only of the Gaussian  $\lambda$ -convolution, and after [(c), (f)] the Gaussian  $\lambda$ -convolution and Fourier filtering the vertical streaks. One may see the filtration effect is very prominent.



There is no difference which operation (Gaussian  $\lambda$ -convolution or Fourier filtering) is applied first. Although the images in Figs. 2.9b,d still reveal the faint stripe patterns, this shows up very weakly in comparison with the initial images (Fig. 2.9a,c). This technique allows us to make more comprehensive analysis of Chandrayaan-1 M<sup>3</sup> data (Kaydash et al., 2018), than has been done previously. We here focus on mapping the parameters of the 1  $\mu\text{m}$  and 2  $\mu\text{m}$  absorption structures.

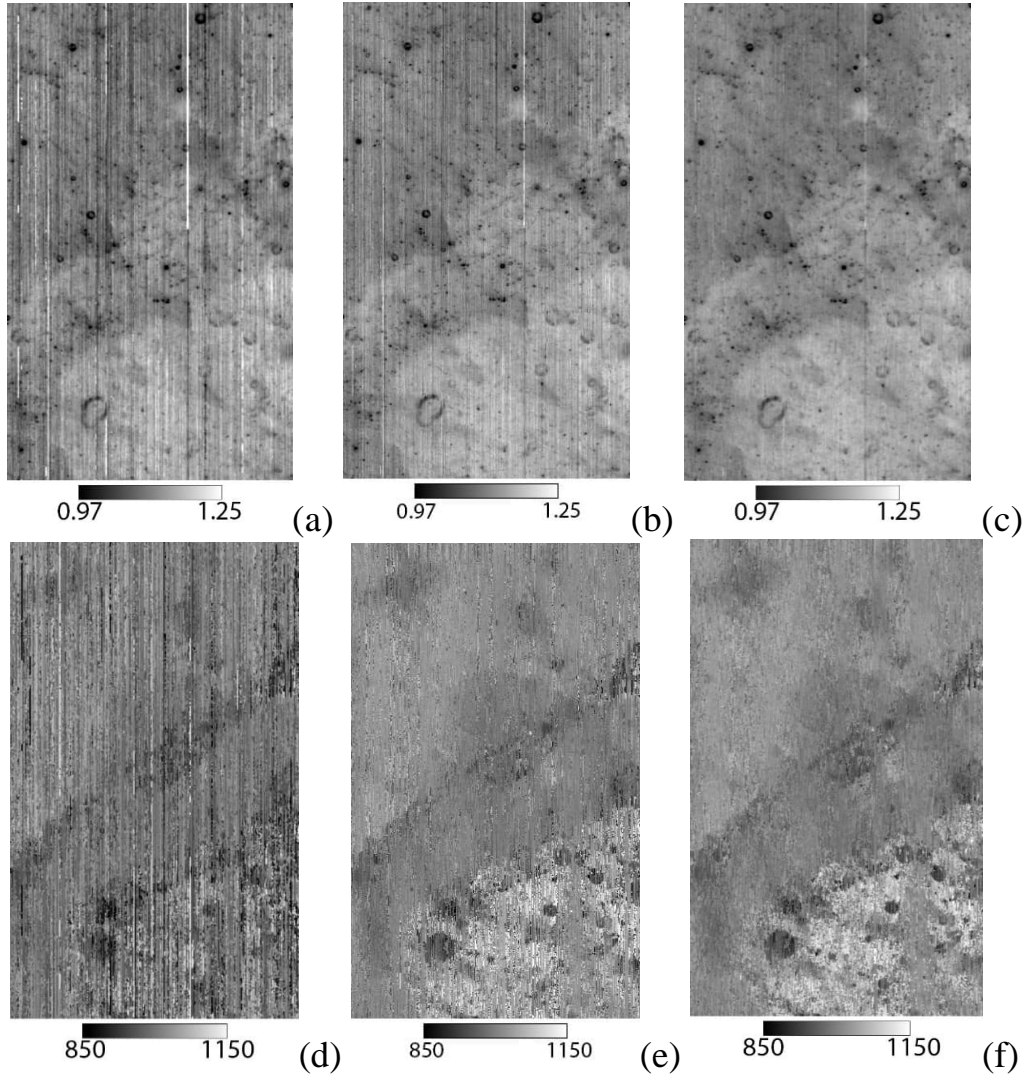


Figure 2.9. Distributions of the color ratio  $A(950 \text{ nm})/A(750 \text{ nm})$  before (a), after (b) using the Gaussian  $\lambda$ -convolution, and after (c) using the Gaussian  $\lambda$ -convolution and Fourier filtering vertical streaks; (d) – (f) the same for the band minima  $\lambda_{\text{min}}$  (in nm).

### 2.2.3 Band parameters

In lunar spectrometry, characteristics of absorption bands usually are investigated using reflectance spectra (e.g., Sunshine et al., 1990; Sunshine and Pieters, 1993). A more thorough method is based on the spectra of the absorption coefficient (e.g., Shkuratov et al., 1999a). Light scattering models for particulate media can be used for calculation of absorption spectra from reflectance spectra. The formula Kubelka-Munk or its modifications are often used (e.g., Myrek et al., 2011). Such models suggesting more physical results have been widely used as well (Hapke, 2012; Shkuratov et al., 1999b). Resulting band parameters, e.g., the minimum position, determined from reflectance and absorption spectra can be slightly different (Shkuratov et al., 1999b). Thus, a standardization of the band determination is necessary. Traditionally reflectance spectra are used initially, and we use them hereafter.

The following parameters: positions of the 1  $\mu\text{m}$  and 2  $\mu\text{m}$  bands ( $\lambda_{\text{min}}$ ), their depths, and general slopes of spectra in the 550 – 2600 nm range here are derived and exploited. Investigations of more complicated parameters, such as band asymmetry are very hard tasks even after the described data improvement. The listed parameters can be determined using different approaches. The approaches can be conditionally divided into two wide groups: parametric and nonparametric (Fu et al., 2007).

The first group is based on a representation of a spectrum as a set of isolated bands, the contours of which are described as a function with free parameters. The whole spectrum is the sum of these particular bands. The most suitable and widely used contour is the Gaussian function or its modifications (Sunshine et al., 1990; Sunshine and Pieters, 1993; Kaydash et al., 2018). The main advantage of such an approach is that each model band can be attributed to the absorption band of

definite chemical elements. However, this advantage is difficult to realize in practice, since the spectrum of the lunar regolith is not a direct linear combination of spectra of the constituent compounds.

Several non-parametric methods of continuum removal have been considered. For instance, one may normalize the overall trend of a full spectra to one single line, i.e. approximate the overall continuum with a linear function (e.g., McCord et al., 1972). This is a rough approximation and, therefore, results of this approach are imprecise. The second approach is to determine the edges of the absorption bands and then to separately remove the continuum for each spectral band. The key problem of the method is uncertainty in the positions of the band edges, since they indefinitely abut on the continuum and are not zero, especially where bands edges overlap. A more sophisticated approach is named the convex hull, which is often used in the spectroscopy for continuum removal (e.g., Graham, 1972; Fu et al., 2007; Martinot et al., 2018). In the case of a spectrum, the convex hull is the convex polygon, for which all spectrum points lie below the polygon or are its vertexes. In this approach, we use a simple Graham Scan algorithm (Graham, 1972) to compute convex hulls of spectra. Then we use only that part of the convex set which lies above the spectrum to remove the continuum. There are two methods to do this: through subtraction, i.e. an additive continuum correction, or through division, i.e. a multiplicative normalization. We here use the second approach.

Fig. 2.10 shows the location of two pixels marked by the rhomb and cross, spectra of which have different convexhulls (Figs. 2.11a,b). The dashed lines in Figs. 2.11a,b are the relative spectra after dividing by the convex hull. The difference between these two cases presented in Figs. 2.11a,b can be mapped. Fig. 2.10 displays a distribution of two kinds of areas. Marked with darker and brighter tones correspond to the hulls presented with a single line (Fig. 2.11a) and several

lines (Fig. 2.11b), respectively. As could be anticipated, there are rather large areas that reveal convex hulls more complicated than linear in the spectral range 550 - 2600 nm.

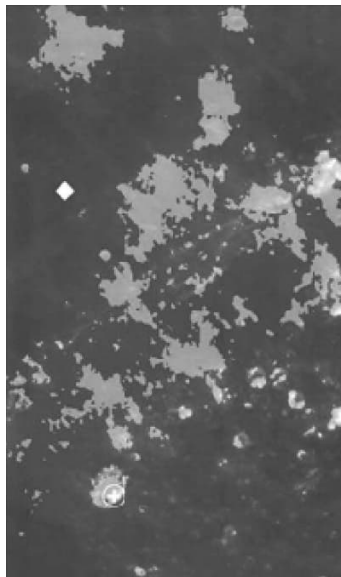


Figure 2.10. A distribution of the different types of the convex hull. The area marked with darker tones (rhomb) correspond to the case shown in Fig. 2.11a. The areas with more complex convex hulls (Fig. 2.11b) marked with brighter tones (cross).

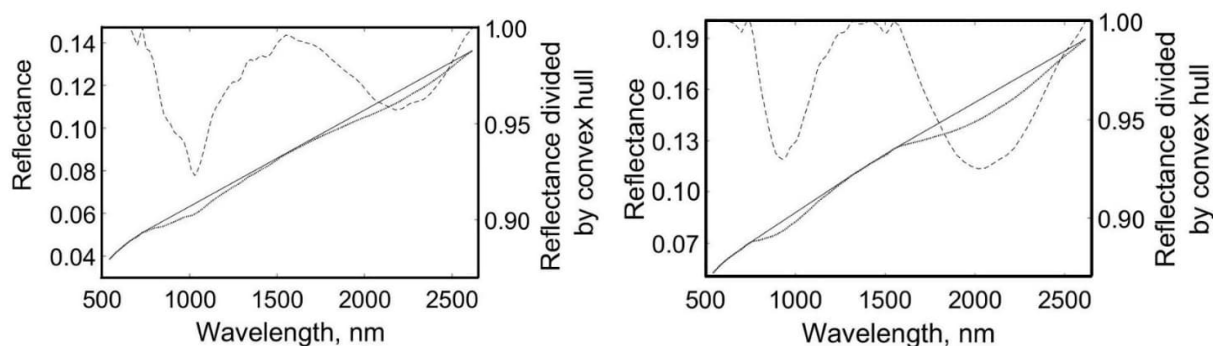


Figure 2.11. Spectra in the pixels shown by rhomb (a) and cross (b) in Fig. 2.10. The original reflectance spectra and their convex hulls presented by lines. The dashed lines are the spectra after dividing by the convex hull.

## 2.3 Results and discussion

### 2.3.1 Mapping band parameters

Using the Gaussian  $\lambda$ -convolution and Fourier filtration of Chandrayaan-1 M<sup>3</sup> images we produce maps of several color ratios for our test area. Fig. 2.12 represents distributions of the color ratios  $A(0.75 \mu\text{m})/A(0.54 \mu\text{m})$ ,  $A(1.30 \mu\text{m})/A(0.75 \mu\text{m})$ , and  $A(2.6 \mu\text{m})/A(1.7 \mu\text{m})$  in which a longer wavelength image is the numerator of the ratio. We note that all three images are fairly similar. The color ratio  $A(950 \text{ nm})/A(750 \text{ nm})$  (see Fig. 2.9b) also resembles the color ratios shown in Fig. 2.12. Bright young craters reveal smaller spectral slopes than other units; this effect is minimal for the color ratio  $A(0.75 \mu\text{m})/A(0.54 \mu\text{m})$ . The material located in the Aristarchus Plateau is the most red. Even mare material between the plateau and Montes Agricola (see Fig. 2.1) is red, although in the case of the ratio  $A(2.6 \mu\text{m})/A(1.7 \mu\text{m})$  this effect is smaller. This suggests noticeable difference of the chemical/mineral composition of this material and lava flows to the northwest of Montes Agricola. We may assume that the lava flooding between the plateau and the ridge were, perhaps, shallow and formed with involving the background (i.e., red) materials.

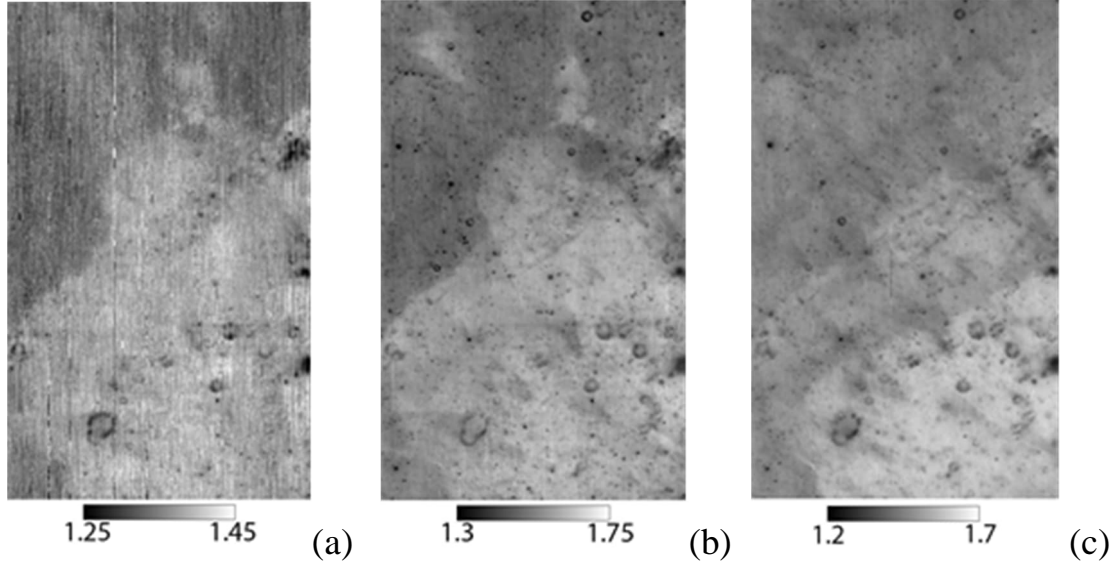


Figure 2.12. (a): Color ratio  $A(0.75 \mu\text{m})/A(0.54 \mu\text{m})$ ; (b): Color ratio  $A(1.30 \mu\text{m})/A(0.75 \mu\text{m})$ ; (c): Color ratio  $A(2.6 \mu\text{m})/A(1.7 \mu\text{m})$ .

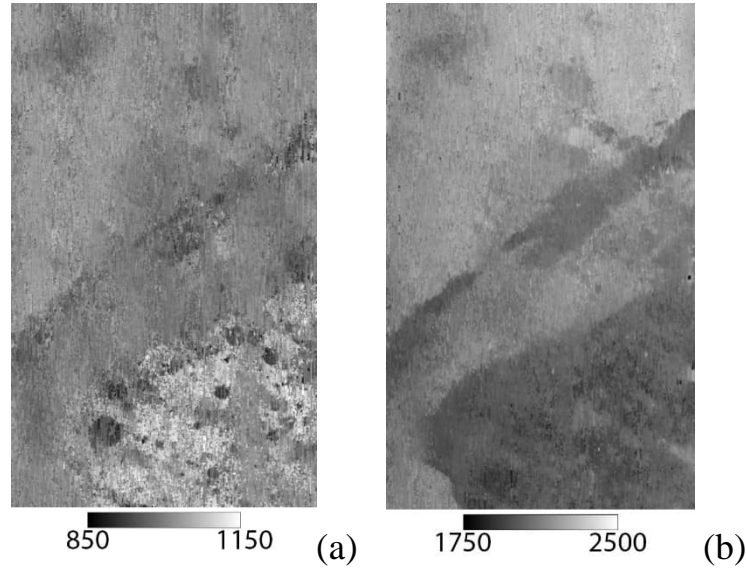


Figure 2.13. Position of  $\lambda_{\min}$  for  $1 \mu\text{m}$  (a) and  $2 \mu\text{m}$  bands. Scales are given in nm.

Fig. 2.13 demonstrates spatial variations of the positions of minima ( $\lambda_{\min}$ ) of the  $1 \mu\text{m}$  and  $2 \mu\text{m}$  spectral bands. This pair of parameters has been calculated using the convex hull method. Measurements near the minima have been approximated by a cubic spline, and then for each pixel of the scene, the minimum was calculated. Fig. 2.13 shows high quality images (especially in the case of the 2

$\mu\text{m}$  band) that are very rich in details. As distinct from the Montes Aglicola, the Aristarchus Plateau has fairly large values of  $\lambda_{\text{min}}$  for the 1  $\mu\text{m}$  band. According to laboratory spectral measurements (e.g., Adams, 1974), this is a characteristic of iron-bearing glasses. The plateau and Montes Agricola have relatively small values of  $\lambda_{\text{min}}$  for the 2  $\mu\text{m}$  band.

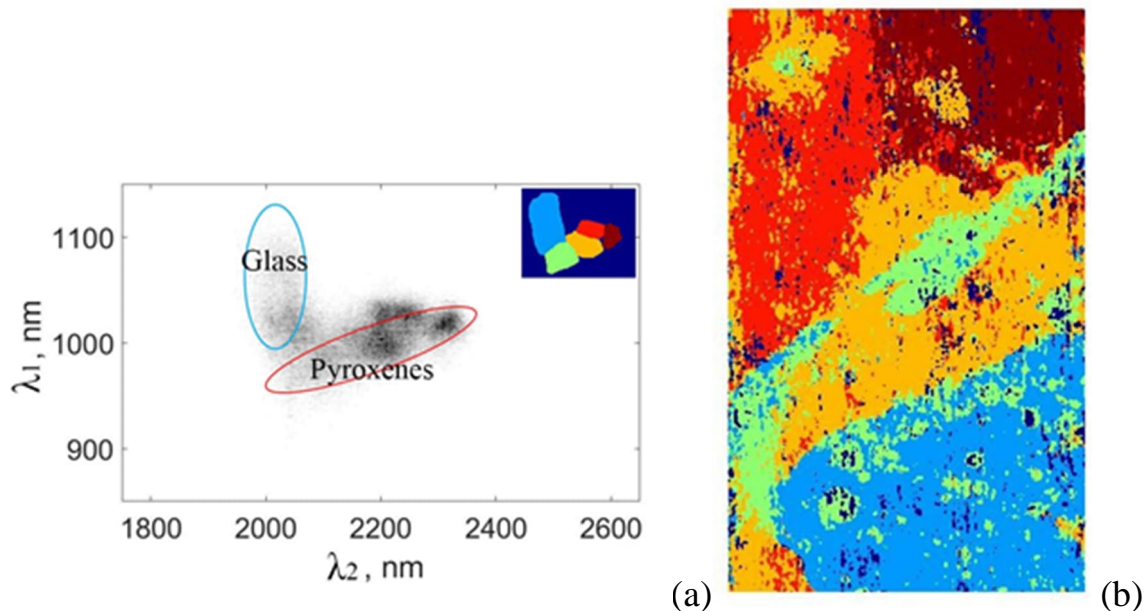


Figure 2.14. A correlation diagram between  $\lambda_{\text{min}}$  for 1  $\mu\text{m}$  (a) and 2  $\mu\text{m}$  bands (a); a map of optical glasses determined with the correlation diagram (b). To calculate the minima, we used cubic splines.

Fig. 2.14a shows a correlation diagram between the positions of the minima of the 1  $\mu\text{m}$  and 2  $\mu\text{m}$  bands. The diagram has a clear cluster structure that is diagnostic. In particular, its main domains can be classified as glass and pyroxene, deduced from laboratory measurements by Adams (1974) (see the ellipses on the diagram in Fig. 2.14a). In the upper right corner of the diagram, we show a legend to the classification map (Fig. 2.14b) corresponding to the clusters seen in the diagram. As we may observe, the materials of the Aristarchus Plateau include a large percentage of glasses, perhaps, of pyroclastic origin. The material of the lava

flows between the Aristarchus Plateau and Montes Agricola form a distinctive cluster in the diagram. This material can be found to the north of Montes Agricola. The red and brown clusters surprisingly divide the ordinary mare surface located to the north of the Aristarchus Plateau in two portions. Unclassified dark spots in the map occupy a small percentage of the area and can be ignored in the analysis.

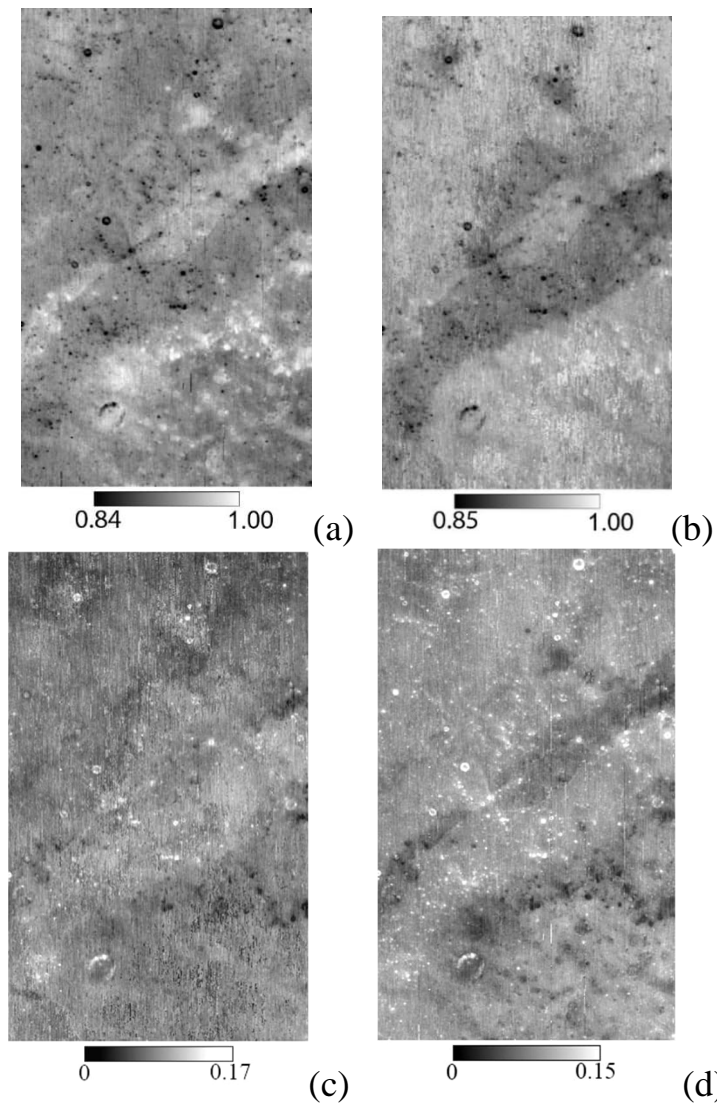


Figure 2.15. The maps of the depths of the 1  $\mu\text{m}$  (a) and 2  $\mu\text{m}$  (b) bands.

The depths of the 1  $\mu\text{m}$  and 2  $\mu\text{m}$  bands depend on pyroxene abundance, type of pyroxenes, and the maturity degree of the lunar surface. The depths were



calculated using the convex hull method and are shown in Fig. 2.15. We here used two definitions of the depth. The first one  $h_{\min}$  is counted from the lowest point in a band (Fig. 2.15a,b) and the second one is  $1-h_{\min}$  (Fig. 2.15c,d) that introduced by Clark (1983). These two pairs of maps reveal complicated patterns. The depths of bands 1  $\mu\text{m}$  and 2  $\mu\text{m}$  are weakly correlate with each other independently of the band depth presentation (e.g., Fig. 2.16). The images of the band depths almost do not correlate with the maps of the band minimum positions shown in Fig. 2.13. The 2  $\mu\text{m}$  depth distribution (Fig. 2.15b) appears almost insensate to the craters on the Aristarchus Plateau, but in the representation of Fig. 2.15d the craters can be seen very well. Craters with immature regolith having deep 2  $\mu\text{m}$  bands (dark spots in Fig. 2.15b) can be observed on the surface to the northwest of the Aristarchus Plateau. In some measure the 1  $\mu\text{m}$  depth distribution shows the same features (Fig. 2.15a), although some craters here look like bright spots on the Aristarchus Plateau. The lava materials lying between Montes Agricola and the plateau have larger values of the depth of 2  $\mu\text{m}$  band; whereas, the 1  $\mu\text{m}$  band has here no peculiarities.

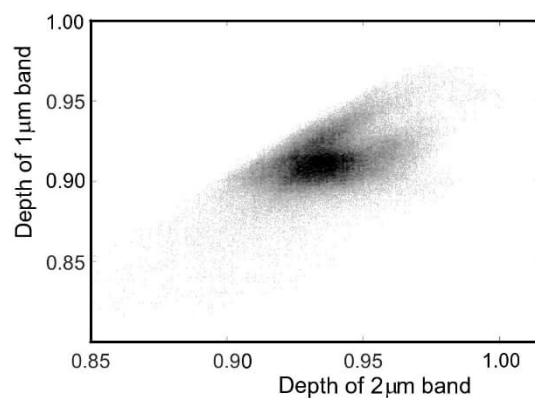


Figure 2.16. A correlation diagram of the depths of the 1  $\mu\text{m}$  and 2  $\mu\text{m}$  spectral bands.

The examples described in this section show that quantitative information can be obtained from the Chandrayaan-1 M<sup>3</sup> images of the Moon in the parameters, such as  $\lambda_{\min}$  and band depths  $h_{\min}$  of both the spectral bands, if the Gaussian  $\lambda$  - convolution and Fourier filtration are applied. It should be emphasized that the depth distribution of the 1  $\mu\text{m}$  band (Fig. 2.15a) and the corresponding color ratio  $A(950\text{ nm})/A(750\text{ nm})$  (Fig. 2.9b) do not show a significant correlation, which suggests that the color ratio determined using the shortwave wing of the band is not an adequate characteristic of band depth variations of the pyroxene bands.

### **2.3.2 Geologic characterization**

We here present a geological description of the region under study in order to show relationships with the maps of the spectral parameters. We use mosaics produced from Kaguya images (resolution is  $\sim 7\text{ m/px}$ ) and the 750 nm reflectance map constructed from the Kaguya multiband imager (Ohtake et al., 2013) to describe the composition of the region. The standard procedure of photogeologic analyses reveals that two major types of deposits make up the area: (1) autochthonous materials form the main geological bodies of the Aristarchus Plateau and its immediate surrounding maria and (2) surficial deposits that are related to both ejecta and ray systems of remote craters and the emplacement of dark mantling materials likely related to pyroclastic activity (Head, 1974; Gaddis et al., 1985, 2000, 2003; Weitz et al., 1998).

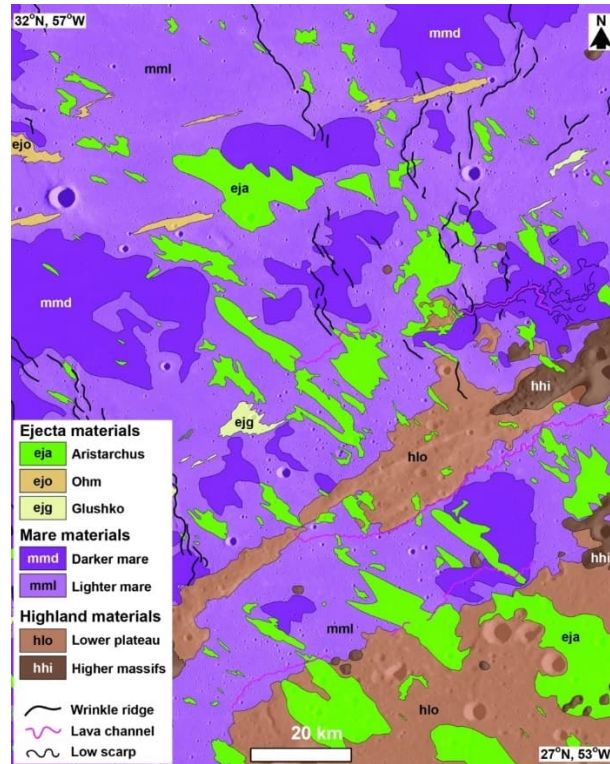


Figure 2.17. A geological map of the studied region.

The highland autochthonous deposits include two material units in our geological map shown in Fig. 2.17. The first one corresponds to high-standing massifs (designated *hhi*) that occur as isolated, approximately equidimensional hills (usually 5-6 km across) with morphologically smooth slopes. The height of the largest hills is ~500-600 m; one of them corresponds to Mons Herodotus at the eastern margin of the map area, which is ~800 m high. The hills are scattered throughout the NW portion of the Aristarchus Plateau, form the SW end of Montes Agricola, and occur within the mare area between the Aristarchus Plateau and Montes Agricola (Zisk et al., 1977). The shape of these *hhi* units suggests that they represent exposures of blocky ejecta of basin-like impact events; some of them may be related to the Imbrium impact. Occurrences of the *hhi* units at the edges of Montes Agricola correspond to pIr units, pre-Imbrian rugged material, shown in different localities in the geological map of the near side of the Moon (Wilhelms

and McCauley, 1971). The second units correspond to lower highland terrains (designated *hlo*) form the majority of the Aristarchus Plateau within the map area and the main portion of Montes Agricola. This unit represents dark mantling materials of uncertain age from Imbrian to Copernican (Wilhelms and McCauley, 1971). We ascribe the index *hlo* to a complex of materials underlying an apparently thin veneer of dark mantling material. This unit has a gently undulating surface with typical topographic variations ~100-200 m, except for the larger (>2-3 km) impact craters that are several hundred meters deep. Materials of the *hlo* unit embay the high-standing massifs of the *hhi* unit and are younger. This unit probably represents a mixture of the Imbrium ejecta and volcanic materials related to volcanic activity in the Aristarchus Plateau.

Mare autochthonous deposits in the NW portion of Oceanus Procellarum embay the highlands of the Aristarchus Plateau and Montes Agricola. Morphologically, the mare surfaces appear to be homogenous. The 750 nm reflectance map allows us to define conditionally two types of materials within the maria: darker and brighter deposits (Fig. 2.17). The latter (*mmb* unit) form the surroundings of the Aristarchus Plateau. This unit mostly coincides with the Im unit, designating Imbrian mare material (Wilhelms and McCauley, 1971). The surface of *mmb* unit is morphologically smooth, without evidence of individual lava flow fronts recognizable at the Kaguya resolution (~7 p/px). Systems of wrinkle ridges oriented in the meridional direction deform the surface of the mare deposits. The darker mare deposits (*mmd*) form isolated equidimensional and elongated patches a few tens of kilometers across. The largest areas of the *mmd* unit are localized within the basin-like topographic depressions near the western edge of the map area where they correspond to the Em unit, designating Eratosthenian mare material (Wilhelms and McCauley, 1971). Near the eastern edge of the map, an occurrence of the darker plains is spatially associated with a

lava channel (Rima Cleopatra) and is confined within local topographic depression. In this area, materials of the darker plains (*mmd*) embay the brighter plains (*mmb*).

Surficial deposits in the area occur as dark pyroclastic mantles that overlay some portion of the Aristarchus Plateau (Fig. 2.17) and as bright patches, elongated strips, and clusters of small (a few hundred meters) secondary craters consistently oriented in several directions and representing ejecta of remote craters. The dark mantles, seen better at high Sun, are confined within the Aristarchus Plateau and show no evidence of possible source features. Three types of bright surficial deposits represent materials ejected from the rather fresh impact craters. The most abundant are ejecta from the crater Aristarchus (23.8°N, 47.5°W, 39 km diameter, unit *eja*). Materials ejected from craters Glushko (8.1°N, 77.7°W, 39.5 km, unit *ejg*) and Ohm (18.4°N, 113.8°W, 61.8 km, unit *ejo*) occur exclusively within the mare deposits northward of Montes Agricola. All the units are formed by either clusters of secondary craters or elongated strips of brighter material.

### 2.3.3 Age assessments

In planetary geology, the absolute model ages (AMA) of units defined and mapped at a specific resolution are derived from crater size-frequency distribution (CSFD) measurements. This technique, including a discussion of model assumptions, strengths and shortcomings, and an error analysis, has been summarized in detail elsewhere (e.g., Neukum et al., 2001; Hiesinger et al., 2000, 2010; Wagner et al., 2002; Michael and Neukum, 2010) and is beyond the scope of this work. In our study, we seek chronological constraints of volcanic and impact events that caused the formation of a complex of deposits surrounding the Aristarchus Plateau and Montes Agricola. In order to obtain these constraints, we have counted craters using the WAC photo mosaics with resolution 100 m/px

(Robinson et al., 2010). The relatively low resolution of these images reduces the effects of the small-scale resurfacing events and contamination of the count areas by small (less than  $\sim 300$  m) secondary craters. Clusters of the larger secondary craters are clearly seen in the WAC mosaics and have been excluded from the count areas. In our study, we counted craters using the CraterTools application to the ESRI ArcGIS (Kneissl et al., 2010) and approximated the size-frequency distribution curves using the CraterStats program (Michael and Neukum, 2010), which applies the chronology by Neukum et al. (2001) and production functions to fit the curves. Our study area includes only a small portion of the Aristarchus Plateau, which may not be representative of the entire complex structure. Because of this, we adopt the Lower Imbrian age, 3.8 Ga (Zisk et al., 1977) for the units (*hhi* and *hlo*) that make up the Aristarchus Plateau in the study region.

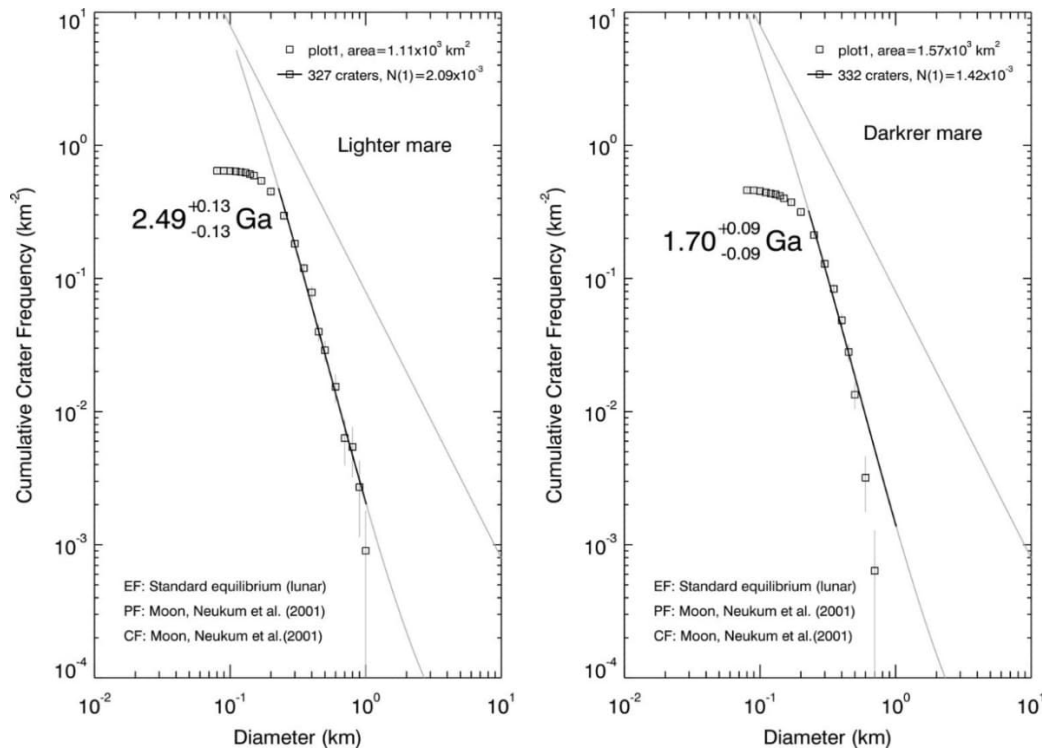


Figure 2.18. Absolute model ages of the brighter (a) and darker (b) mare units. PF and CF are the production and calibration functions, respectively.

The surfaces of the mare units (*mmb* and *mmd*) appear to be at slightly different elevations, with the darker plains (*mmd*) being preferentially confined within local topographic depressions. These topographic positions of the mare units suggest a younger relative age of the darker plains. We conduct the CSFD measurements within five individual fields of the darker plains and three fields of the brighter plains. The areas of the fields range from ~170 to 690 km<sup>2</sup>. When all recognizable craters have been mapped and counted, the areas corresponding to each specific mare unit were merged in order to increase the total number of craters and, thus, the reliability of the AMA estimates. The isochron fitting of the CSFD curves within the merged areas gives the model ages of  $2.49 \pm 0.13$  Ga and  $1.70 \pm 0.09$  Ga for the brighter (*mmb*, Fig. 2.18a) and darker (*mmd*, Fig. 2.18b) plains, respectively. These values are close to the AMA of unit P53 of  $1.68 \pm 0.3/-0.12$  Ga determined from Clementine spectral data (Hiesinger et al., 2003). The spectral data, however, have lower spatial resolution that prevented division of a single spectral unit into a set of finer subunits. Our AMA determinations for the lava plains to the north of the Aristarchus Plateau completely overlap the range of ages of mare units to the south of the Plateau, from  $2.81 \pm 0.38/-0.61$  Ga to  $1.03 \pm 0.16$  Ga, determined from the crater counts on the WAC mosaics (Stadermann et al., 2018).

We also perform a photometric characterization of the region to provide independent qualitative assessments of the ages of the geologic formations seen in Fig. 2.17. The technique is based on mapping the phasefunction parameters. This has been described in detail by Korokhin et al. (2014; 2016a; 2018) and Shkuratov et al. (2016). The NASA Lunar Reconnaissance Orbiter mission (LRO) allows high quality data for lunar photometric studies (Robinson et al., 2010). The spacecraft is equipped with the wide angle camera (WAC). The camera images the lunar surface in the visible (415, 566, 604, 643, and 689 nm) spectral range,

ensuring multiple coverage of the same areas at different illumination and observation angles. We here use images acquired at  $\lambda = 689$  nm as source data to determine photometric parameters of the studied area. Parameters characterizing the optical micro-roughness were mapped with a resolution of approximately 90 m. To approximate the phase angle dependence of the apparent albedo  $A(\alpha, i, e)$ , we use a 3-parameter empirical equation suggested by Korokhin et al. (2016b)

$$A(\alpha, i, e) = A_0 \exp(-\eta \alpha^\rho) \cos \frac{\alpha}{2} D(\alpha, i, e), \quad (2.7)$$

although modifications of this equation have been considered theoretically (e.g., Shkuratov et al., 1994; 2018a), where  $A_0$  is the normal albedo (its pattern is very similar to  $A$ ),  $\eta$  is the parameter of phase curve slope, and  $\rho$  is the characteristic of nonlinearity of the phase curves. We here use Akimov's disk function as the most reliable in lunar photometry (Shkuratov et al., 2011):

$$D(\alpha, \beta, \gamma) = \cos \left( \frac{\pi}{\pi - \alpha} \left( \gamma - \frac{\alpha}{2} \right) \right) \frac{(\cos \beta)^{\alpha/(\pi - \alpha)}}{\cos \gamma}, \quad (2.8)$$

where the photometric (luminance) coordinates  $\alpha$ ,  $\beta$ , and  $\gamma$  are the phase angle, and photometric latitude and longitude, respectively. The angles  $\beta$  and  $\gamma$  can be expressed through the incident and emerging angles  $i$  and  $e$  using the following formulas (e.g., Hapke, 1993; Shkuratov et al., 2011):

$$\begin{aligned} \cos i &= \cos \beta \cos(\alpha - \gamma), \\ \cos e &= \cos \beta \cos \gamma. \end{aligned}, \quad (2.9)$$

We calculate distributions of the parameters  $A_0$  and  $\eta$  for each point of the lunar surface in the scene using the mean square method and hundreds of LROC WAC images acquired at different  $\alpha$  from a range of 7–80°. These images were accurately coregistered with each other. The value of parameter  $\rho$  is fixed 0.6; the average number of points for the phase curve approximation is about 100. A detailed description of the processing is presented by Korokhin et al. (2014,



2016a,b, 2018). Maps of the parameters  $A_0$  and  $\eta$  are shown in Figs. 2.19a,b. It should be emphasized that images are seamless mosaics, which were produced with the technique described by Korokhin et al. (2014, 2016a,b, 2018), which takes into account many different factors including the local surface topography. The algorithm used in this work has been somewhat modified (Korokhin et al., 2018). Instead of using the longitudinal component of the topography slopes calculated from the external DEM, we fit them simultaneously with parameters  $A_0$  and  $\eta$  ( $\rho$  is fixed 0.6) directly in the optimization procedure (see Fig. 2.19c). In other words, we use a photoclinometry technique that produces better quality maps of  $A_0$  and  $\eta$ , and suggests independent information about topography of the scene under study.

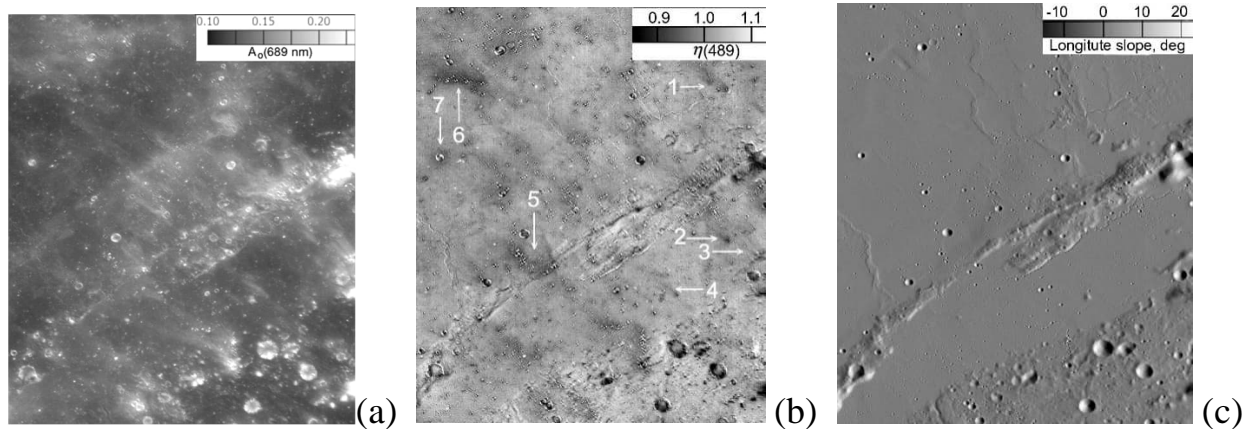


Figure 2.19. Results of photometric retrieval of the normal albedo  $A_0$  (a), the parameter  $\eta$  (b), and calculated topography using Eqs. (2.7) and (2.8), for a portion of the area under study. Dark tones in Fig. 2.19b correspond with smooth areas.

The parameter  $\eta$  characterizes optical roughness of the surface. Rougher surfaces have higher values of  $\eta$ , assuming they have the same albedo. At higher albedo, the parameter  $\eta$  is reduced due to multiple scattering in the lunar regolith (Kaydash et al., 2012, 2014; Shkuratov et al., 2012, 2016; Velikodsky et al., 2016). Fig. 2.19b does not reveal a conspicuous difference in roughness between mare

and plateau areas, although the plateau surface seems rougher in the topography image (Fig. 2.19c). This suggests the absence of formations with the young surface, as in the case of the crater Giordano Bruno (Shkuratov et al., 2012). Traces of surface erosion of elevated topographic formations are clearly seen in Figs. 2.19a,b (arrows 1-4). These are probably the result of ejecta hits from the craters Aristarchus, Ohm, and Glushko (Shkuratov et al., 2018b). We also point to two areas that are not obviously connected with an albedo feature (arrows 5 and 6). Finally the ejecta deposits around a fresh crater are shown by arrow 7. All these areas are smooth in terms of Eq. (2.7). It should be noted that correlation of the optical roughness  $\eta$  and albedo is unexpectedly weak.

#### **2.3.4 Relationships between spectral and geological data**

It is interesting to establish relationships between optical and geological data for this area. Using Adam's  $\lambda_{\min-1} - \lambda_{\min-2}$  diagram, we can find in it the localizations of the geological provinces. Results of such investigations are shown in Fig. 2.20. The grey color corresponds to the whole scene, and the dark color represents a particular geological formation. Thus, dark spots in Figs. 2.20a,b correspond to the areas of the Aristarchus Plateau and Montes Agricola, respectively. In spite of the morphologic similarity, their positions in the diagram are a bit different. The darker (*mmd*) and lighter (*mmI*) maria are almost in the same location of the diagrams (Figs 2.20c,d).

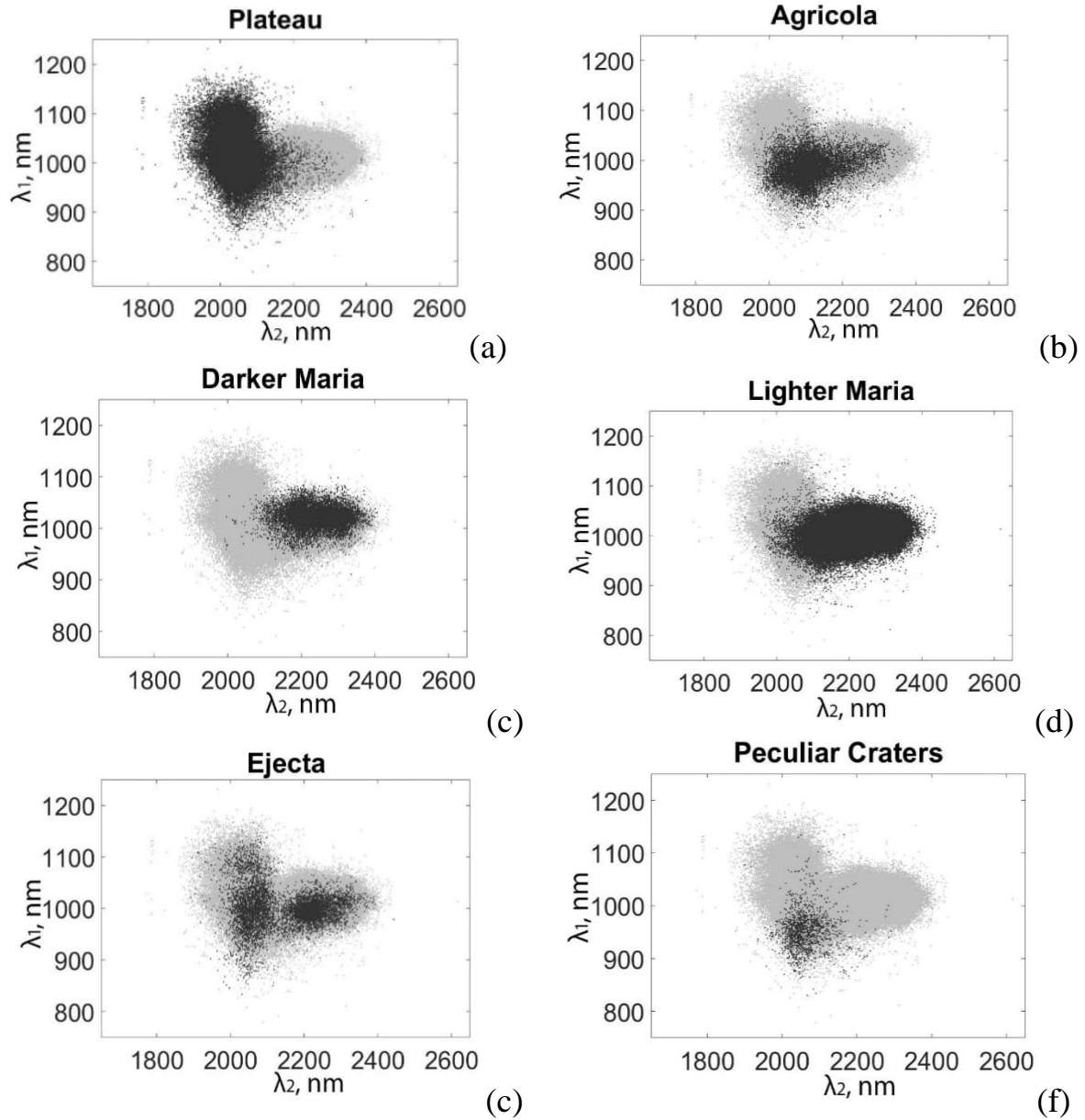


Figure 2.20. Relationships between spectral and geological data in correlation diagrams.

The ejecta materials (*eja*, *ejo*, and *eja*) are presented in different locations in the diagram depending on where they are located on the surface. The ejecta placed on the plateau and mare regions can be seen inside the plateau and mare clusters, respectively (Fig. 2.20e). We additionally consider a group of craters sited on the

Aristarchus Plateau (Fig. 2.21). As can be seen in Fig. 2.20f, the craters form a faint cluster located in the lowest portion of the diagram.

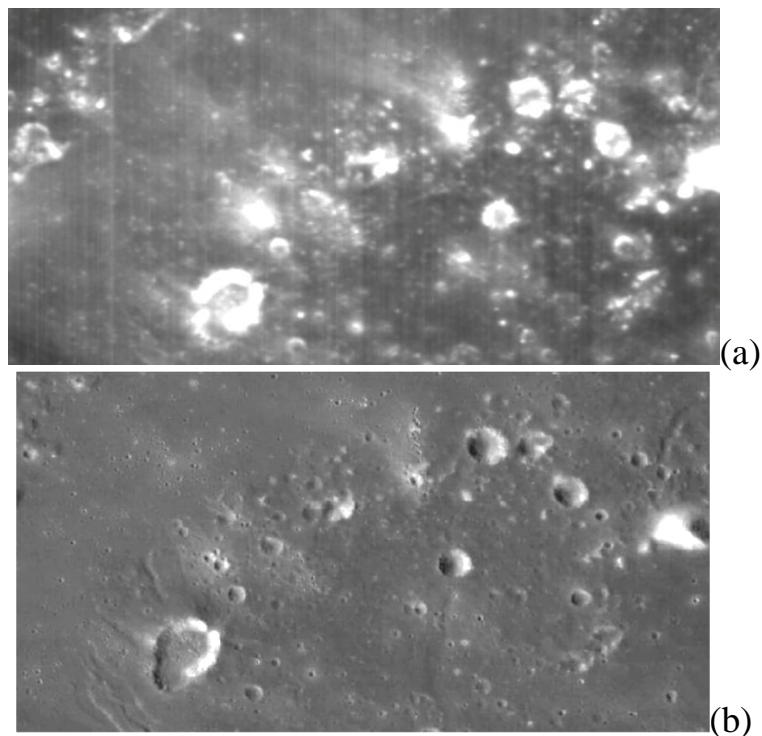


Figure 2.21. This group of bright craters with unusual 1- $\mu$ m band positions were used to build the cluster in Fig. 2.20f; (a) and (b) show, respectively, a fragment of the bottom portion of the image shown in Fig. 2.5b, and a related topography picture taken from <https://quickmap.lroc.asu.edu>

The diagrams presented in Fig. 2.20 help to assess the possible nature and timing of the formation of various materials composing the Aristarchus Plateau, Montes Agricola, and the surrounding maria. Although the Aristarchus Plateau and Montes Agricola represent parts of apparently the same morphological complex, their spectral characteristics are different (Fig. 2.20a,b). The characteristic points that represent the surface of the Aristarchus Plateau form a dense cloud, which is almost completely confined within the glass branch of the Adams diagram (Fig. 2.20a). In contrast, the points corresponding to Montes Agricola are preferentially concentrated within the pyroxene branch of the diagram (Fig. 2.20b). These

spectral differences of morphologically similar units likely reflect a predominant concentration of glassy pyroclastic particles within the plateau, whereas the area of Montes Agricola is deficient of pyroclastic materials. It is in agreed with lower albedo of plateau areas that are beyond craters in comparison with Montes Agricola. This suggests that the explosive volcanic activity was located mostly within the plateau, and its deposits did not reach the nearby massif of Montes Agricola. The pyroxene branch of the Adams diagram, thus, may characterize the pre-pyroclastic composition of the plateau highlands.

In developing the comparison of geological and optical data, we study correlation coefficients of albedo at different wavelengths for the different provinces. That is for each combination of wavelength and from the range 540-2617 nm, we calculate the correlation coefficient using all the pixels in the scene and then construct a diagram that we show in Fig. 2.22. This results in a fanciful pattern that is symmetrical relative to the bisector, on which the correlation coefficient is maximal and equals 1. The contours of equal correlation coefficient are not regular; e.g., the contours extend from the bisector toward the 1  $\mu\text{m}$  and 2  $\mu\text{m}$  bands. It means that in the spectral subranges centered near 1  $\mu\text{m}$  and 2  $\mu\text{m}$  spectra of the pixels of the scene are variable.

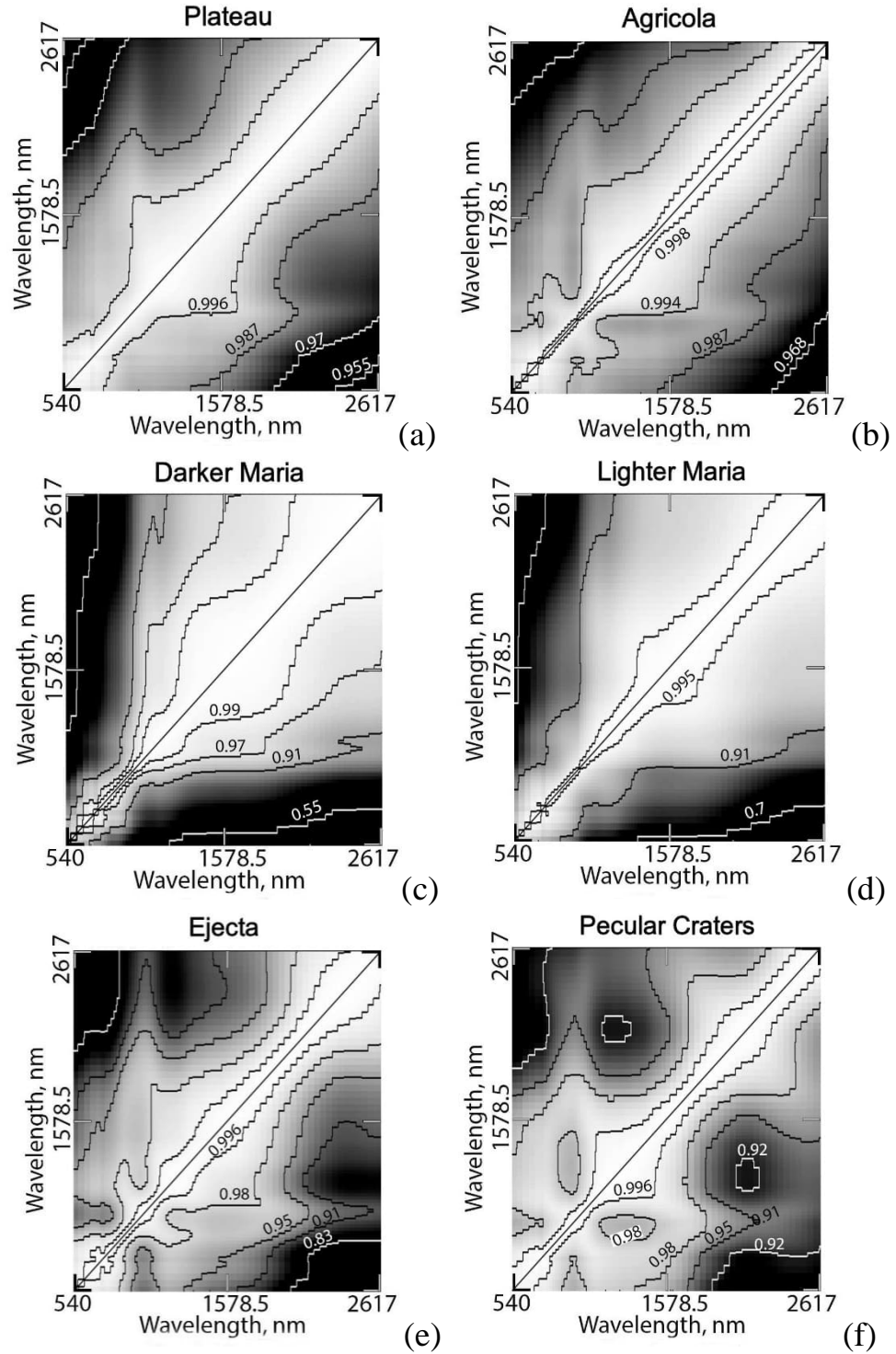


Figure 2.22. Correlation coefficient diagrams of albedos at different wavelengths for different geological provinces.

As can be seen from Fig. 2.22a-f the correlation coefficient diagrams are different for different geological provinces. We see that the Aristarchus Plateau and Montes Agricola have noticeably different diagrams: the variability of the 1  $\mu\text{m}$  band is higher for Montes Agricola. The diagrams for lighter and darker maria are fairly similar, but clearly distinct from the Aristarchus Plateau and Montes Agricola. The materials of the ejecta deposits and peculiar craters that are in Fig. 2.21 have variable 2  $\mu\text{m}$  band, which are not the case of all the former diagrams. The spectral variability near 1  $\mu\text{m}$  is also high. Thus, the diagrams of the correlation coefficients suggest unusual, but useful information.

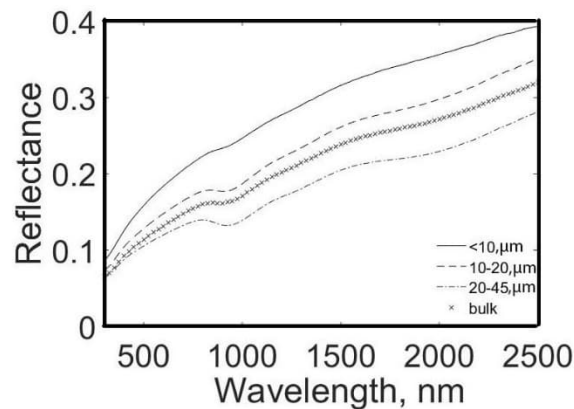


Figure 2.23. Average spectra of LSCC samples

<http://www.planetary.brown.edu/relabdocs/LSCCsoil.html>

It is interesting to compare the lunar correlation coefficient diagrams with the analog those for lunar samples. We exploit here spectral data obtained by the Lunar Sample Characterization Consortium (LSCC) (Taylor et al., 1999, 2001; Pieters et al., 2002, 2006) that include regolith samples selected to be representative of various lunar basalt compositions having different maturity. Since the optical properties of lunar soils are controlled by the smaller size fractions (Pieters et al., 1993) and space weathering processes (Pieters et al., 2000), the

LSCC concentrated on detailed analysis of the  $< 45 \mu\text{m}$  components of lunar soils. Coordinated compositional and spectral measurements of the samples were carried out for soils subdivided into three size fractions ( $< 10 \mu\text{m}$ ,  $10\text{--}20 \mu\text{m}$ , and  $20\text{--}45 \mu\text{m}$ ) in addition to a “bulk”  $< 45 \mu\text{m}$  sample (Taylor et al., 2001). Altogether the LSCC analyzed 52 samples of different size fractions. Bidirectional spectra of a high spectral resolution were acquired for each subsample in the RELAB at Brown University. All spectra were measured over the spectral range  $0.3\text{--}2.6 \mu\text{m}$  with a  $5 \text{ nm}$  sampling resolution at a phase angle of  $30^\circ$  ( $i = 30^\circ$ ,  $e = 0$ , the angles of incidence and emergency, respectively) (Pieters and Hiroi, 2004). Examples of LSCC spectra averaged for each size fraction are shown in Fig. 2.23. As anticipated, the bulk spectrum lies between the fine and coarse fractions. All the separate spectra used and composition data are available at <http://www.planetary.brown.edu/relabdocs/LSCCsoil.html>.



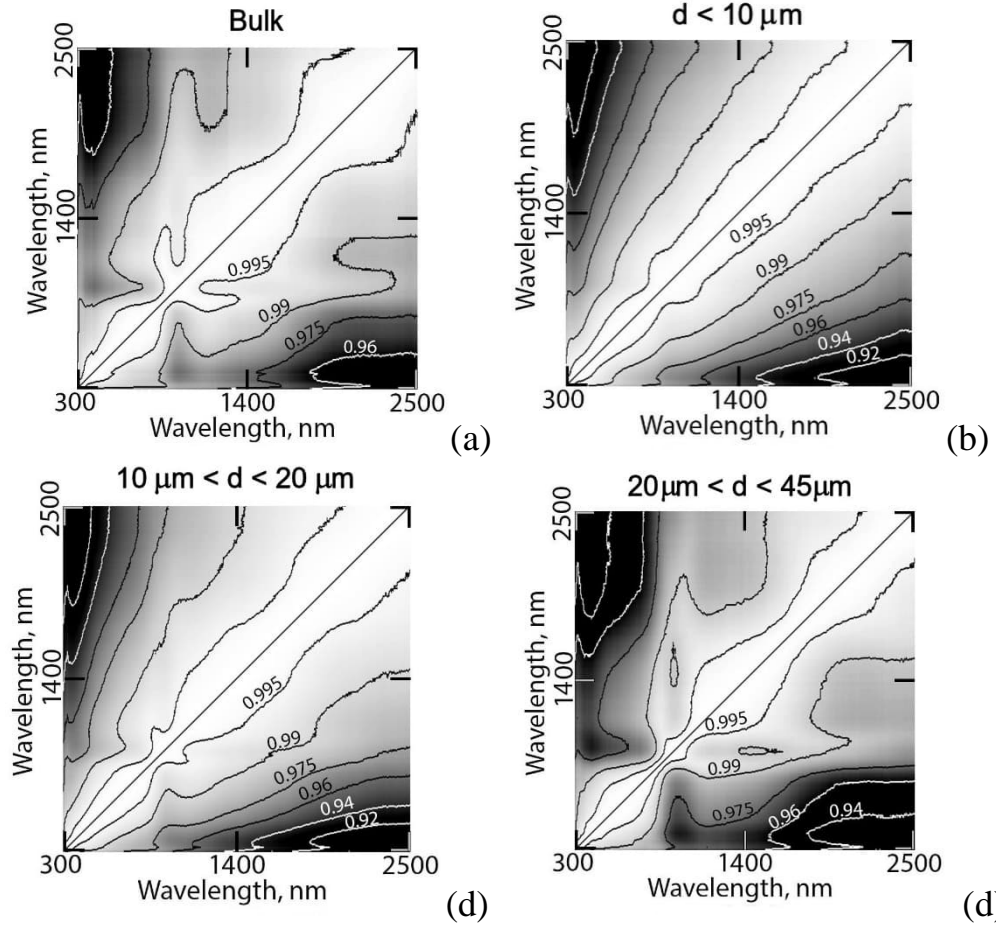


Figure 2.24. Correlation coefficient diagrams of LSCC lunar samples, the average spectra of which are shown in Fig. 1.23

<http://www.planetary.brown.edu/relabdocs/LSCCsoil.html>

Fig. 2.24 shows that the correlation coefficient diagrams of the sample suite do resemble those of the lunar measurements, especially, in the case of mare areas. The sample fraction  $d < 10 \mu\text{m}$  has almost no variability near the  $1 \mu\text{m}$  and  $2 \mu\text{m}$  bands, although this fraction should significantly influence the lunar spectra. The behavior of the bulk and coarse fraction  $20 \mu\text{m} < d < 45 \mu\text{m}$  on the diagrams is similar to that of the materials of the ejecta deposits and peculiar craters.

## 2.4 Conclusions

The main result of this study is the lunar imagery produced from the 1  $\mu\text{m}$  and 2  $\mu\text{m}$  bands using the Chandrayaan-1 M<sup>3</sup> data. This was made possible by processing the images using a Gaussian  $\lambda$ -convolution and Fourier filtration, which was carried out in the discrete form. This approach seems to be very prospective for further investigations using M<sup>3</sup> data, since it allows unprecedented image quality, allowing us to extract a variety of lunar surface characteristics. In particular, we have mapped different color ratios  $A(0.75 \mu\text{m})/A(0.54 \mu\text{m})$ ,  $A(0.95 \mu\text{m})/A(0.75 \mu\text{m})$ ,  $A(1.30 \mu\text{m})/A(0.75 \mu\text{m})$ ,  $A(2.6 \mu\text{m})/A(1.7 \mu\text{m})$ , positions of the minima ( $\lambda_{\text{min}}$ ) of the absorption bands and their depths. The band depth is determined using the convex hull technique that is rather universal and widespread in diagnostic spectroscopy.

We here studied an area comprising a portion of the Aristarchus Plateau, Montes Agricola, and a small part of the mare surface in Ocean Procellarum to the north of Montes Agricola. It was found, e.g., that the lava flows in the place between the Aristarchus Plateau and Montes Agricola have a chemical/mineral composition different in comparison with mare areas to the northwest of the ridge Montes Agricola. Differences in optical properties of the Aristarchus Plateau and Montes Agricola are found. In addition, we showed that the spectral properties of craters located on the plateau and mare surface are different. The cluster structure of the Adams (1974) correlation diagram  $\lambda_1 - \lambda_2$  allows an optical classification map of the region under study. In particular, we found a lunar cluster corresponding to glasses in the Adams diagram constructed using laboratory samples. This lunar cluster is formed by pyroclastic materials of the Aristarchus Plateau and Montes Agricola. The diagram allows us to establish relationships between geologic and spectral parameter maps.

Further studies can be developed with the application of the Gaussian  $\lambda$ -convolution and Fourier filtration to many other lunar areas. Correlation diagrams by Adams (1974) for pyroxene can be applied to numerous regions of the Moon.

## **2.5 References:**

- Adams, J.B., 1974. Visible and near-infrared diffuse reflectance spectra of pyroxenes as applied to remote sensing of solid objects in the solar system. *J. Geophys. Res.* 79, 4829–4836.
- Besse, S., Sunshine, J., Gaddis, L., 2014. Volcanic glass signatures in spectroscopic survey of newly proposed lunar pyroclastic deposits. *J. Geophys. Res.* 116(E6), doi: 10.1002/2013JE004537.
- Burns, R. 1993. *Mineralogical Applications of Crystal Field Theory*. Cambridge Univ. Press, Cambridge 459 p.
- Campbell, B.A., Carter, L.M., Hawke, B.R., Campbell, D.B., Ghent, R.R., 2008. Volcanic and impact deposits of the Moon's Aristarchus Plateau: A new view from Earth-based radar images. *Geology* 36 (2), 135–138.
- Chevrel, S.D., Pinet, P.C., Daydou, Y., Le Mouélic, S., Langevin, Y., Costard, F., Erard, S. 2009. The Aristarchus Plateau on the Moon: Mineralogical and structural study from integrated Clementine UV–Vis–NIR spectral data. *Icarus* 199, 9–24.
- Clark, R., 1983. Spectral properties of mixtures of montmorillonite and dark carbon grains: Implications for remote sensing minerals containing chemically and physically adsorbed water. *J. Geoph. Res.*, 88(B12), 10,635–10,644.
- Gaddis, L.R., Pieters, C.M., Hawke, B.R., 1985, Remote sensing of lunar pyroclastic deposits. *Icarus* 61, 461–89.

- Gaddis, L.R., Hawke, B.R., Robinson, M.S., Coombs, C., 2000. Compositional analyses of small lunar pyroclastic deposits using Clementine multispectral data. *J. Geophys. Res.* 105, 4245-4262.
- Gaddis, L.R., Staid, M.I., Tyburczy, J.A., Hawke, B.R., Petro, N.A., 2003. Compositional analyses of lunar pyroclastic deposits. *Icarus* 161, 262–280.
- Goswami, J. N. and Annadurai, M., 2009. Chandrayaan-1: India's first planetary science mission to the moon. *Current Sci.*, 96(4), 486-491.
- Graham, R.L., 1972. An efficient algorithm for determining the convex hull of a finite planar set. *Inform. Processing Lett.* 1, 132-133, doi:10.1016/0020-0190(72)90045-2.
- Hagerty, J.J., Lawrence, D.J., Hawke, B.R., Gaddis, L.R., 2009. Thorium abundances on the Aristarchus Plateau: Insights into the composition of the Aristarchus pyroclastic glass deposits. *J. Geophys. Res.* 114, E04002, doi:10.1029/2008JE003262.
- Hapke, B., 2012. *Theory of Reflectance and Emittance Spectroscopy*. Cambridge University Press, 455 p.
- Hawke, B.R., Coombs, C.R., Campbell, A., Lucey, P.G., Peterson, C.A., Zisk, S.H., 1991. Remote sensing of regional pyroclastic deposits on the north central portion of the lunar nearside. *Proc. Lunar Sci. Conf.* 21, 377–389.
- Hawke, B.R., Peterson, C.A., Coombs, C.R., Lucey, P.G., Smith, G.A., Taylor, G.J., 1995. Remote sensing studies of the Aristarchus region of the Moon. *Proc. Lunar Sci. Conf.* 26, 559–560.
- Head, J.W., 1974. Lunar dark mantle deposits: Possible clues to the distribution of early mare deposits. *Proc. Lunar Planetary Space Conf.* 5th 1, 207-222.
- Hiesinger, H., Jaumann, R., Neukum, G., Head, J.W., 2000. Ages of mare basalts on the lunar nearside. *J. Geophys. Res.* 105, 29239–29275.

- Hiesinger, H., Head, J.W., Wolf, U., Jaumann, R., Neukum, G., 2003. Ages and stratigraphy of mare basalts in Oceanus Procellarum, Mare Nubium, Mare Cognitum, and Mare Insularum. *J. Geophys. Res.* 108, 5065, doi:10.1029/2002JE001985.
- Hiesinger, H., Head, J., Wolf, U., Jaumann, R., Neukum, G., 2010. Ages and stratigraphy of lunar mare basalts in Mare Frigoris and other nearside maria based on crater size-frequency distribution measurements. *J. Geophys. Res.* 115, E03003 <http://dx.doi.org/10.1029/2009JE003380>.
- Horgan, B. H. N., Cloutis, E. A., Mann, P., Bell, J. F., 2014. Near-infrared spectra of ferrous mineral mixtures and methods for their identification in planetary surface spectra. *Icarus* 234, 132–154. <https://doi.org/10.1016/j.icarus.2014.02.031>
- Kaydash, V., Shkuratov, Y., Videen, G. Phase-ratio imagery as a tool of lunar remote sensing. *Journ. Quant. Spectrosc. Rad. Transfer* 2012. 113(18), 2601-2607.
- Kaydash, V., Shkuratov, Y., Videen, G., 2014. Dark halos and rays of young lunar craters: A new insight into interpretation. *Icarus* 231, 22-33.
- Kaydash, V., Surkov, Ye., Shkuratov, Yu., Videen, G. Mapping parameters of the lunar 1-micron spectral band with improved Chandrayaan-1 M<sup>3</sup> data. *Lunar Planet. Sci.*, 49-th, LPI Houston, 2018, Abstract #1649.
- Klima, R. L., Pieters, C. M., Dyar, M. D., 2007. Spectroscopy of synthetic Mg-Fe pyroxenes I: Spin-allowed and spin-forbidden crystal field bands in the visible and near-infrared, *Meteor. Planet. Sci.*, 42, 235-253
- Klima, R. L., Dyar, M. D. Pieters, C. M., 2011. Near-infrared spectra of clinopyroxenes: Effects of calcium content and crystal structure, *Meteor. Planet. Sci.*, 46, 379-395, doi: 10.1111/j.1945-5100.2010.01158.x.

- Kneissl, T., van Gasselt, S., Neukum, G., 2011. Map projection independent crater size-frequency determination in GIS environments – new software tool for ArcGIS. *Planet. Space Sci.* 59, 1243–1254.
- Korokhin, V.V., Velikodsky, Yu.I., Shkuratov, Yu.G., Kaydash, V.G., Gerasimenko, S.Y., Opanasenko, N.V., Gorden Videen, Carle Pieters, 2010. Removal of topographic effects from lunar images using Kaguya (LALT) and Earth-based observations. *Planet. Space Sci.* 58, 1298-1306 (doi:10.1016/j.pss.2010.05.013).
- Korokhin, V.V., Velikodsky, Yu.I., Shalygin, E.V., Shkuratov, Yu.G., Kaydash, V.G., Gorden, V., 2014. Retrieving lunar topography from multispectral LROC images. *Planet. Space Sci.* 92, 65–76, <http://dx.doi.org/10.1016/j.pss.2014.01.008>.
- Korokhin, V., Shkuratov, Y., Kaydash, V., Basilevsky, A., Rohachova, L., Velikodsky, Y., Opanasenko, N., Videen, G., Stankevich, D., Kaluhina, O., 2016a. Characterization of a photometric anomaly in lunar Mare Nubium. *Planet. Space Sci.* 122, 70–87. doi:10.1016/j. Pss.2016.01.011.
- Korokhin, V.V., Shkuratov, Y.G., Kaydash, V.G., Velikodsky, Yu.I., Videen, G., 2016b. A new phase function of the lunar surface deduced from LROC WAC photometric measurements. *Lunar Planet. Sci.*, 47-th, LPI Houston, Abstract #1248.
- Korokhin, V., Velikodsky, Y., Shkuratov, Y., Kaydash, V., Mall, U., Videen, G., 2018. Using LROC WAC data for lunar surface photoclinometry. *Planet. Space Sci.* <https://doi.org/10.1016/j.pss.2018.05.020>.
- Lucey, P.G., Hawke, B.R., Pieters, C.M., Head, J.W., McCord, T.B., 1986. A compositional study of the Aristarchus region of the Moon using nearinfrared reflectance spectroscopy: *J. Geophys. Res.* 91, D344-D354.

- Lucey, P.G., Taylor, G.I., Malaret, E., 1995. Abundance and distribution of iron on the Moon. *Science* 268, 1150–1153.
- Lucey, P.G., Blewett, D.T., Joliff, B.D., 2000. Lunar iron and titanium abundance algorithms based on final processing of Clementine UV-visible images: *J. Geophys. Res.* 105, 20,297–20,306, doi: 10.1029/1999JE001117.
- Martinot, M., Besse, S., Flahaut, J., Quantin-Nataf, C., Lozac'h, L., van Westrenen, W., 2018. Mineralogical diversity and geology of Humboldt crater derived using Moon Mineralogy Mapper data. *J. Geophys. Res.* 612–629, doi: 10.1002/2017JE005435.
- McCord, T.B., Adams, J.B., 1973. Progress in remote optical analysis of lunar surface composition. *The Moon* 7, 453–474.
- McCord, T.B., Charette, M.P., Johnson, T.V., Lebofsky, L.A., Pieters, C.M., Adams, J.B., 1972. Lunar spectral types. *J. Geophys. Res.* 77, 1349–1359.
- McEwen, A.S., Robinson, M.S., Eliason, E.M., Lucey, P.G., Duxbury, T.C., and Spudis, P.D., 1994. Clementine observations of the Aristarchus region of the Moon: *Science* 266, 1858–1862, doi: 10.1126/science.266.5192.1858.
- Michael, G., Neukum, G., 2010. Planetary surface dating from crater size-frequency distribution measurements: partial resurfacing events and statistical age uncertainty. *Earth Planet. Sci. Lett.* 294, 23–229.
- Myrick, M.L., Simcock, M.N., Baranowski, M., Brooke, H., Morgan, S.L., McCutcheon, J., 2011. The Kubelka-Munk diffuse reflectance formula revisited. *Applied Spectrosc. Rev.* 46 (2), 140–165.
- Nelder, J., Mead, R., 1965. A simplex method for function minimization. *Computer J.*, 7, 308–313.
- Neukum, G., Ivanov, B., Hartmann, W., 2001. Cratering records in the inner solar system in relation to the lunar reference system. *Space Sci. Rev.*, 96, 55–86.

- Ohtake, M., Pieters, C.M., Isaacson, P., Besse, S., Yokota, Y., Matsunaga, T., Boardman, J., Yamamoto, S. Haruyama, J., Staid, M., Mall, U., Green, R.O., 2013. One Moon, many measurements 3: Spectral reflectance. *Icarus* 226, 364-374.
- Pieters, C.M., 1993. Compositional diversity and stratigraphy of the lunar crust derived from reflectance spectroscopy. In: Pieters, C.M., Englert, P.A.J. (Eds.), *Remote Geochemical Analysis: Elemental and Mineralogical Composition*. Cambridge Univ. Press, Cambridge, pp. 309–339.
- Pieters, C., Hiroi, T., 2004. RELAB (Reflectance experiment laboratory): A NASA multispectral spectroscopy facility. *Lunar Planet. Sci.* 35. Abstract 1720.
- Pieters, C.M., Taylor, L.A., Noble, S.K., Keller, L.P., Hapke, B., Morris, R.V., Allen, C.C., McKay, D.S., Wentworth, S.J., 2000. Space weathering on airless bodies: Resolving a mystery with lunar samples. *Meteor. Planet. Sci.* 35, 1101–1107.
- Pieters, C.M., Stankevich, D.G., Shkuratov, Y.G., Taylor, L.A., 2002. Statistical analysis of the links between lunar mare soil mineralogy, chemistry and reflectance spectra. *Icarus* 155, 285–298.
- Pieters, C.M., Shkuratov, Y.G., Kaydash, V.G., Stankevich, D.G., Taylor, L., 2006. Lunar soil characterization consortium analyses: pyroxene and maturity estimates derived from Clementine image data. *Icarus* 184, 83-101.
- Pieters, C.M., 19 colleagues, 2009. The Moon Mineralogy Mapper (M3) on Chandrayaan-1. *Science* 326, 568–572.
- Robinson, M.S., Brylow, S.M., Tschimmel, M., et al., 2010. Lunar Reconnaissance Orbiter (LROC) Instrument Overview, *Space Sci. Rev.* 150, 81-124.
- Schultz, P.H., 1976. *Moon Morphology*. Univ. of Texas Press, Austin.



- Shkuratov, Y., Starukhina, L., Kreslavsky, M., Opanasenko, N., Stankevich, D., Shevchenko, V., 1994. Principle of perturbation invariance in photometry of atmosphereless celestial bodies. *Icarus* 109, 168–190.
- Shkuratov, Y.G., Kaydash, V.G., Opanasenko, N.V., 1999a. Iron and titanium abundance and maturity degree distribution on lunar nearside. *Icarus* 137(2), 222-234.
- Shkuratov, Y., Starukhina, L., Hoffmann, H., Arnold, G., 1999b. A model of spectral albedo of particulate surfaces: implication to optical properties of the Moon. *Icarus* 137(2), 235-246.
- Shkuratov, Yu., Stankevich, D., Kaydash, V., Omelchenko, V., Pieters, C., Pinet, C., Chevrel, S., Daydou, Y., Foing, B., Sodnik, Z., Josset, J.-L., Taylor, L., Shevchenko, V., 2003a. Composition of the lunar surface as will be seen from SMART-1: A simulation using Clementine data. *J. Geophys. Res.* 108(E4), doi:10.1029/2002JE001971.
- Shkuratov Y., Kaydash V., Pieters C., 2005. Lunar clinopyroxene and plagioclase: surface distribution and composition. *Solar Syst. Res.* 39(4), 255-266.
- Shkuratov, Y., Kaydash, V., Starukhina, L., Pieters, C., 2007. Lunar surface agglutinates: mapping composition anomalies. *Solar System Res.* 41, 177-185.
- Shkuratov, Y., Kaydash, V., Korokhin, V., Velokodsky, Y., Opanasenko, N., Videen, G., 2011. Optical measurements of the Moon as a tool to study its surface. *Planet. Space Sci.* 59, 1326-1371. doi:10.1016/j.pss.2011.06.011.
- Shkuratov, Y., Kaydash, V., Videen, G., 2012. The crater Giordano Bruno as seen with optical roughness imagery. *Icarus* 218 (1), 525-533.
- Shkuratov, Y., Kaydash, V., Rohacheva, L., Korokhin, V., Ivanov, M., Velikodsky, Y., Videen, G. Comparison of lunar red spots including the

- crater Copernicus. *Icarus* 2016, 272, 125–139.  
doi:10.1016/j.icarus.2016.02.034
- Shkuratov Y., Korokhin V., Shevchenko V., Mikhalechenko O., Belskaya I., Kaydash V., Videen G., Zubko E., Velikodsky Y., 2018a. A photometric function of planetary surfaces for gurmets. *Icarus* 302, 213-236.
- Shkuratov, Y., Basilevsky, A., Kaydash, V., Ivanov, B., Korokhin, V., Videen, G., 2018b. Surface erosion and sedimentation caused by ejecta from crater Tycho. *Planet. Space Sci.* 151, 130-140.
- Smith, J.O., 2002. *Mathematics of the Discrete Fourier Transform (DFT)*. CCRMA, Stanford University, Stanford, California, 237 p.
- Stadermann, A.C., Zanetti, M.R., Jolliff, B.L., Hiesinger, H., van der Bogert, C.H., Hamilton, C.W., 2018. The age of lunar mare basalts south of the Aristarchus Plateau and effects of secondary craters formed by the Aristarchus event. *Icarus* 309, 45-60.
- Sunshine, J.M., Pieters, C.M., Pratt, S.F., 1990. Deconvolution of mineral absorption bands: an improved approach. *J. Geophys. Res.* 95, 6955–6966.
- Sunshine, J., Pieters, C., 1993. Estimating model abundances from the spectra of natural and laboratory pyroxene mixtures using the Modified Gaussian Model. *J. Geophys. Res.* 98, 9075–9087.
- Taylor, L.A., Pieters, C.M., Morris, R.V., Keller, L.P., McKay, D.S., Parchen, A., Wentworth, S.J., 1999. Integration of the chemical and mineralogical characteristics of lunar soils with reflectance spectroscopy. *Lunar Planet. Sci. Conf. 30th*, Abstract no. 1859, LPI, Houston, USA.
- Taylor, L.A., Pieters, C.M., Morris, R.V., Keller, L.P., McKay, D.S., 2001. Lunar mare soils: space weathering and the major effects of surface correlated nanophase Fe. *J. Geophys. Res.* 106, 27,985–28,000.

- Velikodsky, Y.I., Korokhin, V.V., Shkuratov, Y.G., Kaydash, V.G., Videen, G., 2016. Opposition effect of the Moon from LROC WAC data. *Icarus* 275, 1-15.
- Wagner, R., Head, J.W., Wolf, U., Neukum, G., 2002. Stratigraphic sequence and ages of volcanic units in the Gruithuisen region of the Moon. *J. Geophys. Res.* 107 <http://dx.doi.org/10.1029/2002JE001844>.
- Weitz, C., Head, J., Pieters, C., 1998. Lunar regional dark mantle deposits: Geologic, multispectral, and modeling studies: *J. Geophys. Res.* 103, 22,725-22,759, doi: 10.1029/98JE02027.
- Wood, R.W., 1910. Moon in yellow and ultraviolet light. *Mon. Not. Roy. Astron. Soc.*, 70, 226.
- Wood, R.W., 1912. Selective absorption of light on the Moon's surface and lunar petrography. *Astrophys. J.*, 36, 75.
- Wilhelms, D.E., 1987. The geologic history of the Moon: U.S. Geological Survey Professional Paper 1348, 342 p.
- Wilhelms, D.E., McCauley, J.F., 1971. Geologic map of the near side of the Moon. US Geological Survey Map I-703.
- Whitten, J., Head, J., 2015. Lunar cryptomaria: Mineralogy and composition of ancient volcanic deposits. *Planet. Space Sci.* 106. 67–81.
- Fu, Z., Robles-Kelly, A., Caelli, T., Tan, R.T., 2007. On automatic absorption detection for imaging spectroscopy: a comparative study. *IEEE Transac. Geosci. Remote Sensing* 45(11), 3827–3844.
- Zisk, S.H., Hodges, C.A., Moore, H.J., Shorthill, R.W., Thompson, T.W., Whitaker, E.A., Wilhelms, D.E., 1977. The Aristarchus-Harbinger region of the Moon: Surface geology and history from recent remote-sensing observations. *The Moon* 17, 59-99.

### **CHAPTER 3. [PAPER] CHARACTERIZING PYROCLASTIC DEPOSITES OF LUNAR MARE VAPORUM WITH IMPROVED CHANDRAYAAN-1 M3 DATA**

We investigate a southern portion of Mare Vaporum using improved Chandrayaan-1 M<sup>3</sup> images. The application of additional data processing allows us to analyze such spectral parameters as the depths and positions of the absorption bands near 1 and 2  $\mu\text{m}$ . Three main mineral types that cover the region were detected. These mineral types were mapped using the cluster analysis of Adam's diagram for pyroxenes. We focus on two areas of pyroclastic deposits: a large one at the northern border of Mare Vaporum and a small area around the crater Hyginus placed at the south border. Irregular mare patches in the crater Hyginus reveal the 2  $\mu\text{m}$  band shifted to longer wavelengths. The mapping of the Adam's diagram classes was inspected with phase-ratio analysis of LROC NAC data: the areas associated with clinopyroxenes are distinguished both in albedo and phase-ratio images, having higher roughness than surrounding surface; in contrast to this the areas associated with pyroclastic glasses does not seen neither in albedo nor phase-ratio images. A possible mechanism of the irregular mare patches formations is proposed.

### 3.1 Introduction

Spectrophotometry of planetary surfaces in UV, visible, and NIR is a power tool to study their chemical and mineralogical compositions. The Moon Mineralogy Mapper ( $M^3$ ) is the scanning spectrometer onboard the Chandrayaan-1 spacecraft of ISRO (Goswami and Annadurai, 2009). Its main purpose was remote sensing of the lunar surface mineralogy with the high resolution (e.g., Pieters et al., 2009). This device had covered over 95% of the lunar surface using the hyperspectral images with spatial resolution of about 140 m/pixel. The  $M^3$  spectrometer measured the lunar surface in the range between 540 and 3000 nm in 85 spectral bins. This spectrometer has high potential to detect mineral absorption bands of the most abundant lunar minerals including clino-, orthopyroxenes, olivines, spinels, and ilmenite (e.g., Klima et al., 2011; Isaacson et al., 2011a,b; Pieters et al., 2014; Donaldson-Hanna et al., 2014; Surkov et al., 2020). For different minerals the origin of the bands may be different in the mentioned spectral range. For instance, pyroxenes and olivines reveal absorption bands caused by the interactions of  $Fe^{2+}$  ions with the crystal field: pyroxenes have two prominent absorption features near 1 and 2  $\mu m$ , and olivine has three strongly overlapped bands about 0.9, 1.0, and 1.2  $\mu m$  (Burns, 1993). In contrast the ilmenite ( $FeTiO_3$ ) spectral feature at 1.5  $\mu m$  is formed by the intervalence charge transfer  $Fe^{2+} \rightarrow Ti^{4+}$  (Burns, 1993).

The band position of various types of pyroxenes depends on their composition (e.g. Adams, 1974; Cloutis and Gaffey, 1991; Burns, 1993). For example, the band centers move to longer wavelengths when calcium ions are replaced by magnesium ions (Hazen et al. 1978; Besse et al. 2014). The presence of volcanic glasses in the lunar soil may manifest themselves as broadening and flattening of absorption bands, due to their amorphous structure (Bell et al., 1976).

However, for the band near 1  $\mu\text{m}$ , such broadening and flattening may not be due to the presence of glass, but to the presence of a mixture of pyroxenes with olivines (Singer, 1981). A more distinctive spectral sign of the presence of volcanic glass is simultaneous shifts of the 1  $\mu\text{m}$  band to longer wavelengths and the 2  $\mu\text{m}$  band to shorter wavelengths (e.g. Adams, 1974).

The presence of volcanic glass is closely associated with the areas of lunar pyroclastic deposits (LPD), which are low-albedo features widely distributed on the Moon and often related to volcanic vents linked with fractures, irregular depressions, and non-circular craters. They have been mapped (e.g., Wilhelms, 1987, Wilhelms and McCauley, 1971; Gaddis et al., 2003) and studied with different remote sensing techniques. Among them are telescopic optical surveys (e.g., Hawke and Coombs, 1987, Coombs and Hawke, 1992), spacecraft remote sensing with Clementine UVVIS camera (Gaddis et al., 2000; 2003), high-resolution Lunar Reconnaissance Orbiter Camera (LRO WAC) survey (Gustafson et al., 2012), and radar observations (Carter et al, 2009; Cambell et al., 2009). The M<sup>3</sup> data have been used also for studies of the LPD, e.g., to quantify water abundance (Milliken and Li, 2017; Li and Milliken, 2016).

To determine chemical characteristics of the lunar surface features, e.g. such as the LPD, ratios of albedo  $A(\lambda)$  at different wavelengths called color ratios are usually used, e.g.,  $C(750\text{ nm}/950\text{ nm})$  or  $C(450\text{ nm}/550\text{ nm})$ . Using Clementine's data, Lucey et al. (1995, 2000a,b) developed a successful technique to assess remotely the abundance of FeO, TiO<sub>2</sub>, and the optical maturity (OMAT) that is closely correlated with the agglutinate content and maturity degree of the lunar regolith (Pieters et al., 2006): the higher the OMAT, the lower the maturity degree. The approach proposed by Lucey et al. (1995, 2000a,b) has been improved by Ohtake et al. (2010, 2012).

Color ratios also allow one to make conclusions about parameters of absorption bands of different minerals. For example, the 1  $\mu\text{m}$  band of pyroxenes and olivines can be roughly characterized by  $C(950\text{nm}/750\text{nm})$ . However, this characterization is not enough for a reliable mineralogical description because it does not provide precise information about the band position and its shape that are necessary. The spectrometer  $M^3$  provides an opportunity for accurate analyses of such spectral parameters, since the number of spectral bins is rather high (Mustard et al., 2011; Whitten et al., 2011). Unfortunately, the  $M^3$  capabilities are limited, since the images are burdened by a random structure of narrow strips. We have developed a technique to suppress the strip structure (Shkuratov et al., 2019; Surkov et al., 2020). This allows us, particularly, to provide a mineralogical description of the northwestern part of Aristarchus Plateau with Adam's diagram (Shkuratov et al., 2019). The abundance maps of glass and pyroxenes of different types were obtained. Later we mapped the depth of the 1.5  $\mu\text{m}$  absorption band near the crater Dawes, which is well correlated with the  $\text{TiO}_2$  abundance (Surkov et al., 2020). We interpreted this spectral feature as the absorption band of ilmenite observed in laboratory measurements (Isaacson et al., 2011a).

We here investigate the spectral properties of a southern portion of Mare Vaporum and adjacent area of the rima and crater Hyginus (coordinates  $7.8^\circ\text{N}$ ,  $6.3^\circ\text{E}$ , diameter 11 km, depth 0.8 km) that are shown in Fig. 2. A portion of the  $M^3$  hyperspectral image M3G20090608T042049\_V01\_RFL.IMG from [pds-imaging.jpl.nasa.gov/volumes/m3.html](https://pds-imaging.jpl.nasa.gov/volumes/m3.html) has been used. This region has complicated geology and, hence, expectedly diverse mineralogically. It was previously included in the list of LPD and its composition was analyzed using the 5-band Clementine UVVIS data at a resolution of 100 m/pixel (Gaddis et al., 2003). Hawke and Coombs (1987) pointed out that the spectral characteristics of the Rima Hyginus region are consistent with dark mantle deposits of pyroclastic origin. Wilson et al.

(2011) also have mapped small dark patches near the crater Hyginus as LPD and considered it as a volcanic caldera initiated by the intrusion of a dike that did not breach the surface. We consider here another approach to detection of pyroclastic material and mineral diversity of the scene using the correlation diagram by Adams (1974) as has been carried out by Shkuratov et al. (2019). We perform a cluster analysis of the diagram that represents the correlation between the positions of the 1  $\mu\text{m}$  and 2  $\mu\text{m}$  absorption bands. Clusters on this diagram can be related with certain type of pyroxenes and other minerals (McCord and Adams, 1973; Adams, 1974).

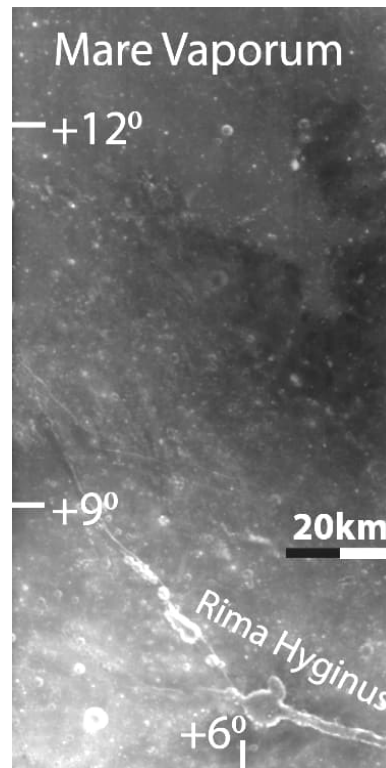


Figure 3.1 A southern portion of Mare Vaporum and adjacent area. The image is a fragment of M3G20090608T042049\_V01\_RFL.IMG at 750 nm spectral band.



Other attractive features of this region are the irregular mare patches (IMPs) in the crater Hyginus. IMPs are small (about 500 m wide) formations with sharp borders. Since their discovery by Whitaker (1972) during the Apollo-15 mission, they have been widely investigated in detail (Strain and El-Baz, 1980; Schultz et al., 2006; Robinson et al., 2010; 2012; Yamamoto et al., 2013; Carter et al., 2013). Nevertheless, their origin is still unclear. Some considered them as volcanic calderas; at least in regard to Ina (e.g., Strain and El-Baz, 1980). Another opinion is that they may be caused by the release of volatiles, lava flow inflation, or pyroclastic eruption. These hypotheses all suggest they are evidence of young lunar volcanism (Stooke, 2012; Elder et al., 2017). The sharpness of the borders of these formations hints that they are young features. This is supported by crater counting (Braden et al., 2014). On the other hand, the absolute age of IMPs is a subject of discussion according to the volcanological model of Qiao et al. (2019) who treat IMPs as not very young features with unique substrate characteristics preventing a correct interpretation of crater size-frequency calculations for superposed impact craters. Note that such structures also were found on Mercury (Blewett et al., 2013). To study the lunar formations, different techniques have been used, including radar observations (Carter et al., 2013). Unfortunately, applications of the spectral techniques almost are not possible, since the formations are too small and available  $M^3$  spectral data can hardly be used for reliable geological conclusions. The exception is Ina, or D-caldera, with a size of about 2 km that is only 4-5 times larger than the spatial resolution of  $M^3$  (Staid et al., 2011; Glaspie et al., 2019; Grice et al., 2016). We believe that our additional data processing allows one to improve the spectral data for formations that are several  $M^3$  pixels in size, providing information about these peculiar objects.

### 3.2 M<sup>3</sup> data and processing

A big problem for performing a quantitative analysis of M<sup>3</sup> images is the presence of noise that manifests itself as a pattern of narrow strips. An example of such a pattern is shown in Fig. 3.3a that presents a fragment of M3G20090608T042049\_V01\_RFL.IMG restricted by the frame seen in Fig. 3.1. To weaken the stripped noise pattern, we use the following two steps of M<sup>3</sup> data processing, whose detailed description is provided by Shkuratov et al. (2019) and Surkov et al. (2020); here we outline them in brief. The M<sup>3</sup> data can conveniently be represented as a 3-D array of numbers  $m \times n \times b$ , where  $m \times n$  is the frame size and  $b$  is the number of spectral channels in the range 540–3000 nm. The first step we use is a  $\lambda$ -spectrum processing consisting in the spectral convolution with a Gaussian core. The core width is chosen empirically; the criterium is that the ratio of the spectrally smoothed and initial data should be integrally less than 0.2%.

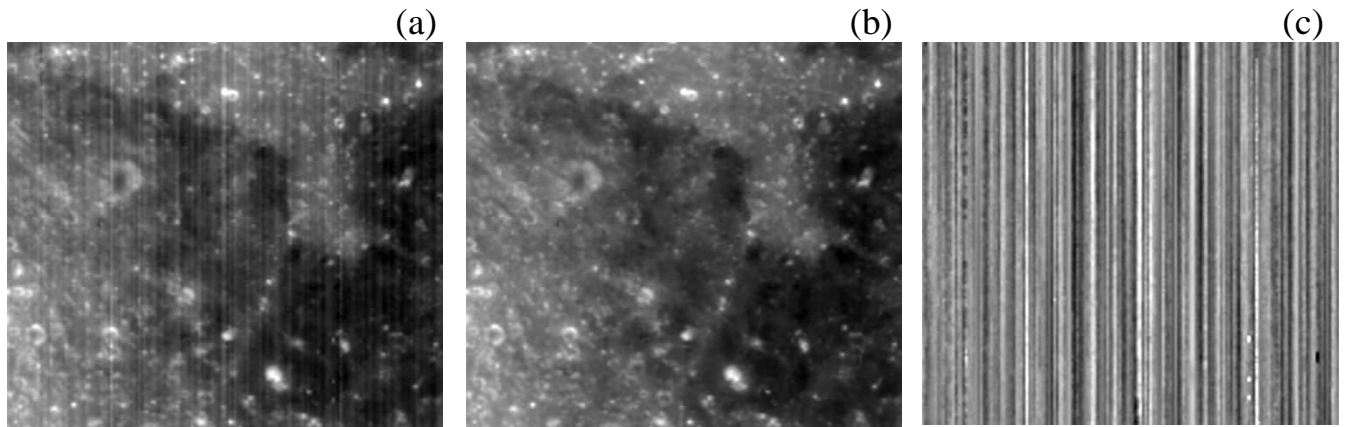


Figure 3.2 The images (a) and (b) correspond to the cases before and after the proposed processing of the portion of M<sup>3</sup> hyperspectral image of the border of Mare Vaporum at 750nm. The image (c) represents the ratio (a)/(b).

Usually, this correction is not enough for mapping various parameters, e.g., color ratios or the band depth and position. For further attenuation of the noise strips, we use Fourier filtering of images in each spectral channel. As a result of the

two-dimensional discrete Fourier transform of the image  $f_{i,j}$  in a certain spectral channel, we obtain the spatial frequency spectrum  $F_{p,q}$  (Eq. 3.1).

$$F_{p,q} = \sum_{j=0}^{m-1} \sum_{k=0}^{n-1} \exp(i(\omega_p j + \omega_q k)) f_{j,k}, \text{ where } \omega_p = -\frac{2\pi p}{m}, \omega_q = -\frac{2\pi q}{n}, \quad (3.1)$$

where  $F_{p,q}$  is a matrix of complex numbers of size  $m \times n$ ; the same as the original image has. The second processing step is the suppression of the strip noise localized in the frequency plane (Shkuratov et al., 2019; Surkov et al., 2020):

$$\tilde{f}_{j,k} = \frac{1}{mn} \sum_{p=0}^{m-1} \sum_{q=0}^{n-1} \exp(-i(\omega_p j + \omega_q k)) \Lambda(\omega_p, \omega_q, \Omega, \sigma_1, \sigma_2) F_{p,q}, \quad (3.2)$$

and

$$\Lambda(\omega_p, \omega_q, \Omega, \sigma_1, \sigma_2) = \begin{cases} \exp\left(-\left(\frac{\omega_p^2}{2\sigma_1} + \frac{\omega_q^2}{2\sigma_2}\right)\right) & \text{if } (\omega_p, \omega_q) \in \Omega, \\ 1, & \text{otherwise} \end{cases}, \quad (3.3)$$

where  $\Omega$  is the area of frequency localization of the strip noise;  $\sigma_1$  and  $\sigma_2$  are the parameters of the Gaussian filtration. Then we produce the inverse Fourier transform to obtain a filtered image of the lunar surface. Figure 3.2b shows such an image produced at  $\sigma_1 \approx 15$  and  $\sigma_2 \gg \sigma_1$ . No signs of a strip pattern can be observed on the image. The ratio of images before and after the  $\lambda$ -convolution and Fourier spectrum filtration is depicted in Fig. 3.2c. The ratio does not carry any information about the Moon that indicates the preservation of the useful signal after processing.

The resulting spectral images allow estimations of the absorption band parameters from reflectance spectra. There are a number of methods to make them. For instance, reflectance spectra can be represented as a combination of the isolated bands, whose profiles are described using functions, e.g., Gaussians, with free parameters (e.g., Sunshine et al., 1990; Sunshine and Pieters, 1993). This gives possibilities to associate each term in the set of used functions with absorption

bands of specific components in the physical mixture. This advantage, however, is debatable because the reflectance spectrum of a mineral mixture is not a strict linear combination of the spectra of the initial components. It may be that some terms do not correspond to the physical component presented in a mixture at all. There are approaches that use the continuum removal for easier depiction of absorption features in a spectrum. The simplest approximation of the continuum is the linear function. A more sophisticated method is to use the separate linear functions for each band in the spectrum. The main problem of this technique is the uncertainty in the determination of the band edges, especially, when the bands are overlapped. To remove the spectral continuum, we here divide the spectrum in each image pixel by its segmented upper hull (e.g., Clark et al., 1987).

### **3.3 Results and discussion**

We outline two LPD regions, which were previously identified by Weitz et al. (1998), on the portion of the M<sup>3</sup> hyperspectral image of Fig. 3.3a, which was processed with the described two-step filtration technique. The white contours mark the border of the dark albedo area, which was indicated as dark mantle deposits of pyroclastic origin (Hawke and Coombs, 1987; Weitz et al., 1998; Gaddis et al., 2000). We note that in a number of works these deposits have been investigated using various methods (e.g., optical, radar, color), nevertheless their exact shapes vary for different techniques as well as the distribution of volcanic glasses over them. For example, radar contours of low circular polarization ratio (CPR) (Carter et al., 2009) do not exactly coincide with ones constructed using the spectral slope in the UV-VIS by Clementine data (Weitz et al., 1998). The same difference in LPD shapes is observed for the Hyginus crater area (white contours at the low edge of Fig. 3.3a) compared with radar data (Carter et al., 2009) and

optical, chemical and maturity data acquired from Clementine (Wilson et al., 2011). We develop another spectral indicator of LPD in the VIS-NIR range, which is more sensitive to the presence of volcanic glasses and may be mapped with spectral and spatial resolution of  $M^3$  data. This method is to map shifts of the 1  $\mu\text{m}$  band position to longer wavelengths as an indicator of the presence of volcanic glasses in the material of the LPD.

### **3.3.1. Mapping the band parameters**

We map some spectral parameters retrieved from the  $M^3$  spectra in Fig. 3.3b-f. These include (b) the color ratio  $A(950\text{nm})/A(750\text{nm})$ , (c) the position of the 1  $\mu\text{m}$  band, (d) the position of the 2  $\mu\text{m}$  band, (e) the depth of the band at 1  $\mu\text{m}$ , and (f) the depth of the band at 2  $\mu\text{m}$ . The color ratio  $C(950\text{ nm}/750\text{ nm})$  in Fig. 3.33b reveals young craters, fresh slopes of Rima Hyginus, and two types of mare materials. The material of the southern portion has significantly higher values of color ratio than that for the basalt to the north. In the previous optical and radar studies (Carter et al, 2009, Wilson et al., 2011), the Mare Vaporum LPDs almost do not reveal themselves in this color ratio. The maps of the depth and position of the 1  $\mu\text{m}$  band (Fig. 3.3c,e) appear different from the albedo and color ratio distributions. The same for the 2  $\mu\text{m}$  band is shown in Fig. 3.3d,f. As one can see, both bands are much deeper for the lunar surface with immature regolith. The border of Mare Vaporum is not seen at all.

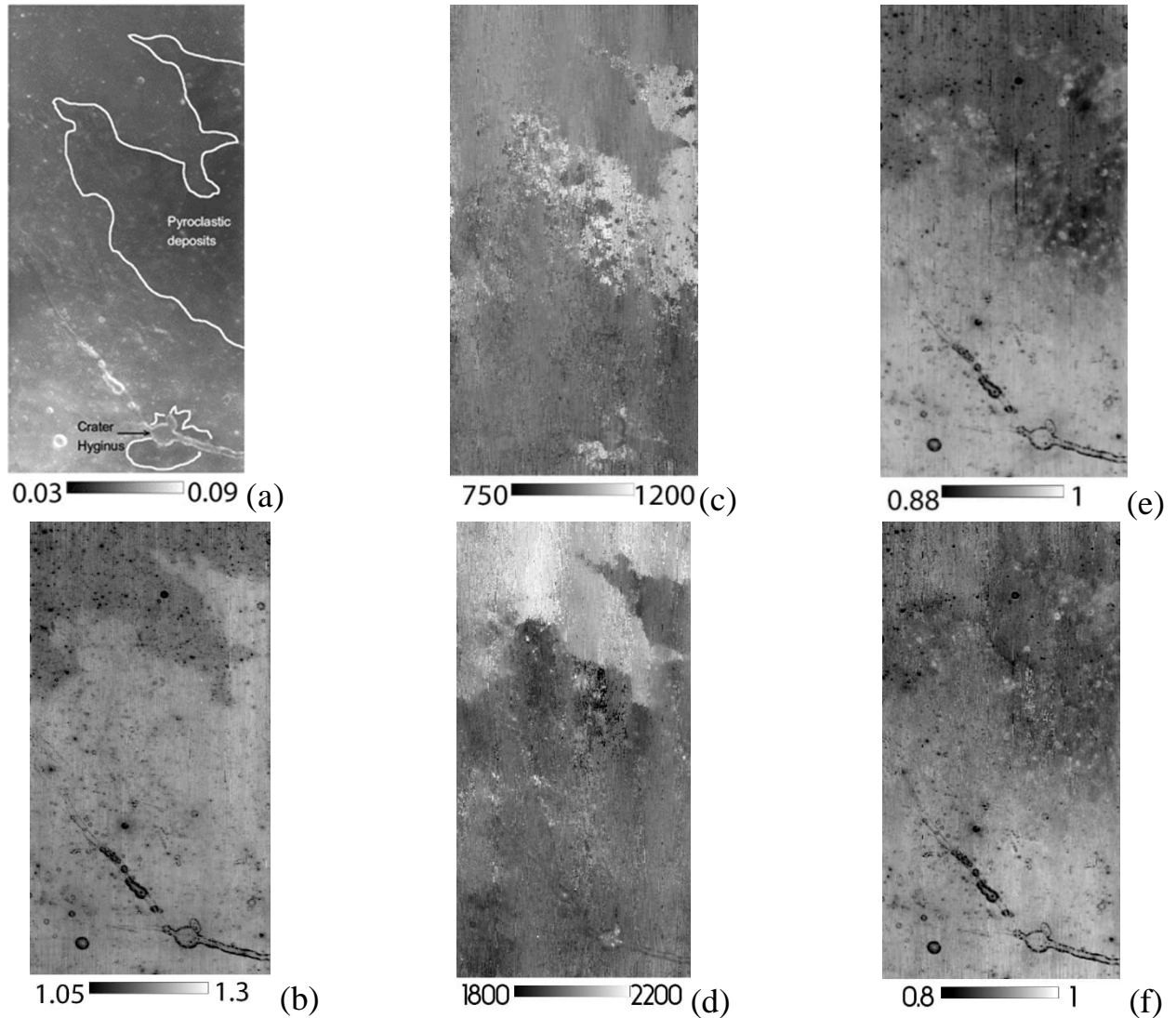


Figure 3.3 Distributions of optical parameters of the scene under study. (a) albedo at 750 nm  $A(750 \text{ nm})$ ; (b) color ratio  $A(950 \text{ nm})/A(750 \text{ nm})$ ; (c) the position of the  $1 \mu\text{m}$  band in nm; (d) the position of the  $2 \mu\text{m}$  band in nm; (e) the depth of the band at  $1 \mu\text{m}$ ; and (f) the depth of the band at  $2 \mu\text{m}$ . The band depth is represented in the following manner: the deeper the band in the spectrum, the darker the tone on the map.

Some of the outlined LPDs are characterized by the deepening of the  $1 \mu\text{m}$  band depth. The image of this parameter reveals many features that are absent in the color ratio distribution. The cause of dark spots on this map is the deep band at  $1 \mu\text{m}$  with the center shifted to approximately 1075 nm or even longer (Fig. 3.3e), the spectral feature intrinsic to volcanic orange glasses Weits et al. (1998). The

bright ones are craters that impacted the lunar surface after glass deposits had been formed. These are also seen in the depth map of the 2  $\mu\text{m}$  band (Fig. 3.3f). These craters have the same centers of the 1 and 2  $\mu\text{m}$  bands as the adjacent mare surface with higher spectral slope.

The exact positions of the bands are the most informative parameter in the qualitative determination of mineralogical composition. Using a correlation diagram of the bands positions has been proposed by Adams (1974) to separate lunar ortho- and clinopyroxenes. The correlation diagram calculated with  $M^3$  data of the scene is shown on Fig. 3.4a. The diagram allows us to distinguish three main classes shown in Fig. 3.34a. Further the class map (Fig. 3.4c) is produced. We classify each pixel of the  $M^3$  hyperspectral image calculating the distance between the band depth positions in each pixel and the centers of each class; then, we attribute the pixel to that class, the distance to which was minimal. The class centers are chosen at the maximal density of the distribution. Coordinates of the centers of the classes 1, 2, and 3 were determined as (2055 nm, 960 nm), (2175 nm, 990 nm), and (2065 nm, 1080 nm), respectively.

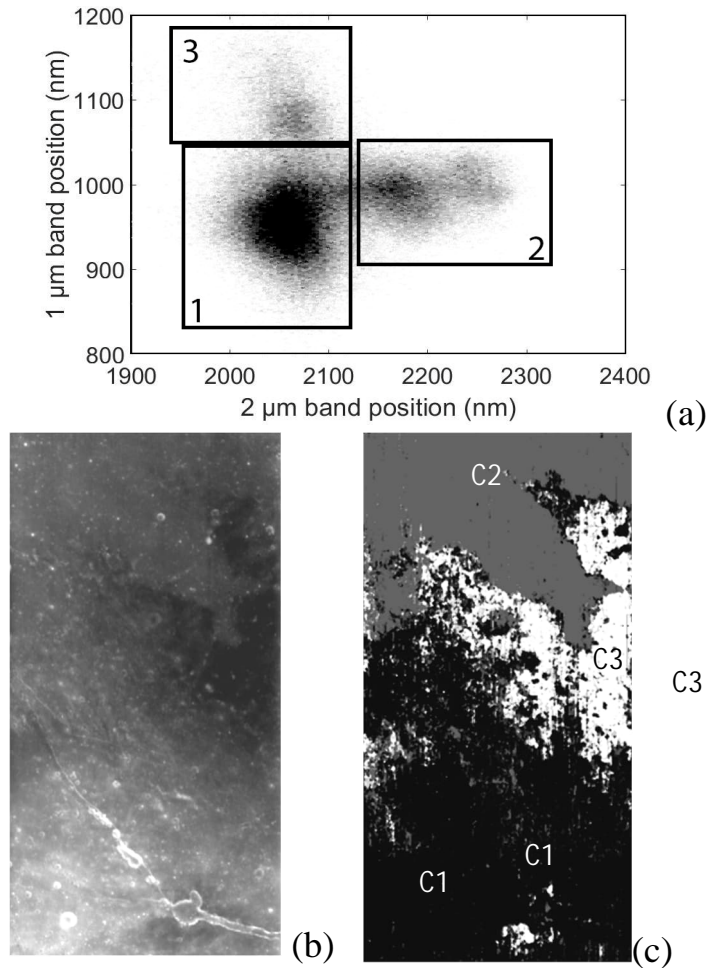


Figure 3.4 (a) Correlation diagram of the positions of the bands near 1 and 2  $\mu\text{m}$  with three marked classes. (b) The albedo map,  $A(750\text{nm})$ . (c) The map of classes: black, gray, and white colors correspond to the Class 1, Class 2, and Class 3, respectively.

We average the spectra within a radius of 5 nm at the center of each class as the most representative ones; these averaged spectra are shown in Fig. 3.5. We interpret Classes 1 and 2 as related to mare materials predominantly containing ortho- and clinopyroxenes, respectively. The Class 3 regions can be attributed to pyroclastic deposits. Class 3 has the 1  $\mu\text{m}$  band shifted to 1075 nm (Fig. 3.3c, Fig. 3.4c, Fig. 3.5b) and the position of the 2  $\mu\text{m}$  band is the same as for pyroxenes of the adjacent southern region (Fig. 3.5b). The one-pixel-sized features of Class 3 are



presented on the low albedo mare feature at the left border of the scene; we interpreted them as the residual noise of  $M^3$  data.

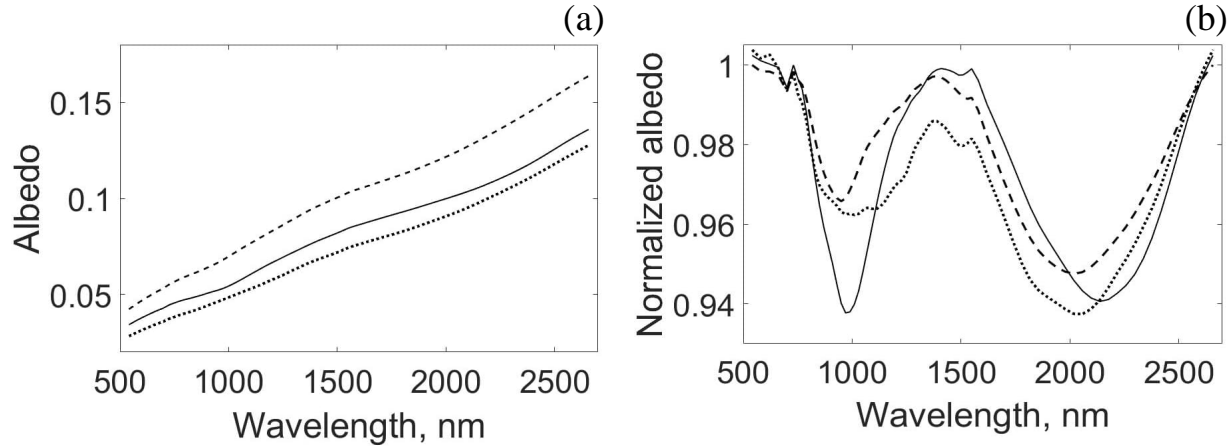


Figure 3.5 (a) The mean  $M^3$  spectra of each class represented in Fig. 3.4a: Class 1 (dashed line), Class 2 (solid line), and Class 3 (dots). (b) The same spectra with continuum removed.

### 3.3.2 The crater Hyginus

A distinct LPD surrounds the crater Hyginus (see Figs. 3.3a and 3.4c). This formation has a rather deep band at 1  $\mu\text{m}$  and the band's position is shifted to longer wavelengths ( $\sim 1050 - 1100 \text{ nm}$ ). It has also significantly lower albedo in the whole  $M^3$  range of wavelengths ( $\sim 540 - 3000 \text{ nm}$ ). These spectral data support the suggestion of Hawke and Coombs (1987) that the dark areas are pyroclastic deposits, and not mare basalt material (Wilhelms, 1968; Pike, 1976). The dark surroundings of the crater Hyginus has the radar CPR of about 0.08 that is similar to the LPD in Mare Vaporum (Carter et al., 2009).

Wilson et al. (2011) developed a model of the origin of the complex of Rima Hyginus. According to this model the crater Hyginus is a caldera-like formation produced by the surface setting into the empty cavity of the partly destroyed uppermost part of the sill of the dike (e.g., Head and Wilson, 2017). The radar data

of Carter et al. (2009) support the assumption that the graben and associated pits centered on graben represent the surface manifestation of the near-surface dike emplacement (Head, 1976; Head and Wilson, 1993, 2017). A comparison of the visible boundaries of the low CPR-value regions with low albedo areas mapped as pyroclastics led Wilson et al. (2011) to the conclusion that the Hyginus pyroclastic deposit is relatively thin ( $\leq 10$  m).

We perform a spectral study of Irregular Mare Patches (IMPs) in the crater Hyginus. The IMPs are presumably the collapsed voids, or cavities, in cooled lava flows that uncovered the substrate mare basalts. The triggers of this collapse might be different, e.g., a meteorite impacted the roof of cavity, or the aging and wear of the roof. For today only one object of this class, Ina, has been investigated with  $M^3$  spectral data due to its comparatively large size (Staid et al., 2011, Braden et al., 2014, Le Qiao et al., 2018, 2019). The  $M^3$  data improved with our additional processing allow for the consideration of many smaller IMPs up to the size of several  $M^3$  pixels, i.e. a few hundred meters. First of all, we use the LROC NAC image to identify these structures in the crater. Figure 3.6a is the portion of the NAC image M1114121068R with the four largest IMPs inside the main caldera identified with arrows. Figure 3.6b shows the same caldera on the portion of the  $M^3$  image. The resolution of  $M^3$  allows us to distinctly locate the two IMPs using reflectance data. Whereas many more IMP-structures (black several-pixels-sized features) are observed on the color ratio  $A(950\text{ nm})/A(750\text{ nm})$ , three of four structures are revealed in Fig. 3.6c.

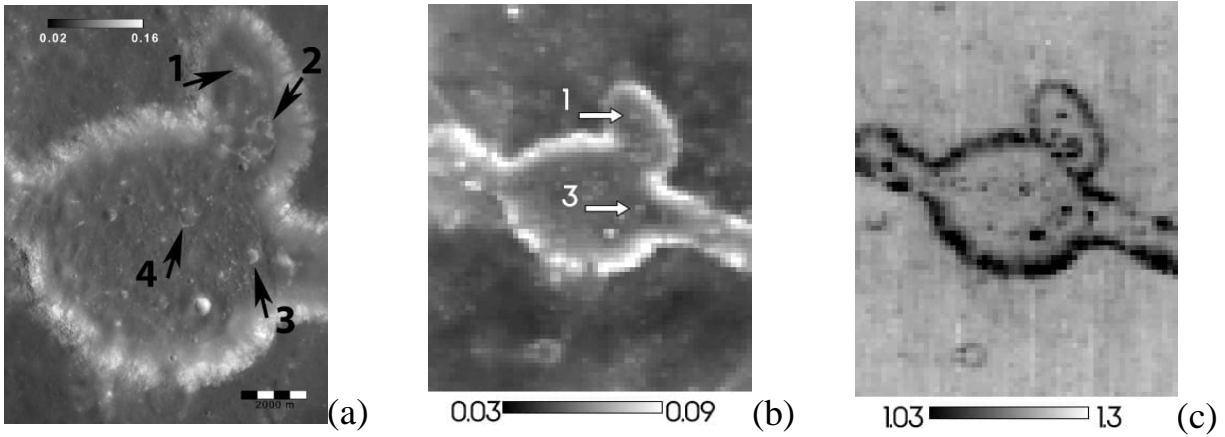


Figure 3.6 (a) The NAC image of Hyginus crater with IMP features identified with numbers; (b) the M<sup>3</sup> image of albedo at 750nm of the same crater, where only two IMPs are distinctly seen; (c) the M<sup>3</sup> color ratio  $C(950 \text{ nm}/750 \text{ nm})$ .

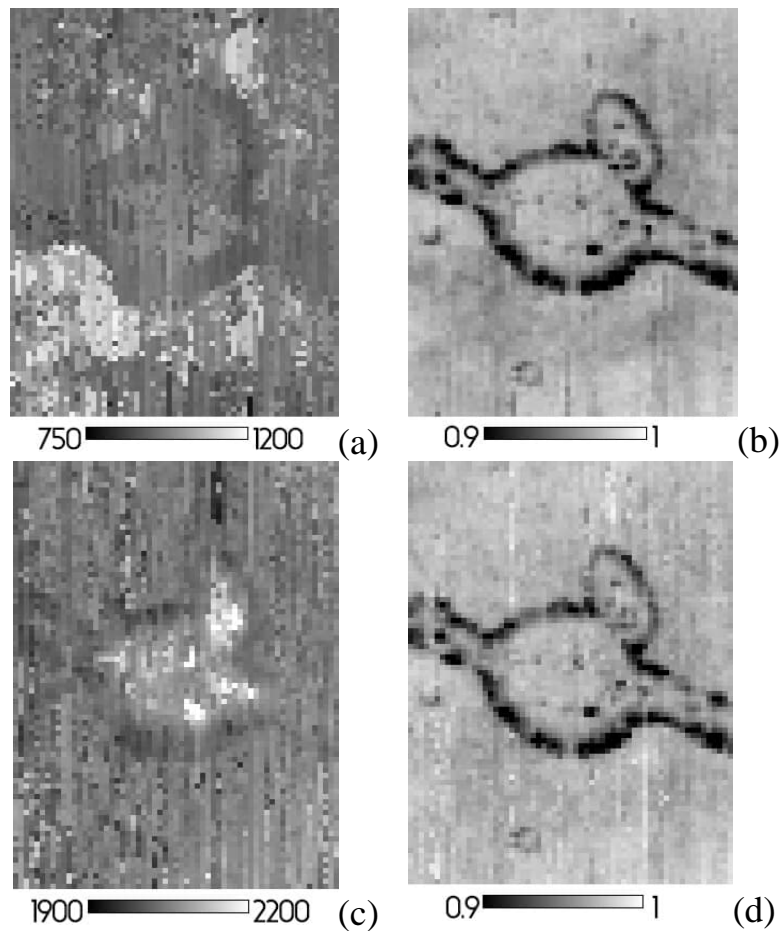


Figure 3.7 (a) The position of the 1  $\mu\text{m}$  band in nm. (b) The depth of the band at 1  $\mu\text{m}$ . (c) The position of the 2  $\mu\text{m}$  band in nm. (d) The depth of the band at 2  $\mu\text{m}$ .

For further spectral analysis we build the maps of the depths and positions of the 1 and 2  $\mu\text{m}$  bands (Fig. 3.7). Both depth maps are similar to the color ratio distributions presented above. These show that the bands on the IMPs are more prominent because of immaturity of the regolith. The position of the 1  $\mu\text{m}$  band is not sensitive to irregular mare patches and slopes of the crater Hyginus.

In Fig. 3.8a we present three spectra. One of them corresponds to the IMP 3 identified in Fig. 3.6a (solid line). The other two refer to the patch's surrounding (dashed line) and the steep crater wall (dotted line). The IMP's spectrum has more prominent absorption than its surroundings and almost the same albedo over the entire  $M^3$  spectral range. The 1  $\mu\text{m}$  band depth of the patch is close to that of the crater wall.

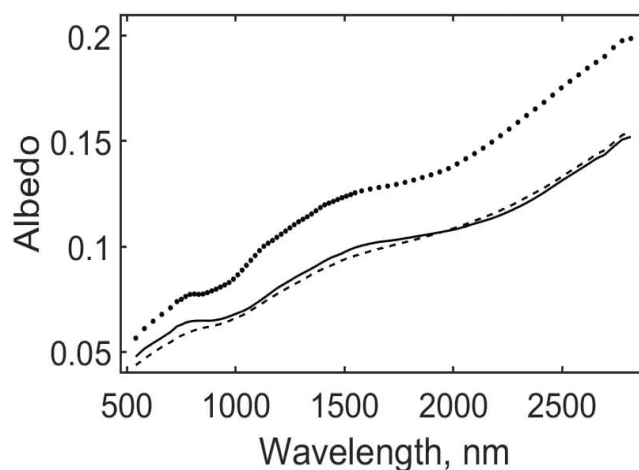


Figure 3.8 The spectra of the lunar mare IMP 3 (solid line), its surroundings (dashed), and steep crater wall (dotted).

The mentioned spectral features of IMPs also can be distinguished with higher resolution data of the Multi Imager onboard the Kaguya spacecraft (Ohtake et al., 2010). We use the portion of the image MIA\_3C5\_03\_06733N078E0063SC that depicts a portion of crater Hyginus (Fig. 3.9a) with a spatial resolution reduced to 60 m/pixel in 7 narrow spectral channels (415 nm, 750 nm, 900 nm, 950 nm,

1000 nm, 1050 nm, 1250 nm, 1550 nm). On these images the IMP also reveal similar spectral behavior as the areas of steep inclines: higher albedo, stronger 1  $\mu\text{m}$  absorption feature, and smaller average spectral slope (Fig. 3.9c). These results are consistent with  $M^3$  data and support the hypothesis that IMPs are relatively young due to the presence of immature regolith. The age of different IMPs is estimated with crater size-frequency distributions as less than 100 million years (Braden et al., 2014). This estimation is obtained using LROC NAC data and taking into account craters with  $D \geq 10\text{m}$ , although Braden et al. (2014) notes that the smooth regions of IMPs usually do not have enough craters to produce statistically significant crater counting. In the cases of the IMPs Cauchy-5, Ina, and Sosigenes, there are no clear equilibrium diameters that can confirm their young ages. According to the volcanological model of Qiao et al. (2018; 2019), characteristics of IMPs may modify the nature and evolution of superposed impact craters, thus producing anomalously young crater ages.

The position of the 2  $\mu\text{m}$  absorption band of the IMPs is surprisingly shifted to longer wavelengths (Fig. 3.7c). There may be a number of causes for this: shortcomings of thermal removal that affect the shape of the spectra, possible wrong estimation of the border of the absorption band with the numerical method of convex hull, and the presence of Mg-spinel in the mineral mixture (Cloutis et al., 2004). The most common forms of spinel found on the Moon are Fe, Cr, or Ti-rich opaque minerals. Non-opaque, low (Fe, Cr, Ti) spinel is usually referred as ‘Mg-spinel’ (Pieters et al., 2014). The presence of Mg-spinel in the mixture with pyroxenes should spectrally reveal itself as the deepening and/or broadening of the 2  $\mu\text{m}$  band.

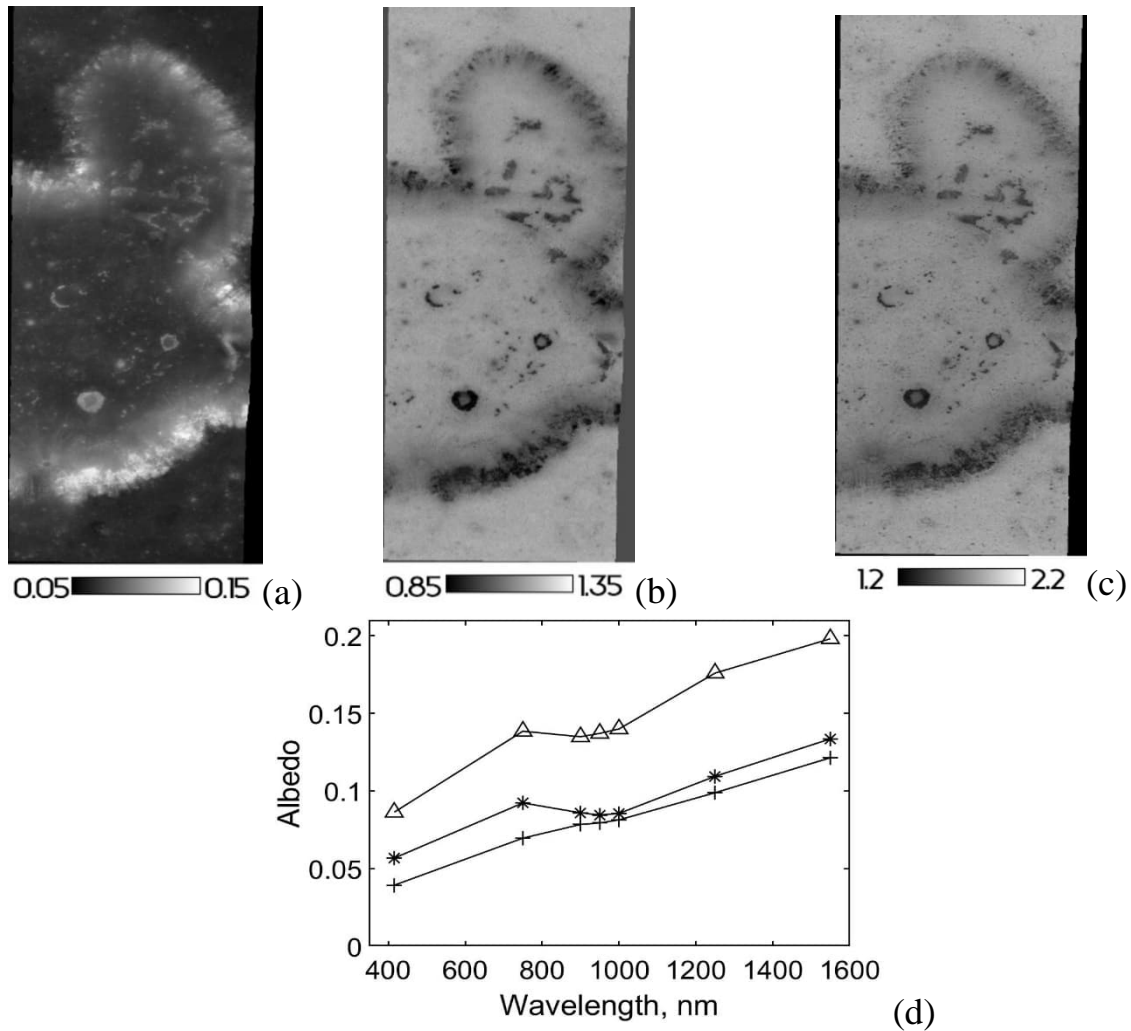


Figure 3.9 Representation of the MI data of crater Hyginus: (a) Reflectance at 750 nm; (b) The color ratio  $A(950 \text{ nm})/A(750 \text{ nm})$ ; (c) The color ratio  $A(1550 \text{ nm})/A(750 \text{ nm})$ . (d) The MI spectra of the same points that are shown in Fig. 3.8: the spectra of the lunar mare IMP 3 (\*) identified in Fig. 3.6, its surroundings (+), and the steep crater wall (Δ).

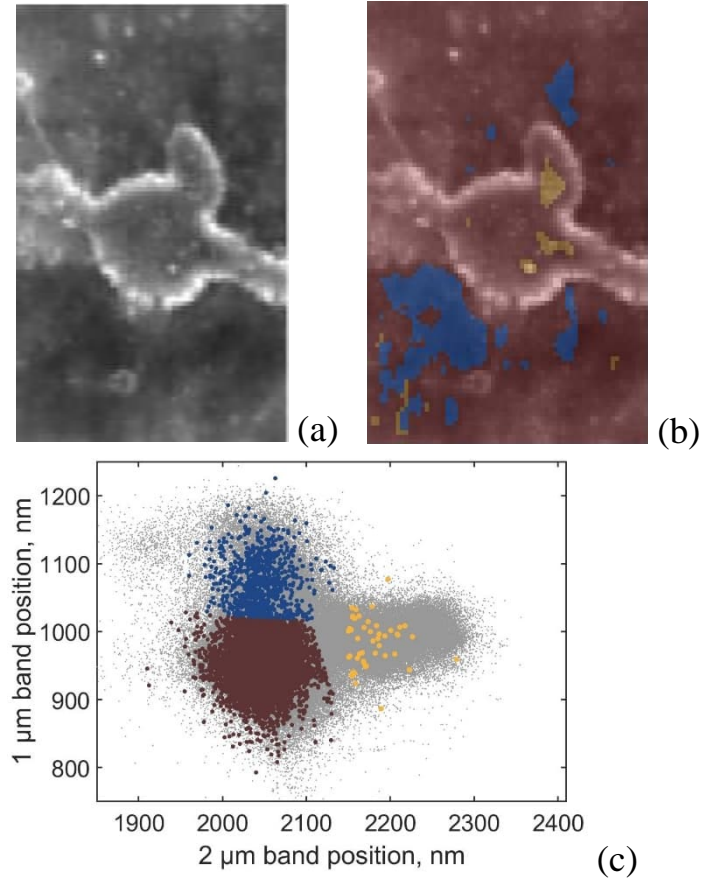


Figure 3.10 The M<sup>3</sup> albedo image of crater Hyginus at 750 nm (a). Albedo and class map images (b). The Adams correlation diagram (c).

It is of interest to inspect the areas corresponding to the classes in the diagram in Fig. 3.10a, with other optical methods. The phase-ratio method is one of them (e.g., Shkuratov et al., 1994, 2011). Mapping the ratio  $A(\lambda_1)/A(\lambda_2)$ , where  $\lambda_1$  and  $\lambda_2$  are different phase angle, provides information about the slope of phase curves in each image pixel (e.g., Kaydash et al., 2012). The higher the slope, the rougher the surface. Albedo also influences the slope, making it smaller, when the albedo increases. Such imagery allows one to estimate variations of the complexity of unresolved surface roughness and microtopography. We have successfully used the phase-ratio technique to study young craters (Shkuratov et al., 2011, 2012; Kaydash et al., 2014; 2018; Korokhin et al., 2016), Apollo (Kaydash et al., 2011;

Kaydash and Shkuratov, 2012) and Luna (Kaydash et al., 2013, 2014; Shkuratov et al., 2013) landing sites. This approach was also used to examine the opposition effect of the Moon (Shkuratov et al., 1999; Kreslavsky et al., 2000; Kreslavsky and Shkuratov, 2003; Velikodsky et al., 2011, 2016). Successful applications of phase-ratio imagery require the use of either similar illumination conditions of phase angle components (Kaydash et al., 2012) or information about topography of the area under study (Korokhin et al., 2014, 2018; Velichko et al., 2019, 2020). Recently a convenient approach was suggested (Velichko et al., 2019, 2020) allowing for the topography determination with the spatial resolution of initial images simultaneously with phase-ratio imagery. The accounting for the topography significantly suppress the shadow pattern.

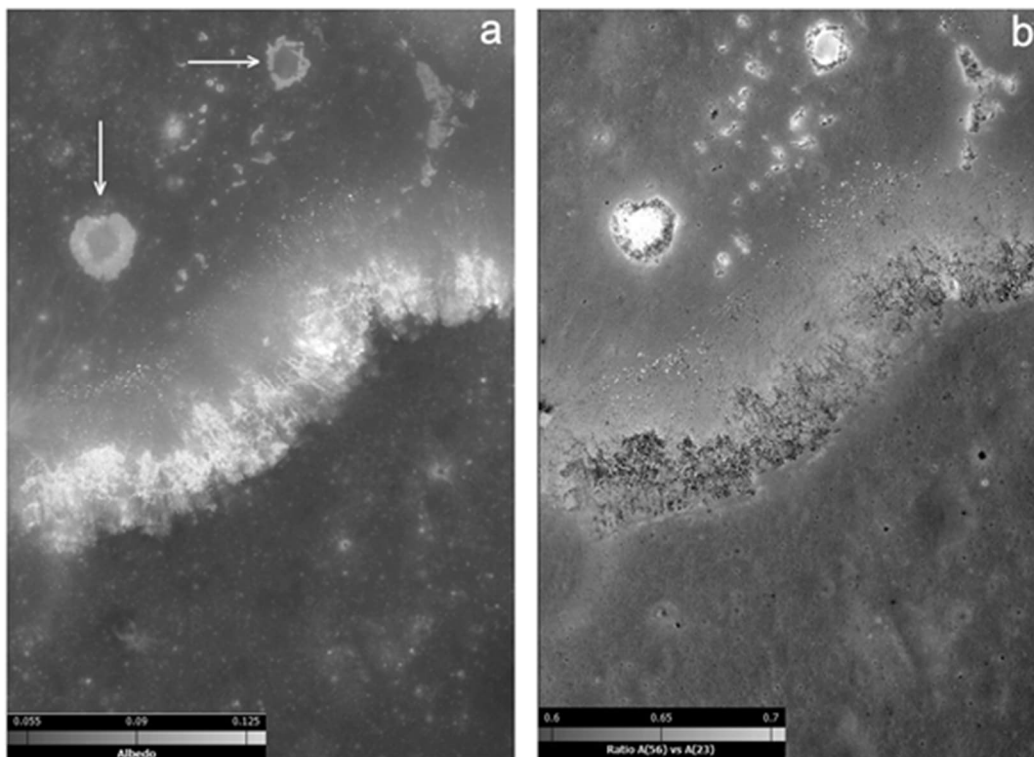


Figure 3.11 The southern edge of the Mare Vaporum. (a) and (b) correspond to the distributions of the albedo  $A(23^\circ)$  and the phase ratio  $A(56^\circ)/A(23^\circ)$ , respectively. Both images are processed with the procedure described in (Velichko et al., 2019, 2020). Brighter tones in (b) mean higher slopes of phase curves.



Omitting the details that can be found in the above references, we move on to the description of the phase-ratio image of the southern edge of the Mare Vaporum. Figures 3.11a,b show images  $A(23^\circ)$  and  $A(56^\circ)/A(23^\circ)$  that were computed using procedure described in (Velichko et al., 2019, 2020). This procedure allows one to eliminate the shadow pattern caused by the topography in both the images. We may see the areas associated with clinopyroxenes in Fig. 3.10 (yellow color) correspond to the formations marked with arrows in Fig. 3.11a. These are craters that could appear as a result of evolution in the crater Hyginus. The walls of these craters have a large slope, the wall regolith is constantly renovated, thus exposing the rough surface. The result of this is visible in Fig. 3.11b, where the crater rims look dark, despite the fact that they have a high albedo. The regolith, which has transported due to slope processes from the walls of these craters to their bottoms, may contain significant amount of clinopyroxenes (Class 2 in Figs. 3.4 and 3.10). The crumbled regolith smooths the roughness of the crater bottoms. Therefore, they stand out well on the image of the phase-ratio (Fig. 3.11b), as places of reduced roughness, having a high albedo. In contrast to Class 2, the material of Class 3 (pyroclastic glasses) does not seen neither in albedo  $A(23^\circ)$  nor phase-ratio  $A(56^\circ)/A(23^\circ)$  images (Fig. 3.11).

### 3.4 Conclusions

We provide a mineralogical description of the southern part of Mare Vaporum using the improved Chandrayaan-1 M<sup>3</sup> data, which allows one to assess with higher accuracy the depth and position of the 1  $\mu$ m and 2  $\mu$ m bands. We use the improved M<sup>3</sup> spectral data with largely suppressed intrinsic noise, which allows us to estimate spectral parameters at the 1-2 pixel scale of M<sup>3</sup> images, i.e. with 500 m spatial resolution. The Adams diagram permits one to distinguish between mineralogical compositions. Three types of minerals are established in the region: ortho- and clinopyroxenes and the pyroclastic glasses. Our investigations of IMPs in the crater Hyginus suggest these are young features, since their spectra have prominent absorption features. We find a shift of the position of the 2  $\mu$ m band to longer wavelengths. The possible causes of this can be the presence of Mg-spinel in the mixture with pyroxenes. We inspected the areas corresponding to the classes in the diagram with phase-ratio analysis of LROC NAC data: the areas associated with clinopyroxenes are distinguished both in albedo and phase-ratio images, having higher roughness than surrounding surface; in contrast to this the areas associated with pyroclastic glasses does not seen neither in albedo nor phase-ratio images. Overall, the spectral signatures of IMPs suggest its unusual mineral composition, which is in accordance with the conclusion of Qiao et al. (2018, 2019) of unique physical properties of IMP.

### 3.5 References

- Adams, J.B., 1974. Visible and near-infrared diffuse reflectance spectra of pyroxenes as applied to remote sensing of solid objects in the solar system. *J. Geophys. Res.* 79, 4829-4836.
- Bell, P.M., Mao, H.K., Weeks, R.A., 1976. Optical spectra and electron paramagnetic resonance of lunar and synthetic glasses – A study of the effects of controlled atmosphere, composition, and temperature. *Proc. Lunar Planet. Sci. Conf.*, 7<sup>th</sup>. LPI Houston, 2543–2559.
- Besse, S., Sunshine, J.M., Gaddis, L.R., 2014. Volcanic glass signatures in spectroscopic survey of newly proposed lunar pyroclastic deposits. *J. Geophys. Res. Planets* 119, doi:10.1002/2013JE004537.
- Blewett, D., Vaughan, W., Zhiyong Xiao, Chabot, N., Denevi, B., Ernst, C., Helbert, J., D’Amore, M., Maturilli, A., Head, J., Solomon, S., 2013. Mercury’s hollows: Constraints on formation and composition from analysis of geological setting and spectral reflectance. *J. Geophys. Res. Planets*, 118, 1013–1032, doi:10.1029/2012JE004174
- Braden, S.E., Stopar, J.D., Robinson, M.S., Lawrence, S.J., van der Bogert, C.H., Heisinger, H., 2014. Evidence for basaltic volcanism on the Moon within the past 100 million years. *Nature: Geoscience Letters*, 1-5, doi:10.1038/NGEO2252.
- Burns, R., 1993. Mineralogical applications of crystal field theory. Cambridge Univ. Press, Cambridge, 459 p.
- Carter, L.M., Campbell, B.A., Hawke, B.R., Campbell, D.B., Nolan, M.C., 2009. Radar remote sensing of pyroclastic deposits in the southern Mare Serenitatis and Mare Vaporum regions of the Moon. *J. Geophys. Res.*, 114, E11004, doi:10.1029/2009JE003406

- Carter, L.M., Hawke, B.R., Garry, W.B., Campbell, B.A., Giguere, T.A., Bussey, D.B.J., 2013. Radar observations of lunar hollow terrain. Lunar Planet. Sci. Conf., 44<sup>th</sup>. LPI Houston, abstract no 2146.
- Clark, R., King, T., Gorelick, N., 1987. Automatic continuum analysis of reflectance spectra. JPL Proceed. 3rd Airborne Imaging Spectrom. Data Analysis Workshop. 138-142.
- Cloutis, E., Gaffey, M.J., 1991. Pyroxene spectroscopy revised: Spectral compositional correlations and relationship to geothermometry. J. Geophys. Res., 96, 22,809 – 22,826.
- Cloutis, E.A., Sunshine, J.M., Morris, R.V., 2004. Spectral reflectance-compositional properties of spinels and chromites: Implications for planetary remote sensing and geothermometry, Meteorit. Planet. Sci., 39, 545–565, doi:10.1111/j.1945-5100.2004.tb00918.x
- Coombs, C.R., Hawke, B.R., 1992. Pyroclastic deposits on the western limb of the Moon, in: Proc. Lunar Planet. Sci. Conf. 22nd, pp. 303–312.
- Donaldson Hanna, K.L., Cheek, L.C., Pieters, C.M., Mustard, J.F., Greenhagen, B.T., Thomas, I.R., Bowles, N.E., 2014. Global assessment of pure crystalline plagioclase across the Moon and implications for the evolution of the primary crust. J. Geophys. Res. Planets, 119(7). 1516-1545.
- Elder C., Hayne P., Bandfield J.L., Ghent R., Williams J.-P., Donaldson Hana K.L., Paige D.A., 2017. Young lunar volcanic features: Thermophysical properties and Formation. Icarus 290. Doi: 10.1016/j.icarus.2017.03.004.
- Gaddis, L.R., Hawke, B.R., Robinson, M.S., Coombs, C., 2000. Compositional analyses of small lunar pyroclastic deposits using Clementine multispectral data. J. Geophys. Res. 105, 4245–4262.
- Glaspie L.M., Bennet K.A., Gaddis L.R., Donaldson Hanna K.L., Horgan B.H.N., Keszthelui L., Stopar J., and Lawrence S., 2019. Characterization of a

- potential compositional halo around Ina irregular mare patch. Lunar Planet. Sci. Conf., 50<sup>th</sup>. LPI Houston, abstract no 2889.
- Goswami, J. N. and Annadurai, M., 2009. Chandrayaan-1: India's first planetary science mission to the moon, *Current Science*, Vol. 96, No. 4, pp. 486-491.
- Grice J., Donaldson Hana K.L., Bowes N.E., Schultz P.H., Bennet K.A., 2016. Investigating young (<100 million years) irregular mare patches on the Moon using Moon Mineralogy Mapper observations. Lunar Planet. Sci. Conf., 47<sup>th</sup>. LPI Houston, abstract no 2106.
- Gustafson, J. O., J. F. Bell III, L. R. Gaddis, B. R. Hawke, and T. A. Giguere (2012), Characterization of previously unidentified lunar pyroclastic deposits using Lunar Reconnaissance Orbiter Camera data, *J. Geophys. Res.*, 117, E00H25, doi:10.1029/2011JE003893
- Hawke, B. R., and C. R. Coombs, 1987. Remote sensing studies of the Rima Hyginus region of the Moon, *Proc. Lunar Planet. Sci. Conf.*, 18-th, LPI Houston. 407 – 408.
- Hazen, R.M., Bell, P.M., and Mao, H.K., 1978. Effects of compositional variation on absorption spectra of lunar pyroxenes. *Proc. Lunar Planet. Sci. Conf.*, 9-th. LPI Houston. 2919-2934.
- Head, J.W., 1976. Lunar volcanism in space and time. *Rev. Geoph. Space Phys.* 14, 265-300.
- Head, J.W., Wilson, L., 1993. Lunar graben formation due to near-surface deformation accompanying dike emplacement. *Planet. Space Sci.* 41, 719-727.
- Head, J.W., Wilson, L., 2017. Generation, ascent and eruption of magma on the Moon: New insights into source depths, magma supply, intrusions and effusive/ explosive eruptions (Part 2: Predicted emplacement processes and observatios). *Icarus* 283, 176-223. doi:10.1016/j.icarus.2016.05.031.

- Isaacson, P.J., Pieters, C.M., Hiroi, T., Liu, Y., Dhingra, D., Klima, R.L., Taylor, L.A., 2011a. Reflectance spectroscopy of ilmenite: New constraints from Apollo sample measurements. Lunar Planet. Sci. Conf. 42nd. LPI Houston. 2130.
- Isaacson, P., Pieters, C., Besse, S., Clark, R., Head, J., Klima, R., Mustard, J., Petro, N., Staid, M., Sunshine, J., Taylor, L., Thaisen K., Tompkins, S., 2011b. Remote compositional analysis of lunar olivine-rich lithologies with Moon Mineralogy Mapper (M<sup>3</sup>) spectra. J. Geophys. Res. 116 E00G11.
- Klima, R.L., Pieters, C.M., Boardman, J.W., Green, R.O., Head-III, J.W., Isaacson, P.J., Mustard, J.F., Nettles, J.W., Petro, N.E., Staid, M.I., Sunshine, J.M., Taylor, L.A., Tompkins, S., 2011. New insights into lunar petrology: Distribution and composition of prominent low-Ca pyroxene exposures as observed by the Moon Mineralogy Mapper (M<sup>3</sup>), J. Geophys. Res., 116. E00G06. doi:10.1029/2010JE003719.
- Kaydash, V.G., Shkuratov, Y.G., 2012. Structural disturbance of the lunar surface caused spacecraft. Solar System Res. 46(2), 108-118. [doi.org/10.1134/S0038094612020050](https://doi.org/10.1134/S0038094612020050)
- Kaydash, V.G., Shkuratov, Y.G., 2014. Structure perturbations of the lunar surface near the landing site of “Lunokhod-1”. Solar System Res. 48(3), 167-175. [doi.org/10.1134/S0038094614030034](https://doi.org/10.1134/S0038094614030034)
- Kaydash, V., Shkuratov, Yu., Korokhin, V., Videen G., 2011. Photometric anomalies in the Apollo landing sites as seen from the Lunar Reconnaissance Orbiter. Icarus 211, 89–96. [doi.org/10.1016/j.icarus.2010.08.024](https://doi.org/10.1016/j.icarus.2010.08.024)
- Kaydash, V., Shkuratov, Yu., Videen, G., 2012. Phase-ratio imagery as a planetary remote sensing tool. J. Quant. Spectrosc. Rad. Transfer 113(18), 2601–2607. [doi.org/10.1016/j.jqsrt.2012.03.020](https://doi.org/10.1016/j.jqsrt.2012.03.020)

- Kaydash, V., Shkuratov, Y., Videen, G., 2013. Landing of the probes Luna 23 and Luna 24 remains an enigma. *Planet. Space Sci.* 89, 172–182.  
[doi.org/10.1016/j.pss.2013.08.021](https://doi.org/10.1016/j.pss.2013.08.021)
- Kaydash, V., Shkuratov, Y., Videen, G., 2014. Dark halos and rays of young lunar craters: a new insight into interpretation. *Icarus* 231, 22–33.  
[doi:10.1016/j.icarus.2013.11.025](https://doi.org/10.1016/j.icarus.2013.11.025).
- Kaydash, V., Shkuratov, Yu., Korokhin, V., Velichko S., Videen, G., 2018. The lunar surface around extremely fresh craters. *Icarus* 311, 258–270.  
[doi.org/10.1016/j.icarus.2018.04.024](https://doi.org/10.1016/j.icarus.2018.04.024)
- Korokhin, V.V., Velikodsky, Y.I., Shalygin, E.V., Shkuratov, Y.G., Kaydash, V.G., Gorden, V., 2014. Retrieving lunar topography from multispectral LROC images. *Planet. Space Sci.* 92, 65–76.  
[doi.org/10.1016/j.pss.2014.01.008](https://doi.org/10.1016/j.pss.2014.01.008)
- Korokhin, V., Shkuratov, Y., Kaydash, V., et al., 2016. Characterization of a photometric anomaly in lunar Mare Nubium. *Planet. Space Sci.* 122, 70–87.  
[doi.org/10.1016/j.pss.2016.01.011](https://doi.org/10.1016/j.pss.2016.01.011)
- Korokhin, V., Velikodsky, Y., Shkuratov, Y., Kaydash, V., Mall, U., Videen, G., 2018, Using LROC WAC data for Lunar surface photoclinometry. *Planet. Space Sci.* 160, 120–135. [doi.org/10.1016/j.pss.2018.05.020](https://doi.org/10.1016/j.pss.2018.05.020)
- Kreslavsky, M.A., Shkuratov, Y.G., Velikodsky, Y.I., Kaydash, V.G., Stankevich, D.G., Pieters, C.M., 2000. Photometric properties of the lunar surface derived from Clementine observations. *J. Geophys. Res.*, 105 (E8), 20,281–20,296.
- Kreslavsky, M.A., Shkuratov, Y.G., 2003. Photometric anomalies of the lunar surface: Results from Clementine data, *J. Geophys. Res.*, 108(E3), 5015.  
[doi.org/10.1029/2002JE001937](https://doi.org/10.1029/2002JE001937)

- Li, S., Milliken, R.E., 2016. An empirical thermal correction model for Moon Mineralogy Mapper data constrained by laboratory spectra and Diviner temperatures, *J. Geophys. Res. Planets*, 121, 2081–2107, doi:10.1002/2016JE005035
- Lucey, P.G., Taylor, G.I., Malaret, E., 1995. Abundance and distribution of iron on the Moon. *Science* 268. 1150–1153.
- Lucey, P.G., Blewett, D.T., Bradley, L.L., 2000a. Lunar iron and titanium abundance algorithm based on final processing of Clementine ultraviolet–visible images. *J. Geophys. Res.* 105, 20,297–20,305.
- Lucey, P.G., Blewett, D.T., Taylor, G.J., Hawke, B.R., 2000b. Imaging of the lunar surface maturity. *J. Geophys. Res.*, 105, 20,377– 20,386.
- McCord T.B., Adams J.B., 1973. Progress in remote optical analysis of lunar surface composition. *The Moon* 7, 453-474.
- Milliken, R., Li, S. Remote detection of widespread indigenous water in lunar pyroclastic deposits. *Nature Geosci.* 10, 561–565 (2017). [doi.org/10.1038/ngeo2993](https://doi.org/10.1038/ngeo2993)
- Mustard, J. F., et al., 2011. Compositional diversity and geologic insights of the Aristarchus crater from Moon Mineralogy Mapper data, *J. Geophys. Res.*, 116, E00G12, doi:10.1029/2010JE003726
- Ohtake, M., et al., 2010. Deriving the absolute reflectance of lunar surface using SELENE (Kaguya) Multiband Imager data. *Space Sci. Rev.*, 154(1-4), 57-77.
- Otake, H., Ohtake, M., Hirata, N., 2012. Lunar iron and titanium abundance algorithms based on Selene (Kaguya). 43<sup>rd</sup> LPSC, abstract no 1905.
- Pike, R. J., 1976. Geologic map of the Rima Hyginus region of the Moon. U. S. Geol. Surv. Misc. Geol. Invest. Map, I-945



- Pieters, C.M., Shkuratov, Y.G., Kaydash, V.G., Stankevich, D.G., Taylor, L., 2006. Lunar soil characterization consortium analyses: pyroxene and maturity estimates derived from Clementine data. *Icarus* 184, 83–101
- Pieters, C.M., 19 colleagues, 2009. The Moon Mineralogy Mapper (M<sup>3</sup>) on Chandrayaan-1. *Science* 326, 568-572.
- Pieters, C.M., Hanna, K.D., Cheek, L.C., Dhingra, D., Prissel, T., Jackson, C.R., Moriarty, D., Parman, S., Taylor, L.A., 2014. The distribution of Mg-spinel across the Moon and constraints on crustal origin, *American Mineralogist* 99 (10): 1893-1910. doi.org/10.2138/am-2014-4776
- Qiao L., Head J., Xiao L., Wilson L., Dufek J., 2018. The role of substrate characteristics in producing anomalously young crater retention ages in volcanic deposits on the Moon: Morphology, topography, subresolution roughness, and mode of emplacement of the Sosigenes lunar irregular mare patch. *Meteoritics & Planetary Science* 53, Nr 4, 778–812 doi:10.1111/maps.13003
- Qiao L., Head J.W., Ling Z., Yan J., 2019. Geological characterization of the Ina shield volcano Summit Pit crater on the Moon: Evidence for magmatic foams and anomalously young crater retention ages. *J. Geoph. Res: Planets* 124, 1100-1140. Doi: 10.1029/2018JE005841.
- Robinson, M.S., Thomas, P.C., Braden, S.E., Lawrence, S.J., Garry, W.B., and the LROC Team, 2010. High resolution imaging of Ina: morphology, relative age, formation. *Lunar Planet. Sci.*, 41<sup>st</sup>, LPI Houston. abstract no 2592.
- Robinson, M.S., Ashley, J.W., Boyd, A.K., Wagner, R.V., Speyerer, E.J., Hawke, B. Ray, Hiesinger, H., van der Bogert, C.H., 2012. Confirmation of sublunarean voids and thin layering in mare deposits. *Planet. Space Sci.* 69, 18–27.

- Singer, R.B., 1981. Near-infrared spectral reflectance of mineral mixtures: Systematic combinations of pyroxenes, olivine, and iron oxides. *J. Geoph. Res.* 86, 7967–7982.
- Staid M., 10 colleagues, 2011. The spectral property of Ina: New observations from the Moon Mineralogy Mapper. *Lunar Planet. Sci.*, 42<sup>nd</sup>, LPI Houston. abstract no 2499.
- Strain, P.L., El-Baz, F., 1980. The geology and morphology of Ina. *Lunar Planet. Sci.*, 11<sup>th</sup>, LPI Houston. 2437-2446.
- Stooke, P.J., 2012. Lunar meniscus hollows. *Lunar Planet. Sci.*, 43<sup>rd</sup>, LPI Houston, abstract no 1011. Schultz, P., Staid, M., Pieters C., 2006. Lunar activity from recent gas release, *Nature* 444, 184-186.
- Shkuratov, Y., Starukhina, L., Kreslavsky, M., Opanasenko, N., Stankevich, D., Shevchenko, V., 1994. Principle of perturbation invariance in photometry of atmosphereless celestial bodies. *Icarus* 109, 168–190.  
[doi.org/10.1006/icar.1994.1084](https://doi.org/10.1006/icar.1994.1084)
- Shkuratov, Y., Kreslavsky, M., Ovcharenko, A., Stankevich, D., Zubko, E., Pieters, C., Arnold, G., 1999. Opposition effect from Clementine data and mechanisms of backscatter. *Icarus* 141, 132-155.
- Shkuratov, Y., Kaydash, V., Korokhin, V., Velokodsky, Y., Opanasenko N., Videen, G., 2011. Optical measurements of the Moon as a tool to study its surface. *Planet. Space Sci.* 59, 1326-1371.  
[doi.org/10.1016/j.pss.2011.06.011](https://doi.org/10.1016/j.pss.2011.06.011)
- Shkuratov, Y., Kaydash, V., Videen, G., 2012. The crater Giordano Bruno as seen with optical roughness imagery. *Icarus* 218, 525–533.  
[doi.org/10.1016/j.icarus.2011.12.023](https://doi.org/10.1016/j.icarus.2011.12.023)
- Shkuratov, Y., Kaydash, V., Sysolyatina, X., Razim, A., Videen G., 2013. Lunar surface traces of engine jets of Soviet sample return probes: The enigma of

- Luna-23 and Luna-24 landing sites. *Planet. Space Sci.* 75. 28–36.  
[doi.org/10.1016/j.pss.2012.10.016](https://doi.org/10.1016/j.pss.2012.10.016)
- Shkuratov Y., Surkov Y., Ivanov M., Korokhin V., Kaydash V., Videen G., Pieters C., Stankevich D., 2019. Improved Chandrayaan-1 M<sup>3</sup> data: A northwest portion of the Aristarchus Plateau and contiguous maria. *Icarus* 321, 34–49.
- Sunshine, J.M., Pieters, C.M., 1993. Estimating model abundances from the spectra of natural and laboratory pyroxene mixtures using the Modified Gaussian Model. *J. Geophys. Res.* 98, 9075-9087.
- Sunshine, J.M., Pieters, C.M., Pratt, S.F., 1990. Deconvolution of mineral absorption bands: An improved approach. *J. Geophys. Res.* 95, 6955-6966.
- Surkov, Y., Shkuratov, Y., Kaydash, V., Korokhin, V., Videen, G., 2020. Lunar ilmenite content as assessed by improved Chandrayaan-1 M<sup>3</sup> data. *Icarus* 341, id.113661. doi:[10.1016/j.icarus.2020.113661](https://doi.org/10.1016/j.icarus.2020.113661)
- Velichko, S., Korokhin, V., Kaydash, V., Shkuratov, Yu., Videen, G., 2019. Removal of the topography effect from phase-ratio images using LROC NAC data. LPSC-50th, Abstract #1544.
- Velichko S.F., Korokhin V.V., Velikodsky Y.I., Kaydash V.G., Shkuratov Y.G., Videen G., 2020. Removal of topographic effects from albedo and phase-ratio images using LROC NAC data. *Lunar Planet. Sci.*, 51, LPI Houston. Abstract #1150.
- Velikodsky, Y.I., Opanasenko, N.V., Akimov, L.A., Korokhin, V.V., Shkuratov, Y.G., Kaydash, V.G., Videen, G., Ehgamberdiev, Sh.A., Berdalieva, N.E., 2011. New Earth-based absolute photometry of the Moon. *Icarus* 214(1). 30-45. [doi.org/10.1016/j.icarus.2011.04.021](https://doi.org/10.1016/j.icarus.2011.04.021)
- Velikodsky, Y.I., Korokhin, V.V., Shkuratov, Y.G., Kaydash, V.G., Videen G., 2016. Opposition effect of the Moon from LROC WAC data. *Icarus* 275, 1-15. [doi.org/10.1016/j.icarus.2016.04.005](https://doi.org/10.1016/j.icarus.2016.04.005)

- Weitz, C.M., Head III, J.W., Pieters, C.M., 1998. Lunar regional dark mantle deposits: Geologic, multispectral, and modeling studies, *J. Geophys. Res.*, 103, 22,725–22,759, doi:10.1029/98JE02027
- Whitaker, E., 1972. An unusual mare feature. *Apollo 15 Prelim. Sci. Rep.*, NASA SP-289, 2584–2585.
- Whitten, J., Head, J., Staid, M., Pieters, C., Mustard, J., Clark, R., Nettles, J., Klima, R., Taylor, L., 2011. Lunar mare deposits associated with the Orientale impact basin: New insights into mineralogy, history, mode of emplacement, and relation to Orientale Basin evolution from Moon Mineralogy Mapper (M<sup>3</sup>) data from Chandrayaan-1, *J. Geophys. Res.*, 116, E00G09, doi:10.1029/2010JE003736.
- Wilhelms, D. E., 1968. Geologic map of the Mare Vaporum Quadrangle of the Moon, U.S. Geol. Surv. Misc. Geol. Invest. Map, I-548.
- Wilhelms, D.E., 1987. *The Geologic History of the Moon*, USGS Prof. Paper 1348.
- Wilhelms, D.E., McCauley, J.F., 1971. Geologic Map of the Near Side of the Moon, USGS Map 1-703 (1:5,000,000 scale)
- Wilson, L., Hawke, B.R., Giguere, T.A., et al., 2011. An igneous origin for Rima Hyginus and Hyginus crater on the Moon. *Icarus* 215, 584–595.
- Yamamoto, A., Furuta, R., Ohtake, V., Haruyama, J., Matsunaga, T., Otake, H., 2013. TiO<sub>2</sub>, FeO, and texture analysis map of lunar crater Ina, based on SELENE Multiband Imager data. *Lunar Planet. Sci.*, 44th, LPI Houston, abstract no 1855.

## **CHAPTER 4. [PAPER] LUNAR ILMENITE CONTENT AS ASSESSED BY IMPROVED CHANDRAYAAN-1 M3 DATA**

We map ilmenite abundance on the Moon surface using Chandrayaan-1 M3 data, using the strength of the ilmenite absorption band near 1550 nm. The mapping is carried out for an area comprising the border between Mare Serenitatis and Mare Tranquillitatis. We use an improved filtration of the strip noise that is characteristic of Chandrayaan-1 M3 data. The relation between ilmenite and TiO<sub>2</sub> abundances determined with UV-Vis color ratios is discussed. We compare the total titanium distributions with what is assessed from the ilmenite content, finding in all cases  $\text{TiO}_2^{\text{total}} > \text{TiO}_2^{\text{ilmenite}}$ . This suggests that titanium is a component of not only ilmenite. A map of the difference between total and in-ilmenite titanium abundances is presented.

## 4.1 Introduction

The assessment of the chemical and mineral distributions over the Moon's surface can provide important information about the interior and geology of the Moon as well as the surface processes such as space weathering. Ilmenite is an oxide mineral  $\text{FeTiO}_3$  that is common in lunar basalts. This is a fairly dark mineral and therefore has poor optical spectra that are not usually used in remote sensing. Lunar ilmenite includes a significant portion of lunar surface titanium. This enables indirect assessments of the ilmenite abundance using estimates of titanium content.

The titanium abundance is often determined from that of  $\text{TiO}_2$ . Different techniques to evaluate this abundance remotely have been developed. All of them are based on empirical correlations between  $\text{TiO}_2$  content of the returned regolith samples and their spectral slopes in the UV-Vis range (e.g., Charette et al., 1974; Pieters and McCord, 1976; Johnson et al., 1991; Lucey et al., 2000; Shkuratov et al., 1999a; Gillis et al., 2003; Korokhin et al., 2008, 2016; Robinson et al., 2007). The spectral slopes are characterized by the color ratio  $C(\lambda_1/\lambda_2) = A(\lambda_1)/A(\lambda_2)$ , where  $A(\lambda)$  is the spectral albedo,  $\lambda_1$  and  $\lambda_2$  are different wavelengths. The spectral slope in the range 400 – 560 nm is related to the charge transfer mechanism  $\text{O}^{2-} \rightarrow \text{Ti}^{4+}$  and  $\text{O}^{2-} \rightarrow \text{Fe}^{2+}$  (Burns, 1993) as well as to nano-phase iron that is in regolith grains (Hapke 2001). It should be emphasized that on the lunar surface the abundances of  $\text{Fe}^{2+}$  and  $\text{Ti}^{4+}$  are closely correlated to each other (e.g., Shkuratov et al., 1999a). Gamma-ray spectroscopy also has been used in measurements of Ti abundance, although with much lower spatial resolution (Prettyman et al., 2006). Gamma-ray titanium data also have been exploited in conjunction with optical measurements (Shkuratov et al., 2005).

There are several empirical expressions for an approximate assessment of the TiO<sub>2</sub> content in the lunar maria. One of them can be obtained from data of Pieters and McCord (1976):

$$\text{TiO}_2[\%] = a \exp \left[ bC(400 \text{ nm} / 560 \text{ nm}) \right], \quad (4.1)$$

where  $a = 8 \cdot 10^{-8}$  and  $b = 21$ . Later it was found that different types of mare basalts may have dependences with different constants  $a$  and  $b$  (Gillis et al., 2003), i.e. Eq. (4.1) is not universal. This formula also cannot be applied to TiO<sub>2</sub> estimations for bright young craters, and it also is very unreliable for highland regions. To take into consideration the influence of the maturity degree on titanium estimates, Lucey et al., (2000) suggested the following empirical equation obtained for *Clementine* data from the UVVis camera (Nozette et al., 1994).

$$\text{TiO}_2[\%] = 3.71 \left\{ \arctan \left[ \frac{C(415 \text{ nm}/750 \text{ nm}) - 0.42}{A(750 \text{ nm})} \right] \right\}^{5.98}, \quad (4.2)$$

Where  $A(\lambda)$  is albedo in %. Using Eq. (4.2) requires caution, since this formula predicts too high content of TiO<sub>2</sub> (e.g., Korokhin et al., 2008). Sato et al. (2017) reported a close linear correlation between the LRO WAC color ratio  $A(321 \text{ nm})/A(415 \text{ nm})$  and TiO<sub>2</sub> abundance. The correlation is described as follows

$$\text{TiO}_2[\%] = 100C(321 \text{ nm}/415 \text{ nm}) - 68.9, \quad (4.3)$$

with correlation coefficient 0.98. The TiO<sub>2</sub> map by Sato et al. (2017) should be considered to be valid only for the mare regions. The map [http://wms.lroc.asu.edu/lroc/view\\_rdr/WAC\\_TIO2](http://wms.lroc.asu.edu/lroc/view_rdr/WAC_TIO2) seems to be more adequate, than the one obtained using Eq. (4.2). We use these data to study the total and ilmenite titanium distributions over the mare surface.

Ilmenite has its own spectral signature, which is the absorption band near 1550 nm. This band is considered to be formed by a heterogeneous intervalence charge transfer  $\text{Fe}^{2+} \rightarrow \text{Ti}^{4+}$  (Burns, 1993). The mechanism leading to the transfer is

a delocalization of electrons between adjacent cations with the formation of a molecular orbital. This hypothesis is reinforced by the large width of this band. The signature near 1550 nm makes it possible to directly assess the abundance of ilmenite in the lunar surface material producing measurements of the band intensity (Surkov et al., 2019). In this paper we study such a possibility using data obtained with the Moon Mineralogy Mapper ( $M^3$ ) that is the scanning spectrometer installed on board *Chandrayaan-1*, i.e. the lunar polar orbiter of the Indian Space Research Organization (ISRO). The  $M^3$  allowed measurements in the spectral range 500–3000 nm (Pieters et al., 2009) that fully encloses the ilmenite band. We investigate a region comprising vicinities of the border between Mare Serenitatis and Mare Tranquillitatis (Fig. 4.1), including the *Apollo-17* landing site. Mare Tranquillitatis contains areas with high abundance of  $TiO_2$  (e.g., Johnson et al., 1991; Korokhin et al., 2008).

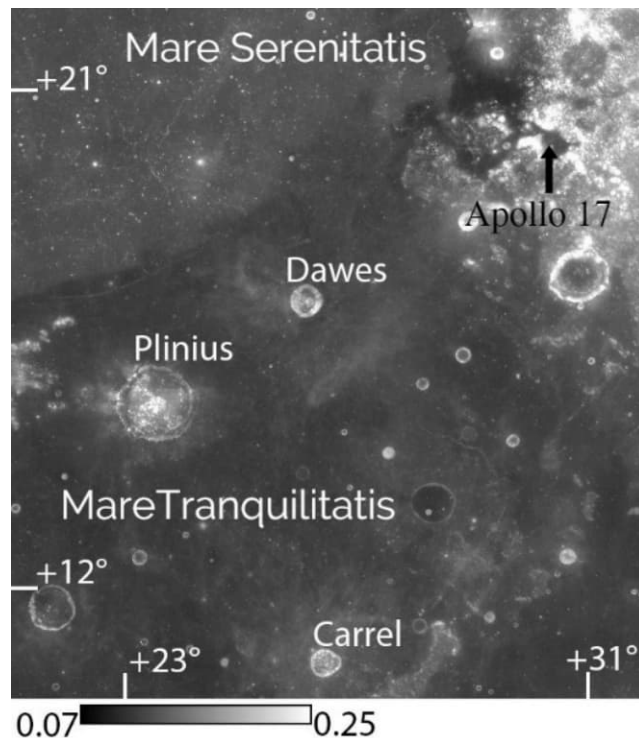


Figure 4.1 The seamless LRO WAC mosaic of Mare Serenitatis and Mare Tranquillitatis



## 4.2 Source data and extra M<sup>3</sup> data processing

The whole M<sup>3</sup> image set is divided into several optical periods. Each of them consists of two months with the best illumination conditions, when the solar angle measured from the surface normal at equator was from  $-30^0$  to  $+30^0$ , and two weeks before/after these months (the solar angle was from  $\pm 30^0$  to  $\pm 45^0$ ). Optical period 1 was devoted to the low-resolution data acquisition. All high-resolution hyperspectral images were expected to be obtained during the other periods. However, in the second period, the orbiter changed its orbit from 100 km to 200 km due to technical problems, resulting in significantly lower resolution. Moreover, the loss of the satellite connection made this optical period the last. Nevertheless, before the interruption of this mission, high-resolution images had covered over 95% of the Moon's surface. Efforts were made by mission research groups to calibrate and process the M<sup>3</sup> data (Lundeen et al., 2011), and now the set of hyperspectral images with a spatial resolution of approximately 100 m/pixel in 85 narrow spectral bands in the range of wavelengths from 400 to 3000 nm are available for scientific interpretation. All the M<sup>3</sup> images are long strips (about 85 km in width) extended along the meridians, since the *Chandrayaan-1* has a polar orbit.

We choose a region with supposedly large variations of ilmenite abundance, for which qualitative M<sup>3</sup> data are available. These are areas near the border between low-Ti Mare Serenitatis and high-Ti Mare Tranquillitatis (see Fig. 4.1). There are three especially attractive sites to test our new technique based on the measurements of the 1550 nm band depth: (1) the central peak and wall of the crater Plinius; (2) the ejecta blanks of the crater Dawes, which are convenient to see how our technique manifests itself in the case of rather thin TiO<sub>2</sub> abundance variations; and (3) the Taurus-Littrow valley, in which the *Apollo-17* landing site is

located. We use suitable parts of four  $M^3$  overlapping strips with the solar angles close to  $40^\circ$  and close azimuths of the Sun in order to image and characterize this region. All images were downloaded from [pds-imaging.jpl.nasa.gov/data/m3/CH1M3\\_0004/DATA/20090415\\_20090816/](https://pds-imaging.jpl.nasa.gov/data/m3/CH1M3_0004/DATA/20090415_20090816/), which are somewhat spoiled by the narrow strip-like artifacts, and hence, demand extra processing steps to provide reliable assessment and mapping of spectral parameters. Significant progress has recently been achieved in filtering such artifacts (Shkuratov et al., 2019). In the first step of the filtering, the spectrum of each pixel is smoothed by a convolution with a Gaussian function. The second step is the strip-noise filtration using a Fourier transform.

Figure 4.2 demonstrates that the  $M^3$  spectra have many small oscillations related to random noise. The 1D discrete Gaussian kernel is characterized by the width of a  $\lambda$ -convolution window, which is chosen empirically, taking into account the following: (1) the kernel should not be too wide; (2) the spectra should be as smooth as possible; (3) the signal averaged over the image in each spectral channel must not be changed; we used the limits  $\pm 0.2\%$ . Qualitative indicators of the noise processing are the absence of lunar details in the ratio of the images obtained before and after the  $\lambda$ -convolution, and the presence of only vertical strips in this ratio. Fig. 4.3 shows such an example, where the images (a) and (b) represent the cases before and after the  $\lambda$ -convolution, and the image (c) shows the ratio (a)/(b). As one can see from Fig. 4.3, the intensity of noise strips in (b) noticeably decreases after the  $\lambda$ -convolution, nevertheless, they do not vanish completely. We here used the kernel width of about 3 spectral pixels on the level of the half-height of the Gaussian function as an optimal.

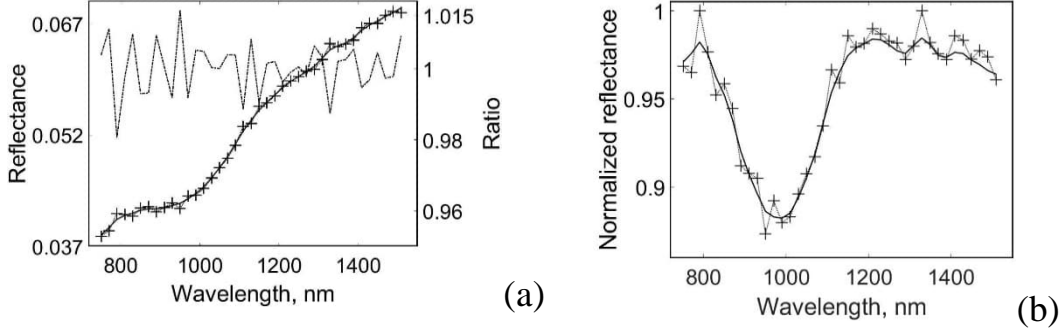


Figure 4.2 An example of a spectrum between 750 nm and 1550 nm (a). Crosses and solid line represent the spectrum before and after the  $\lambda$ -convolution, respectively, and the ratio of them is shown with dashed line; the same spectrum divided by its convex hull calculated over the whole-range spectrum (b).

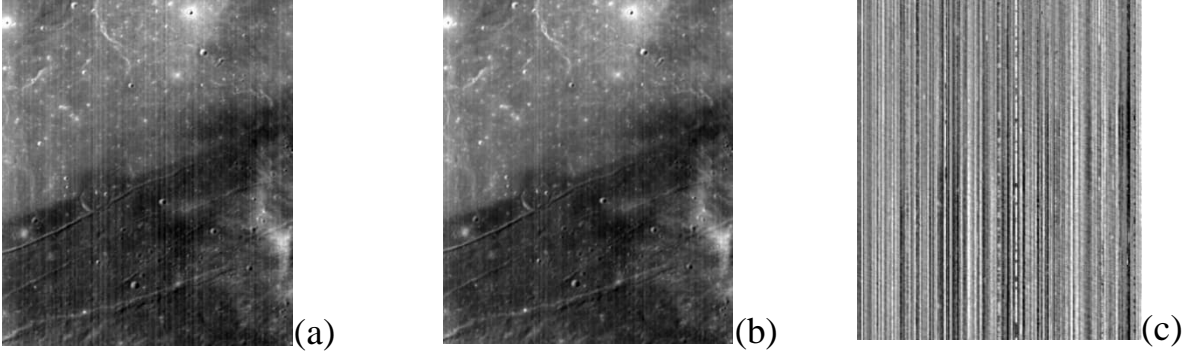


Figure 4.3 The images of the portion of the scene under investigation at 750 nm spectral channel (a) and (b) correspond to the cases before and after the  $\lambda$ -convolution, respectively. The image (c) represents the ratio (a)/(b). The images correspond to the frame shown in Fig. 4.1.

In the second step of the processing we have used a harmonic analysis of the image in each spectral channel with the 2D discrete Fourier transform (Shkuratov et al., 2019). We produce the transform  $F(\omega_x, \omega_y)$  of the image  $f(x, y)$ :

$$F(\omega_x, \omega_y) = \frac{1}{2\pi} \int_{-\infty}^{\infty} \exp(-i(\omega_x x + \omega_y y)) f(x, y) dx dy, \quad (3.4)$$

where  $\omega_x$  and  $\omega_y$  are the coordinates in the Fourier plane. Then, we may find and suppress the frequencies responsible for the stripes, using a filter  $A(\Omega, \omega_x, \omega_y)$   $A(\Omega, \omega_x, \omega_y)$ , where  $\Omega$  is the domain, where the stripe frequencies are mainly

localized. For instance, this could be a simple rejection filter (Shkuratov et al., 2019)

$$\Lambda(C, \Omega, \omega_x, \omega_y) = \begin{cases} C, & \text{if } \omega_x, \omega_y \in \Omega \\ 1, & \text{if else} \end{cases}, \quad (3.5)$$

where  $C$  is a small constant. After filtration we may produce the inverse Fourier transform, resulting in an image without or almost without the stripe clutter.

$$f(x, y) = \frac{1}{2\pi} \int_{-\infty}^{\infty} \exp(i(\omega_x x + \omega_y y)) \Lambda(C, \Omega, \omega_x, \omega_y) F(\omega_x, \omega_y) d\omega_x d\omega_y, \quad (3.6)$$

For practical implementations we use a discrete representation of the Fourier integrals

$$F_{p,q} = \sum_{j=0}^{m-1} \sum_{k=0}^{n-1} \exp(i(\omega_p j + \omega_q k)) f_{j,k}, \quad (3.7)$$

$$f_{j,k} = \frac{1}{mn} \sum_{p=0}^{m-1} \sum_{q=0}^{n-1} \exp(-i(\omega_p j + \omega_q k)) \Lambda(\Omega, \omega_p, \omega_q) F_{p,q}, \quad (3.8)$$

where  $\omega_p = -2\pi p/m$  and  $\omega_q = -2\pi q/n$  are the coordinates in the frequency plane,  $p = 0, 1, 2, \dots, m-1$ , and  $q = 0, 1, 2, \dots, n-1$ ,  $m$  and  $n$  characterize the image sizes in the pixel number.

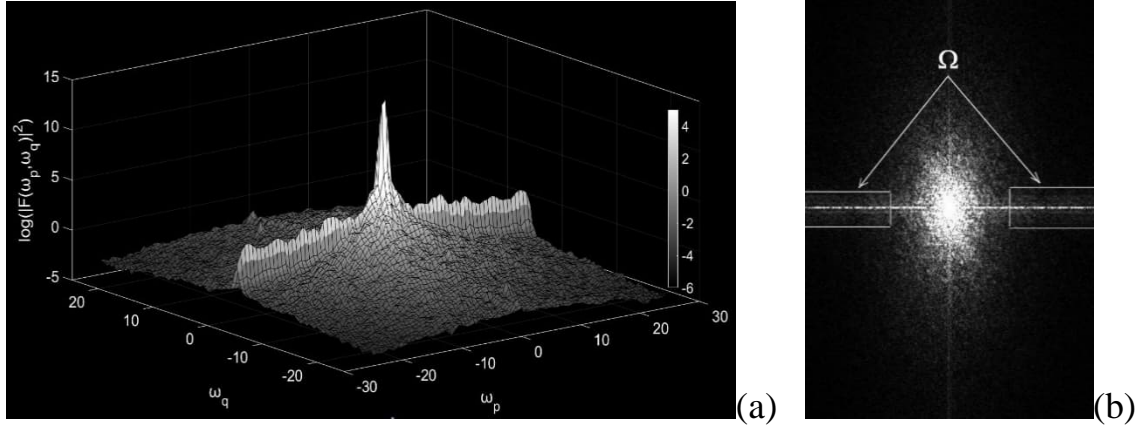


Figure 4.4 The logarithm of the power spectrum of an  $M^3$  image of the area shown in Fig. 4.1 is depicted in (a). The strip noise is mainly localized in the wings of the comb-like formation. (b) represents the view from above, indicating the area  $\Omega$  of the noise localization.

Eq. (4.7) allows one to separate the strip noise and lunar pattern and to clip the noise with minimal loss of useful information, especially, when the signal-to-noise ratio is sufficiently small. Fig. 4.4 shows the power spectrum for the area under study. The comb-like formations extending horizontally from the center to edges are a localization of the strip noise. Results of the two-step filtration of images similar to those shown in Fig. 4.3a are represented in Fig. 4.5a, b. Almost no narrow strips on the albedo  $A(950 \text{ nm})$  and color ratio  $C(950 \text{ nm}/750 \text{ nm})$  images are observed.

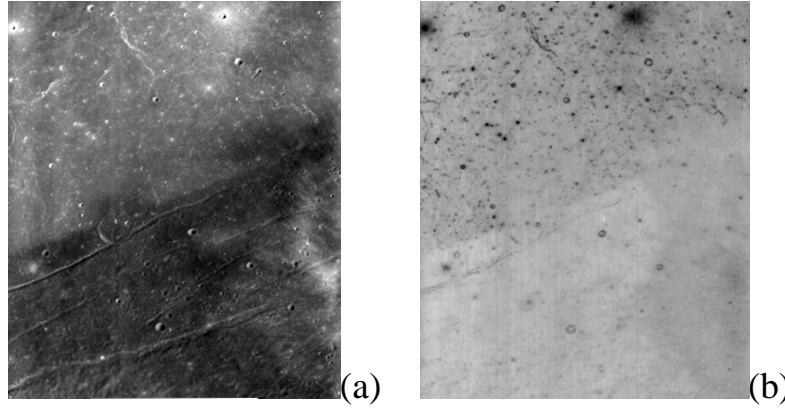


Figure 4.5 Images of the albedo  $A(750 \text{ nm})$  (a) and the color ratio  $A(950 \text{ nm})/A(750 \text{ nm})$  (b). The images correspond to the frame shown in Fig. 4.1. We use the filter described by Eq. (4.5) with  $C = 0$ .

Unfortunately, the filter described by Eq. (4.5) is vulnerable to the presence of very high contrast details with sharp borders. In this case, artifacts may appear in the result. Fig. 4.6a shows a small part of the non-filtered image M3G20090731T045352\_V01\_RFL.IMG comprising the crater Dawes and its vicinity (see Fig. 4.1). The same area is shown after processing with a filter described by Eq. (4.5) at  $C = 0$ . The artifact related to the filtering is associated with the crater Dawes; this is the wide dark strip (see Fig. 4.6b). The artifact is due to the restriction of the spatial spectrum of the image at the filtration, which originates from the Gibbs effect (e.g., Gottlib and Shu Chi-Wang, 1997). Such artifacts are especially common in color ratio images. For instance, Fig. 4.6d-f show the ratio  $C(950 \text{ nm}/750 \text{ nm})$  retrieved from non-filtered and filtered data, respectively. Thus, the filter we used for the Fourier filtration restricts us to images that are not of high contrast. For example, these should be images acquired at phase angles not so large that they produce long deep shadows. The resulting artifacts can be interpreted as real lunar details, misleading geologists. In order to extend the working set of  $M^3$  data to include images made at large phase angles and remove these artifacts, we propose an improved Fourier filter that allows

significant suppression of the Gibbs effect. Oscillations around the sharp borders in the image occur after decreasing the number of elements of the Fourier series. The Gibbs effect manifestation depends on the shape and position of  $\Omega$  (Fig. 4.4b). The problem of the crater Dawes artifact lays in the full and sharp zeroing of all spatial frequencies in  $\Omega$ . A more sophisticated approach should be applied to achieve satisfactory suppression of the artifact. We omit consideration of any subtleties of the harmonic analysis (Brillinger, 2001), from which the filter can be derived. Considering the geometrical characteristics of the area  $\Omega$ , we suggest using the following:

$$\Lambda(\omega_p, \omega_q, l, \sigma_1, \sigma_2) = \begin{cases} \exp\left(-\left(\frac{\omega_p^2}{2\sigma_1} + \frac{\omega_q^2}{2\sigma_2}\right)\right) & \text{if } (\omega_p, \omega_q) \in \Omega \\ 1 & \text{otherwise} \end{cases} \quad (4.9)$$

Where  $\sigma_1$  and  $\sigma_2$  are the filter parameters. Fig. 4.6 shows results of application of this new filter to the images containing crater Dawes. As can be clearly seen, filter (9) preserves the signal better as compared to Eq. (4.5).

### 4.3 Mapping ilmenite abundance

As has been mentioned, there are two approaches to assess the ilmenite abundance. The first is based on an analysis of spectral characteristics of the mineral. The second one is indirect; this is based on estimations of  $\text{TiO}_2$  content correlated with the UV-Vis slope that is influenced by other factors in addition to  $\text{TiO}_2$ . We used the  $\text{TiO}_2$  distribution (WAC\_TIO2\_E350N0450.IMG), derived from the empirical correlation between  $C(321 \text{ nm}/415 \text{ nm})$  and the  $\text{TiO}_2$  abundance (Sato et al., 2017), from [http://wms.lroc.asu.edu/lroc/view\\_rdr/WAC\\_TIO2](http://wms.lroc.asu.edu/lroc/view_rdr/WAC_TIO2).

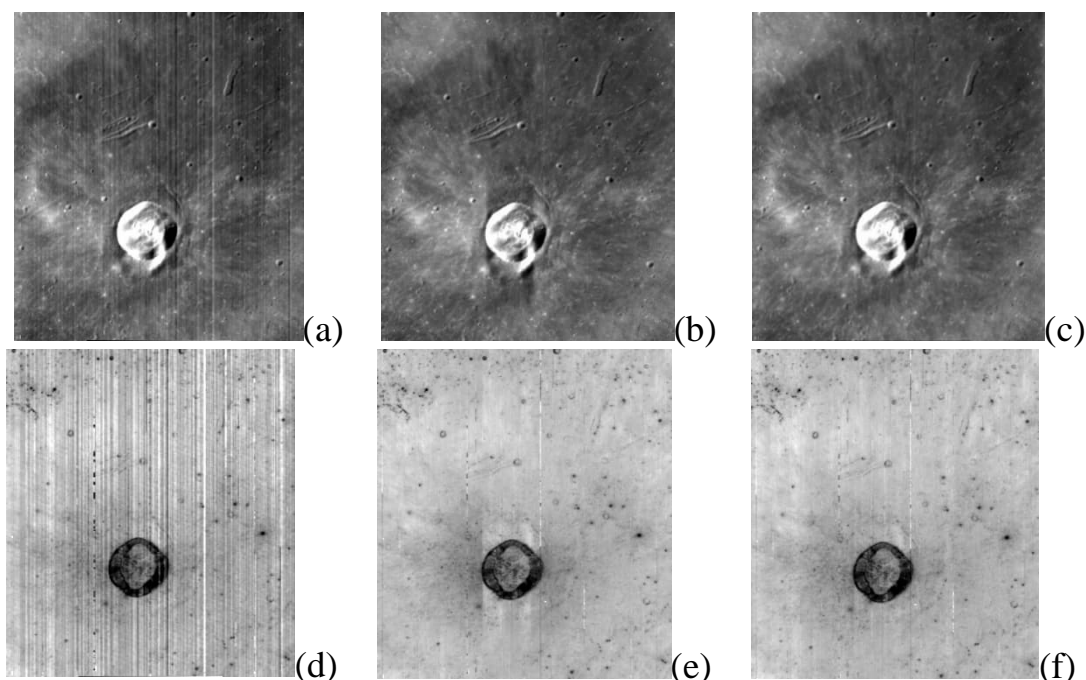


Figure 4.6 The crater Dawes (see Fig. 4.1). Images of reflectance at 950 nm, which are (a) unprocessed, (b) processed with sharp rejection, and (c) processed using the filter (9), respectively. The same for the color ratio  $C(950 \text{ nm}/750 \text{ nm})$  (d) – (f), respectively.

Ilmenite is a spectrally poor mineral in the range of wavelengths between 540 nm and 2600 nm. This mineral can be characterized by (1) low albedo, (2) slight elevation at 1000 nm, and (3) broad (about 500 nm at the half-depth) shallow absorption centered near 1550 nm (see Fig. 4.7). The prominent feature in the ilmenite spectra at 1000 nm could be a reliable sign of the presence of this mineral. However, this feature is superposed with much more expressed absorption bands of the pyroxenes and olivine that are common for the soils of the lunar maria. The ilmenite absorption band at 1550 nm is considered to be the most prominent characteristics of ilmenite presence. Unfortunately, only one band parameter, the band's depth, can be obtained, because of the overlap of the wings of the 1550 nm band with the bands of other minerals. To assess the depth, we use the convex hull technique (e.g., Shkuratov et al., 2019), considering a continuum in each image pixel with the next equation:



$$S(\lambda) = 1 - \frac{A(\lambda)}{A_{CH}(\lambda)}, \quad (4.10)$$

where  $A_{CH}(\lambda)$  is the albedo determined for the convex hull line.

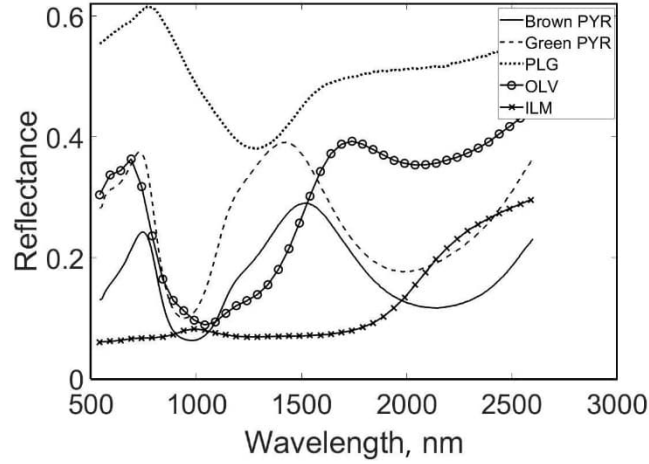


Figure 4.7 Spectral reflectance of minerals taken from the LRMCC dataset (Isaacson et al., 2011); brown and green pyroxenes, plagioclase, olivine, and ilmenite are presented.

Examples of continuum removing are displayed in Fig. 4.8, where the mean spectra of four small areas (3×3 pixels) with different TiO<sub>2</sub> content are taken from the site [http://wms.lroc.asu.edu/lroc/view\\_rdr/WAC\\_TIO2](http://wms.lroc.asu.edu/lroc/view_rdr/WAC_TIO2). One may see the manifestation of the spectral feature near 1550 nm clearly depends on the TiO<sub>2</sub> content: the greater the TiO<sub>2</sub> abundance, the more conspicuous the 1550 nm band. Ilmenite alters the pyroxene bands near 1000 nm and 2000 nm, as has been established earlier (Nash and Conel, 1974).

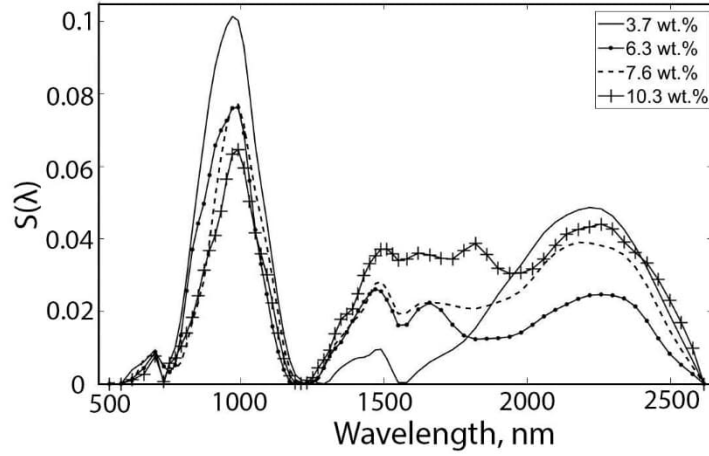


Figure 4.8 Depth spectra normalized on a convex hull by Eq. (4.410). The  $\text{TiO}_2$  contents are indicated.

To determine the band depth ( $BD$ ) with Eq. (4.10), it is necessary to find the maximal  $S(\lambda)$ . Because of spectral noise the value of  $\lambda_{max}$  cannot be measured reliably, and we use the following expression for the  $BD$

$$BD = \frac{S_{1489\text{nm}} + S_{1509\text{nm}} + S_{1529\text{nm}} + S_{1549\text{nm}} + S_{1579\text{nm}}}{5} \quad (3.11)$$

We use Eq. (4.11) to map the ilmenite distributions in vicinities of the craters Plinius and Dawes. Figs. 4.9 and 4.10 show low ilmenite abundance in Mare Serenitatis and ejecta of the craters.

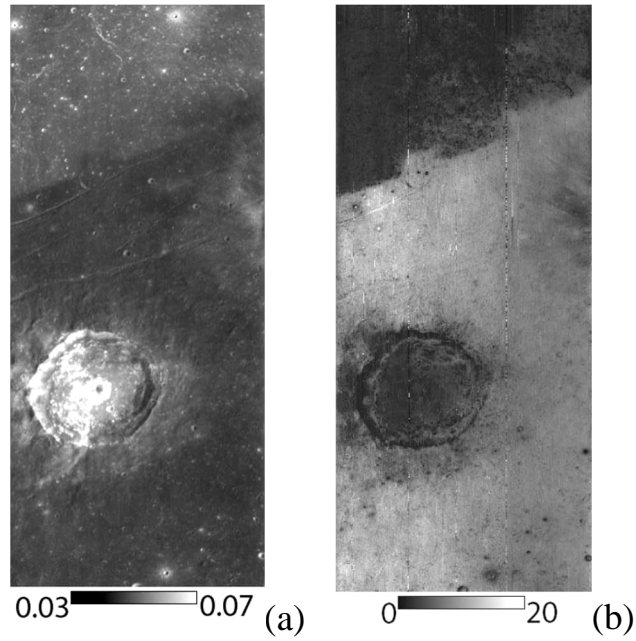


Figure 4.9 The albedo at 750 nm (a), and *BD* map calibrated with Eq. (4.12) in wt% (b) of the crater Plinius.

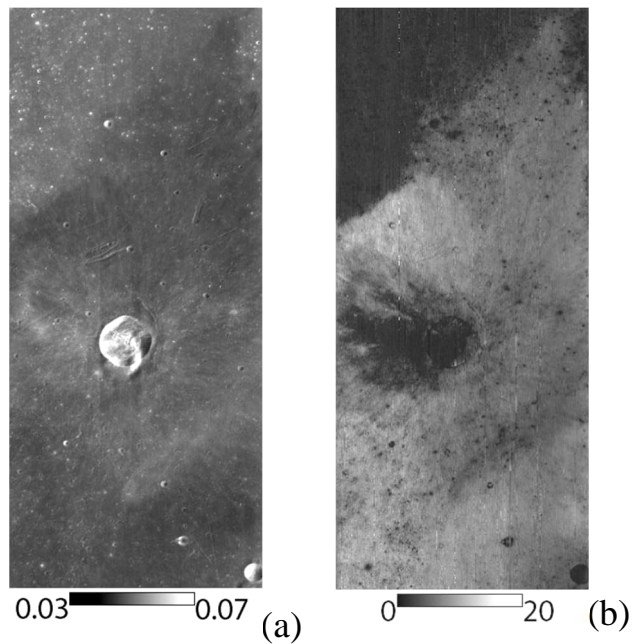


Figure 4.10 The albedo at 750 nm (a) and *BD* map calibrated with Eq. (4.12) in wt% (b) of the crater Dawes.

The depth of the absorption band at 1550 nm can be calibrated in terms of ilmenite content with a laboratory dataset. We here use the LRMCC spectral and mineralogical data from <http://www.planetary.brown.edu/LRMCC/> (Isaacson et al., 2011). The spectral data overlap the  $M^3$  range. There are eight different spectra available: four for the two low-Ti mare obtained during *Apollo 15* mission, and four for the high-Ti mare obtained during *Apollo 17* mission; they are different in grain size. For additional data, we use the spectra of the pure ilmenite available in the same dataset. As can be seen from Fig. 4.11, the band depth correlates with ilmenite content linearly. The following function describes the dependence satisfactorily:

$$\text{Ilmenite Content, wt.\%} \cong 202.8 \cdot BD \quad (4.12)$$

Eq. (4.12) allowed us to calibrate the images shown in Figs. 4.9 and 4.10.

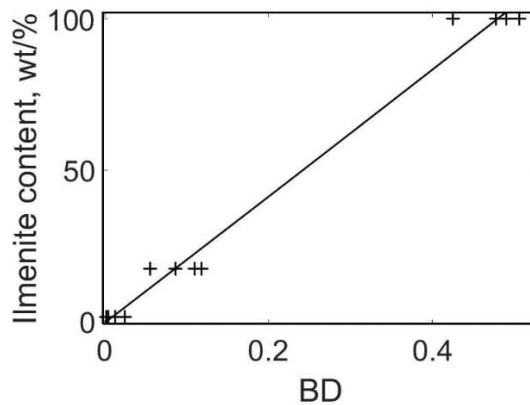


Figure 4.11. Calibration of the spectral parameter  $BD$  in terms of ilmenite content using the full set of laboratory data.

We map the ilmenite abundance for the full area shown by the frame in Fig. 4.1, merging suitable portions of the following  $M^3$  images: M3G20090731T092152, M3G20090731T045352, M3G20090731T005012, and M3G20090730T205153. These were acquired for spacecraft orbits at almost the

same photometrical conditions. The large map of ilmenite abundance was computed using portions filtered separately and then merged. Both the reflectance and ilmenite abundance maps were averaged in areas where the portions overlapped. Fig. 4.12 shows the reflectance image at 750 nm, the map of ilmenite abundance, and the distribution of  $\text{TiO}_2$  taken from [http://wms.lroc.asu.edu/lroc/view\\_rdr/WAC\\_TIO2](http://wms.lroc.asu.edu/lroc/view_rdr/WAC_TIO2).

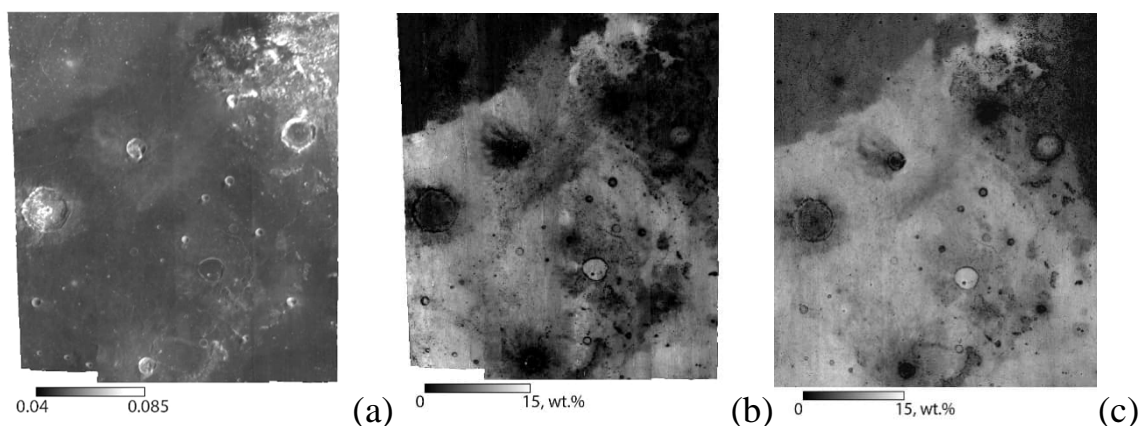


Figure 4.12. The full reflectance image at 750 nm (a), the map of ilmenite abundance (b), and the distribution of  $\text{TiO}_2$  taken from [http://wms.lroc.asu.edu/lroc/view\\_rdr/WAC\\_TIO2](http://wms.lroc.asu.edu/lroc/view_rdr/WAC_TIO2) (c).

#### 4.4 Discussion

We have noted that in the lunar mare material the element titanium can be present in ilmenite as well as an admixture in minerals and glasses. For instance, in low-Ti basalts  $\text{TiO}_2$  is largely hosted in Fe-Ti spinels. Figs. 4.12b,c confirms this, revealing the total titanium content may noticeably exceed the abundance of ilmenite. This is clearly seen with the diagram of correlation between the ilmenite and  $\text{TiO}_2$ , which is presented in Fig. 4.13. In the diagram there are two clusters associated with the Mare Tranquillitatis and the Mare Serenitatis. It should be

noted the correlation of ilmenite with  $\text{TiO}_2$  is reliably detectable only for significant percentages of the latter.

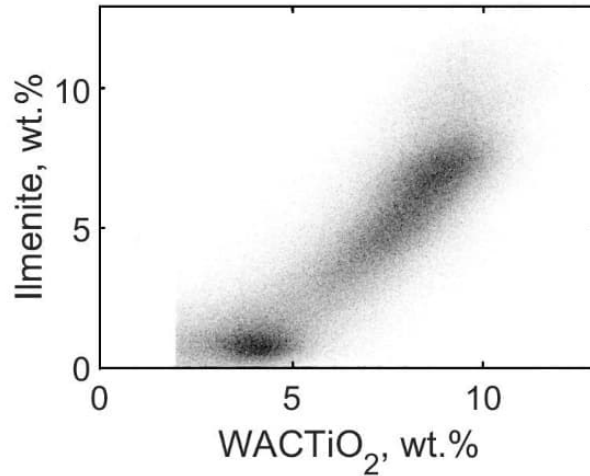


Figure 4.13. The correlation of the ilmenite abundance with the  $\text{TiO}_2$  content estimated using  $C(321\text{ nm}/415\text{ nm})$  from [wms.lroc.asu.edu/lroc/view\\_rdr/WAC\\_TIO2](https://wms.lroc.asu.edu/lroc/view_rdr/WAC_TIO2)

Laboratory data may corroborate the diagram depicted in Fig. 4.13. The correlation between the  $\text{TiO}_2$  and ilmenite abundances in lunar regolith samples from the RELAB dataset (Pieters et al., 2006) is shown in Fig. 4.14, which is rather similar to that in Fig. 4.13. Thus, we can separate ilmenite  $\text{TiO}_2$  from the total. We calculate the content of  $\text{TiO}_2$  hosted in ilmenite using the following equation

$$\text{TiO}_2^{\text{ilmenite}} = \frac{M(\text{TiO}_2)}{M(\text{FeTiO}_3)} \times \text{Ilmenite, wt. \%}, \quad (4.13)$$

where  $M(X)$  is the molecular mass of  $X$ .

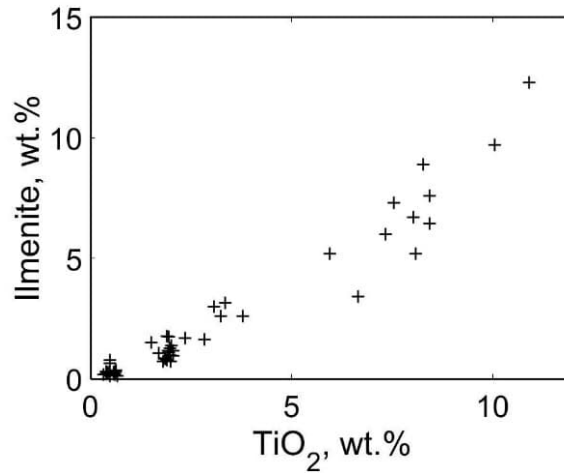


Figure 4.14. Correlations between  $\text{TiO}_2$  and  $\text{FeTiO}_3$  contents for lunar soil samples from RELAB datasets (Pieters et al., 2006).

We may subtract  $\text{TiO}_2^{\text{Ilmenite}}$  from the total  $\text{TiO}_2$  content, obtaining the map shown in Fig. 4.15. As one may see, the border between the lunar maria almost disappears and the variations of  $\text{TiO}_2$  abundance in Mare Tranquillitatis become less expressed, except in the neighborhood of the crater Dawes.

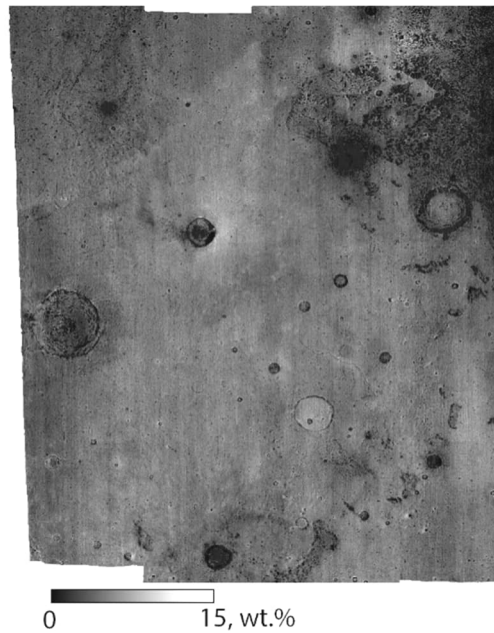


Figure 4.15. Map of the difference  $\text{TiO}_2^{\text{total}} - \text{TiO}_2^{\text{ilmenite}}$  in wt.%. This was calculated from Figs. 4.9 and 4.10.

Areas with high abundance of ilmenite can be prospective in future exploration of lunar resources. Taylor (1994) has found from laboratory measurements that the concentration of  $^3\text{He}$  in the regolith is closely correlated with the parameter  $[\text{TiO}_2 \cdot \text{I}_s/\text{FeO}]$ , where  $\text{I}_s/\text{FeO}$  characterizes regolith maturity (Morris, 1980). The regression equation of this correlation has the form

$$^3\text{He}[\text{ppb}] = 0.204[\text{TiO}_2 \cdot \text{I}_s/\text{FeO}]^{0.645}, \quad (4.14)$$

As the parameters  $\text{TiO}_2$  and  $\text{I}_s/\text{FeO}$  can be estimated from measurements of albedo and color ratios, this allows  $^3\text{He}$  concentration maps (Shkuratov et al., 1999b; Shkuratov and Bondarenko, 2001; Fa Wenzhe and Jin Ya-Qiu, 2007; Shkuratov et al., 2011). The  $^3\text{He}$  isotope has significantly higher concentration (up to 100 times) in ilmenite than in other minerals (Taylor, 1994). The reason is diffusion from ilmenite is much slower than these other minerals (Xiaohui Fu et al., 2011). Ilmenite is more retentive than other minerals for noble gases. Thus, the ilmenite can be considered as a potential source of fuel for nuclear fusion energy (Wittenberg et al., 1986; Taylor, 1994). Thus, mapping ilmenite areas with high resolution is very important. It should be emphasized that Eq. (4.14) needs to be recalculated for the case of ilmenite instead of  $\text{TiO}_2$ . This allows for a more reliable determination of  $^3\text{He}$ .



## 4.5. Conclusions

We present a technique that can provide quantitative assessment and mapping of ilmenite abundance using the absorption band at 1550 nm using processed *Chandrayaan-1* M<sup>3</sup> data. We use a soft filter instead of the sharp rejection technique proposed by Shkuratov et al. (2019) to remove the noise strips in frequency space. This technique prevents significant signal losses and also reduces the appearance of the Gibbs phenomenon related to the contrast albedo formations with sharp boundaries.

We use this technique to examine a region between Mare Serenitatis and Mare Tranquillitatis and map the depth of the M<sup>3</sup> ilmenite band near 1550 nm, which was calibrated using the LRMCC laboratory dataset (Isaacson et al., 2011). The obtained ilmenite abundance distribution correlates with the TiO<sub>2</sub> content determined by Sato et al. (2017) and is presented in [wms.lroc.asu.edu/lroc/view\\_rdr/WAC\\_TIO2](https://wms.lroc.asu.edu/lroc/view_rdr/WAC_TIO2).

We compare the titanium distributions calculated by Sato et al. (2017) and determined from the assessment of ilmenite content. As would be expected,  $\text{TiO}_2^{\text{total}} > \text{TiO}_2^{\text{ilmenite}}$ . This demonstrates ilmenite is not the only source of lunar titanium. This element can be in the form of impurities in other minerals as well as in dark glasses that do not reveal the ilmenite band near 1550 nm.

## 4.6 References

- Brillinger, D.R., 2001. Time Series: Data analysis and theory. SIAM's Classics in Applied Mathematics, Philadelphia, 540 pp.
- Burns, R., 1993. Mineralogical Applications of Crystal Field Theory. Cambridge University Press, Cambridge 459 pp.
- Charette, M.P., McCord, T.B., Pieters, C.M., Adams, J.B., 1974. Application of remote spectral reflectance measurements to lunar geology classification and determination of titanium content of lunar soils. *J. Geophys. Res.* 79(11), 1605-1613, doi:10.1029/JB079i011p01605
- Fa Wenzhe, Jin Ya-Qiu., 2007. Quantitative estimation of helium-3 spatial distribution in the lunar regolith layer. *Icarus* 190, 15-23, doi: 10.1016/j.icarus.2007.03.014
- Gillis, J., Jollif, B., Elphic, R., 2003. A revised algorithm for calculating TiO<sub>2</sub> from Clementine UV–VIS data: a synthesis of rock, soil, and remotely sensed TiO<sub>2</sub> concentrations. *J. Geophys. Res.* 108 (E2), 5009, doi:10.1029/2001JE001515.
- Gottlib, D., Shu Chi-Wang, 1997. On the Gibbs phenomenon and its resolution. *SIAM Rev.* 39(4), 644–668.
- Hapke, B., 2001. Space weathering from Mercury to the asteroid belt. *J. Geophys. Res.* 106, 10,039–10,073.
- Isaacson, P., A. Basu S., Pieters, C., Klima, R., Hiroi, T., Liu, Y., and Taylor, L., 2011, The lunar rock and mineral characterization consortium: Deconstruction and integrated mineralogical, petrologic, and spectroscopic analyses of mare basalts. *Meteorit. Planet. Sci.* 46, 228-251, doi:[10.1111/j.1945-5100.2010.01148.x](https://doi.org/10.1111/j.1945-5100.2010.01148.x).
- Johnson, J.R., Larson, S.M., Singer, R.B., 1991. A re-evaluation of spectral ratios for lunar mare TiO<sub>2</sub> mapping. *Geophys. Res. Lett.* 18 (11), 2153–2156.

- Korokhin, V.V., Kaydash, V.G., Shkuratov, Y.G., Stankevich, D.G., Mall, U., 2008. Prognosis of TiO<sub>2</sub> abundance in lunar soil using a non-linear analysis of Clementine and LSCC data. *Planet. Space Sci.* 56(8), 1063–1078.
- Korokhin, V., Shkuratov, Y., Kaydash, V., Basilevsky, A., Rohachova, L., Velikodsky, Y., Opanasenko, N., Videen, G., Stankevich, D., 2016. Characterization of a photometric anomaly in lunar Mare Nubium. *Planet. Space Sci.* 122, 70–87. doi:10.1016/j. Pss.2016.01.011.
- Lucey, P., Blewett, D., Bradley, L., 2000. Lunar iron and titanium abundance algorithm based on final processing of Clementine ultraviolet–visible images. *J. Geophys. Res.* 105, 20,297–20,305.
- Lundeen, S., McLaughlin, S., Alanis, R., 2011. Data product software interface specification, Version 9.10, [pds-imaging.jpl.nasa.gov/documentation/M3 DPSIS.PDF](https://pds-imaging.jpl.nasa.gov/documentation/M3_DPSIS.PDF)
- Morris, R., 1980. Origins and size distribution of metallic iron particles in lunar regolith. *Proc. Lunar Planet. Sci. Conf.* 11<sup>th</sup>. LPI Houston, USA, pp. 1697-1712.
- Nash, D.B., Conel, J.E., 1974. Spectral reflectance systematics for mixtures of powdered hyperstene, labradorite, and ilmenite. *J. Geophys. Res.* 79(11), 1615-1621.
- Nozette, S., and 33 colleagues. 1994. The Clementine mission to the Moon: Scientific overview. *Science* 266, 1835-1839.
- Pieters, C., McCord, T.B., 1976. Characterization of lunar mare basalt types: I. A remote sensing study using reflection spectroscopy of lunar soils. *Proc. Lunar Sci. Conf.* 7<sup>th</sup>, p.2677-2690.
- Pieters, C.M., Shkuratov, Yu., Kaydash, V., Stankevich, D., Taylor, L., 2006. Lunar soil characterization consortium analyses: Pyroxene and maturity

- estimates derived from Clementine image data. *Icarus* 184, 83-101, doi: 10.1016/j.icarus.2006.04013
- Pieters, C.M., 19 colleagues, 2009. The Moon Mineralogy Mapper (M3) on Chandrayaan-1. *Science* 326, 568–572.
- Prettyman, T., Hagerty, J., Elphic, R., Feldman, W., Lawrence, D., McKinney, G., Vaniman, D., 2006. Elemental composition of the lunar surface: Analysis of gamma ray spectroscopy data from Lunar Prospector. *J. Geophys. Res.* 111 (E12007), doi:10.1029/2005JE002656
- Robinson, M.S., Hapke, B.W., Garvin, J.B., Skillman, D., Bell III, J.F., Ulmer, M.P., Pieters, C.M., 2007. High resolution mapping of TiO<sub>2</sub> abundances on the Moon using the Hubble Space Telescope. *Geophys. Res. Letters* 34(13), doi: 10.1029/2007gl029754
- Sato, H., Robinson, M.S., Lawrence, S.J., Denevi, B.W., Hapke, B., Jolliff, B.L., Hiensinger, H., 2017. Lunar mare TiO<sub>2</sub> abundances estimated from UV/Vis reflectance. *Icarus* 296, 216-238, doi: 10.1016/j.icarus.2017.06.013
- Shkuratov, Y.G., Bondarenko, N.V., 2001. Regolith thickness mapping of the Moon by radar and optical data. *Icarus* 149, 329-338.
- Shkuratov, Yu.G., Kaydash, V.G., Opanasenko, N.V., 1999a. Iron and titanium abundance and maturity degree distribution on lunar nearside. *Icarus* 137, 222-234.
- Shkuratov, Y.G., Starukhina, L.V., Kaydash, V.G., Bondarenko, N.V., 1999b. Distribution of <sup>3</sup>He abundance over the lunar nearside. *Solar Syst. Res.*, 33(5), 409-420.
- Shkuratov, Yu., Kaydash, V., Stankevich, D., Pinet, P., Chevrel, S., Daydou, Y., 2005. Derivation of elemental abundance maps at intermediate resolution from optical interpolation of Lunar Prospector Gamma-Ray spectrometer data. *Planet. Space Sci.* 53, 1287-1301.

- Shkuratov, Y., Kaydash, V., Korokhin, V., Velokodsky, Y., Opanasenko, N., Videen, G., 2011. Optical measurements of the Moon as a tool to study its surface. *Planet. Space Sci.* 59. 1326-1371.
- Shkuratov, Y., Surkov, Y., Ivanov, M., Korokhin, V., Kaydash, V., Videen, G., Pieters, C., Stankevich, D., 2019. Improved Chandrayaan-1 M3 data: A northwest portion of the Aristarchus Plateau and contiguous maria. *Icarus* 321, 34–49.
- Surkov, Y., Shkuratov, Y., Kaydash, V., Korokhin, V., Videen, G., 2019. Mapping the 1.5  $\mu\text{m}$  ilmenite spectral feature using Chandrayaan-1 M<sup>3</sup> data. 50<sup>th</sup> LPSC, abstract #1026.
- Taylor, L., 1994. Helium-3 on the Moon: Model assumptions and abundances. *Eng. Constr. Oper. in Space IV*, ASCE Publ., Proc. of Space' 94, 678–686.
- Wittenberg, L., Santarius, J., Kulchinski, G., 1986. Lunar source of <sup>3</sup>He for fusion power. *Fusion Technol.* 10, 167–178.
- Xiaohui Fu, Yongliao Zou, Yongchun Zheng, Huaiyu He, Ziyuan Ouyang, 2011. Noble gas diffusion mechanism in lunar soil simulant grains: Results from <sup>4</sup>He+ implantation and extraction experiments. *J. Earth Sci.*, 22 (5), 566–577.

## CHAPTER 5. GENERAL SUMMARY AND CONCLUSIONS

The dissertation is devoted to spectrophotometric studies of the north-western part of the Aristarchus Plateau, the southern part of the Mare Vaporum, together with the volcanic complex of the Hyginus crater and furrow, and the area along the border of the Mares Serenitatis and Tranquilitatis.

The purpose of this work was to determine and map the mineralogical composition of the indicated areas of the Moon's surface based on the spectral data of the M<sup>3</sup> detector installed on the Chandrayan-1 spacecraft. To achieve this goal, a two-stage method of additional data processing in the form of hyperspectral cubes was developed, which allowed one to obtain reliable maps of the distribution of spectral parameters, fundamentally important for the mineralogical interpretation of data.

The paper contributed to the mineralogical interpretation of spectrophotometric data of the Vis-NIR range and methods of remote prognosis of the mineralogical composition of the Moon's surface. For the first time, the effect of the presence of ilmenite in the regolith on the shape of the diffuse reflectance spectra of the Moon's surface was established. Namely, the relationship between its abundance and the depth of the absorption band near 1.5  $\mu\text{m}$  was shown, on the basis of which a spectral method of quantitative assessment of the ilmenite content was proposed.

The technique of determining the mineralogical diversity of the surface of the Moon using Adams' diagram has received further development. The use of a cluster analysis approach made it possible to construct spatial distributions of spectral provinces, which, with appropriate mineralogical interpretation, allows for the identification and mapping of areas with a certain similar mineralogical

composition. Particular attention was paid to the methods of identification and clarification of the contours of deposits of pyroclastic material.

The main results of spectrophotometric studies and mineralogical mapping of selected areas of the Moon's surface:

1) maps of the main spectral provinces of the north-western part of the Aristarchus Plateau were constructed. Four types of pyroxenes of the basalt environment of the plateau have been identified. Spectral features of the material covering the plateau indicate a high content of pyroclastic material in almost the entire area studied of the plateau;

2) it was determined spectrophotometrically that pyroclastic glass is present in the DMD deposits in the south of Mare Vaporum. The contours of deposits of pyroclastic material have been clarified. The uneven distribution of the depth of the absorption band near 1  $\mu\text{m}$  on the surface of these deposits indicates variations in the content of pyroclastic glass;

3) confirmed the presence of DMD-like pyroclastic material in the southern Paru Sea in the low-albed material around Hygin Crater. This allows us to spectrally differentiate this material from basalts of Mare Vaporum;

4) an analysis of the IMP spectra located in the Hyginus crater was carried out. The main spectral features of IMP are the shape of the contours of the absorption band near 2  $\mu\text{m}$  and a lower overall slope of the spectra, which were interpreted as a difference in mineralogical composition and a younger age of surface formation;

5) forecasting of the ilmenite content at the border of Mare Serenitatis and Tranquilitatis was carried out. It was determined that the content of ilmenite in the lunar regolith varies significantly and can range from 0 to 20 wt.%. A significant decrease in the content of ilmenite on the walls of Pliny and Dawes craters and small craters is associated with the destruction of the crystalline structure during impact events. Less pronounced spatial variations of ilmenite in the Tranquilitatis Mare are probably the consequences of the inhomogeneity of the flow of primary lava flows and solidification regimes;

6) analyzed the difference between the total content of  $\text{TiO}_2$  in regolith and the amount of  $\text{TiO}_2$  contained in ilmenite. Such a difference is evidence that  $\text{TiO}_2$  is distributed between several mineralogical components, primarily between ilmenite and agglutinates.

The scientific results obtained are in general in good agreement with the modern general ideas about the mineralogical composition of the surface of the Moon. New clarifying information was obtained on (1) the mineralogical composition of selected areas of the Moon's surface and the spatial distribution of mineralogical provinces is clarified; (2) peculiarities of the mineralogical composition of the volcanic complex of the Hyginus crater and the IMP formations; (3) distribution of ilmenite content along the boundary of Maria Tranquilitatis and Serenitatis.

The results obtained in this way can be used for scientific purposes, for example, for the further development of ideas about the mineralogical composition, processes of formation and evolution of the material of the surface of the Moon, studies of lunar volcanism, for planning future scientific research and



space missions, to assess potential resources, in particular, titanium and promising fuel for thermonuclear reactors - the  $^3\text{He}$  isotope.

The developed method of data processing of the scanning spectrometer  $M^3$  and the corresponding software for cluster analysis of the Adams' diagram, estimation and mapping of the ilmenite content can be used in spectrophotometric studies and mineralogical interpretation of the spectral data of this instrument for other areas of the Moon's surface. In addition, it is assumed that this method of additional data processing can be extended to  $M^3$ -like spectrophotometric data of other detectors in the form of hyperspectral cubes, for example, the IIRS instrument installed onboard the Chandrayaan-2 spacecraft.

## ACKNOWLEDGEMENTS

The research of this thesis was started at the Institute of Astronomy of V.N. Karazin Kharkiv National University of Ukraine and finalized at the Max-Planck Institute for Solar System Research in Göttingen, Germany. Financial support from the Max-Planck Society is gratefully acknowledged.

I thank my university supervisor, Prof. Dr. Martin Kappas, for accepting me as a Ph.D. student at the Georg-August University of Göttingen and for supporting me during the stages of my Ph.D work. For topic selection along with substantial advice I would like to thank Dr. Vadym Kaydash and Prof. Yuriy Shkuratov of V.N. Karazin Kharkiv National University of Ukraine. I thank my supervisor at the Max-Planck Institute for Solar System Research, Dr. Urs Mall, for accepting me at the Max-Planck Institute, and for his great help and support during my Ph.D work.

I am grateful to Dr. Viktor Korokhin, Dr. Serhiy Velichko, Dr. Dmytro Stankiewicz and other members of the Remote Planet Sensing Group of the Institute of Astronomy of V.N. Karazin Kharkiv National University of Ukraine for the many valuable discussions and advice. I am grateful to PD. Dr. Harald Krüger, Dr. Daniel Wyss and Prof. Dr. Carsten Damm for finding time to be part of the examination board.

## Academic Curriculum Vitae

### Yehor Surkov

#### 1. Personal Information

Name: Yehor Surkov

Born: 27.09.1994 in Kharkiv, Ukraine

#### 2. Education

2017 M. Sci., Faculty of Physics and Technologies, V.N. Karazin Kharkiv National University, Ukraine.

2015 B. Sci., Faculty of Physics and Technologies, V.N. Karazin Kharkiv National University, Ukraine.

#### 3. Publications in peer reviewed journals

1. Improved Chandrayaan-1 M3 data: A northernmost portion of the Aristarchus plateau and adjacent maria. Y. Shkuratov, *Y. Surkov*, M. Ivanov, V. Korokhin, V. Kaydash, G. Videen, C. Peiters, and D. Stankevich. *Icarus* 321, 34-49 (2019)

2. Lunar ilmenite content as assessed by improved Chandrayaan-1 M3 data. *Y. Surkov*, Y. Shkuratov, V. Kaydash, V. Korokhin, and G. Videen. *Icarus* 341, 113661 (2020)

3. Characterizing southern portion of Mare Vaporum with improved Chandrayaan-1 M3 data. *Y. Surkov*, Y. Shkuratov, V. Kaydash, S. Velichko, V. Korokhin, and G. Videen. *Icarus* 355, 114123 (2021)

4. Photometric analysis of the Luna spacecraft landing sites. S. Velichko, V. Korokhin, Y. Shkuratov, V. Kaydash, *Y. Surkov*, and G. Videen. *Planet. Space Sci.* 216, 105475 (2022)